Can you determine nanoparticle size from lattice vibrations?

Sylvia Yuk Yee Chung

Masters by Research: Physics
Supervisor: Dr Dean Sayle
Date of Submission: 25/04/18
Student ID: 16900493
Page Count: 98

Abstract

Molecular dynamics simulation was used to calculate breathing mode frequencies of polyhedral ceria nanoparticles and determine whether the frequency can be used as an indicator of nanoparticle size and shape. In particular, energy was added to ceria nanoparticles, 2.7 – 8 nm in size, to induce vibration. The frequencies of the breathing mode vibrations were calculated to range from 28 – 78 cm^{-1} and change as a function of particle size in accord with experiment.

This information is important with respect to analytical tools used to measure nanoparticle sizes and also nanomedicinal applications. Moreover, MD simulation can be used as a tool to help complement experiment in predicting structures that give rise to particular breathing mode vibrational frequencies.

Acknowledgements

I would like to thank my supervisor, Dr Dean Sayle, for accepting me onto this degree. Nanoparticle simulation is an area of research I was previously unfamiliar with, but an enjoyable field to have ventured into.
The advice I have accumulated from him over the past few years has significantly improved my understanding of not only the subjects from this degree course, but also lessons which can be applied to everyday life. Dean has taught me a great deal and the experience of researching under his supervision has made 2016/2017 the best academic year I have ever had. I have enjoyed this year so much that I fear in the future, I will not be able to get a better supervisor than him.

I cannot recall the countless amount of times he has come to my aid, whether it was a simple coding problem or explaining a topic I had trouble understanding. His generosity extends beyond the degree course, and I know this because his guidance has helped me secure a Japanese government funded scholarship to do a PhD in Japan, a dream I have wished for as long as I remember. For this reason, I know I will be forever grateful to him and will cherish his guidance dearly for the rest of my life.

Table of Contents

Chapter 1: Introduction

Ceria nanoparticle is commercially known as a glass polishing agent and as a catalytic converter in vehicle exhausts. Amongst the research community, ceria is known for its anti-oxidant property which has been attributed to its ability to have two oxidation states co-existing on the surface. This makes ceria an ideal compound for applications where catalytic behaviour is desired, such as nanomedicine[1]. Nowadays, it is common knowledge that oxidants are harmful to the body and as such, the research of ceria and its ability to reduce the levels of reactive oxygen species (ROS), compounds that contribute to oxidation and can be scavenged by ceria[1-3], is of high interest.

In an attempt to maintain charge neutrality, the presence of Ce^{3+} ions on the surface leads to the production of oxygen vacancies. Therefore, a ceria nanoparticle with a high surface charge ratio of Ce^{3+}/Ce^{4+} exhibits anti-oxidant behaviour[1] as a result of the increased oxygen vacancies produced. These vacancies are catalytically active sites which promotes the removal of radicals and other reactive oxygen species (ROS). In some cases however, the resulting products from the catalytic reaction may accumulate. A build-up of these species could lead to oxidation within the cell, which can be desired or disadvantageous depending on the circumstance. Overall, ceria can act as both an oxidant and an anti-oxidant, and can be exploited to enhance the behaviour of the desired characteristic.

One of the successful applications of ceria involves the ceria nanoparticle being introduced into embryo cells, which led to the occurrence of angiogenesis[1]. Angiogenesis is the formation of new blood vessels from existing blood vessels and is associated with the healing of wounds. It is therefore beneficial in cases where wounds are present because the process is healing the damaged tissue, but can also occur in tumours which is disadvantageous as it is providing nutrients to the tumour cells. Das et al.[1] reported that the surface charge ratio was the cause behind the induction of angiogenesis, specifically the removal of ROS. Being able to control whether angiogenesis is induced or not is highly advantageous and therefore, a better understanding of how ceria can modulate oxygen is worth investigating.

Vibration is the oscillation or the periodic motion of an elastic body or medium, moved from its position or state of equilibrium. This phenomenon exists in multiple forms, sound and heat as two examples, and are therefore, vital for everyday life. Sound occurs by vibrating the molecules in air, the air acting as a medium for which the waves can travel in. Heat is produced by the disordered vibrations in molecules. Both of these occurrences are examples of the vibration of particles.

A molecular vibration is generally defined as the change of the shape of the molecule caused by the bending, stretching or rotation of the bonds, which occurs whilst the overall molecule is moving in constant motion. There are two types of molecular vibrational modes, stretching and bending, examples of such are shown below in Figure 1.

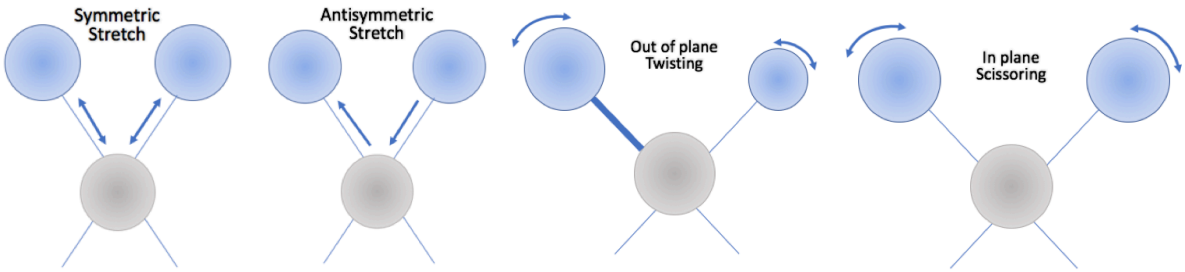

Figure 1: A few examples of how a molecular vibration occurs using 2D drawn versions of a stick and ball diagram. The first two diagrams on the left are showing the types of stretching modes, whilst the two diagrams on the right are demonstrating a bending type mode.

The ability to characterise vibrations allows for the prediction of the functional groups and other material properties. Through the use of spectroscopic methods, molecular vibrations can be induced, the data from which can identify the different types of bonds that exist within the compound. IR spectroscopy is non-destructive, relatively easy to use and is not time consuming. These advantages, along with the ability to provide information on easily distinguished functional groups makes this technique a commonly used spectroscopic method for analysing vibrational modes. Resultantly, there is an abundant amount of research utilising and observing molecular vibrations, and what information these modes can provide about the material properties of the structure. Although there is significantly more literature on the studies of the higher frequency molecular vibrations, researchers over the past few decades have started to show more attention on the properties of breathing modes and what information these modes can provide.

The breathing mode is a symmetric stretch mode, observed as a type of movement where the atoms within the molecule are moving in sync and in phase to each other in the radial direction. In other words, an expansion and contraction in the radial direction. Figure 2 below shows a 2D representation of a radial breathing mode.

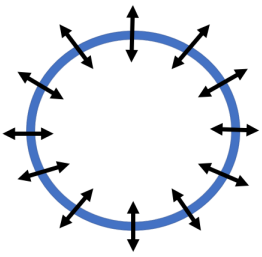

Figure 2: A simple graphic of how a radial breathing mode vibration occurs, with the blue circle representing a single wall nanotube, and the black double ended arrows showing the symmetric, in phase, synchronised movement.

A wide variety of nanostructures including gold nanorods, carbon nanotubes, fullerene, graphene and spherical nanoparticles have had their breathing modes experimentally observed using spectroscopic techniques. For a cubic lattice like ceria, the symmetry of the lattice is fixed during a breathing mode vibration and a dipole is prevented from being produced. As the breathing mode is a symmetric stretch type of mode, this mode does not appear in IR spectroscopy. Other spectroscopic methods, such as ultra-fast laser spectroscopy[4-5] and Raman spectroscopy[6] have been successfully used to obtain breathing mode frequencies. Raman spectroscopy is a favoured method as these breathing modes are Raman active and are accessible at the low frequency Raman region. Centro-symmetric

molecules such as ceria and carbon dioxide follow the rule of mutual exclusion, where their Raman active modes are IR inactive and vice versa.

The size of a nanoparticle affects properties such as the melting point temperature, optical effects and the cooling of excited electrons. Directly measuring characteristics such as size, shape and other geometric related properties is an expensive procedure and can take a long time to produce results. Observing the breathing mode vibration and therefore, acquiring the frequency, can give rise to various types of information including the possibility of being able to determine the size and shape of nanoparticles. An example of such involves the radial breathing mode of carbon nanotubes. This breathing mode can identify the diameter of carbon nanotubes using Raman spectroscopy[7]. This is evidence that the diameter of a nanostructure can be predicted from its breathing mode. According to a review by Ghavanloo et al.[8], the material and morphological properties of a nanostructure affects what frequency is produced, indicating that these geometrical characteristics could be identified from the frequency. Obtaining breathing mode frequencies as a function of the nanoparticle size and shape are perhaps the most obvious but also simple choice for testing the findings reported by these authors. A successful attempt would confirm that this may be a potentially simpler method for identifying such characteristics.

Hodak et al.[9] discovered that gold particles of differing diameters will produce different modulation frequencies. They concluded that the size of a gold nanoparticle was inversely proportional to the beat frequency it produced. The vibrations observed in their study were acoustic breathing modes and is some form of evidence of what is expected of a relationship between nanoparticle size and the breathing mode frequency observed. This finding leads to the suggestion that perhaps a ceria nanoparticle would also provide the same observation.

As mentioned above, ceria can induce the process of angiogenesis[1]. The authors suggested that perhaps it was related to the different surface planes on the nanoparticle exhibiting different reactivity. Simulating the breathing mode vibration would cause the entire nanoparticle to expand and withdraw continuously, which would disrupt and expose the surfaces more than it would usually be exposed when at rest. Ideally, this would increase the reactivity of the surfaces. This is based on the assumption that the action of expanding and withdrawing during a vibration displaces the atoms from their lattice positions, leading to a momentary disorder amongst the atoms, disrupting the lattice, and an increase in the surface energy.

Another potentially useful application from investigating the breathing mode of ceria nanoparticle is inspired by the study reported by Wheaton et al[10]. The authors obtained the breathing mode frequencies of nanoscale compounds such as polystyrene and titanium dioxide, with diameters ranging from 20 – 50 nm, and found the frequencies to decrease with increasing particle diameter. The frequencies were within the range of 0.7 – 10 cm^{-1} which is within the low GHz region. They then applied this technique to two proteins of differing shape and obtained characteristic frequencies from the breathing modes. This study is an example showing that the size, and possibly the shape, of a nanoparticle can be determined from the breathing mode frequency. This would serve as a more simple method

of nanoparticle identification, as opposed to the direct measurement of the size and other structural characteristics, which can be a time consuming and complex procedure.

This study aims to investigate whether the size and shape of a ceria nanoparticle can produce differing frequencies from its breathing mode vibration.

1.1 References

1. S. Das, J. M. Dowding, K. E. Klump, J. F. McGinnis, W. Self, S. Seal, Nanomedicine, 2013, vol 8, pp. 1483 – 1508
2. S. Das, S. Singh, J. M. Dowding, S. Oommen, A. Kumar, T. X. T. Sayle, S. Saraf, C. R. Patra, N.E. Vlahakis, D. C. Sayle, W. T. Self, S. Seal, Biomaterials, 2012, vol 33, pp. 7746 – 7755
3. M. Hijaz, S. Das, I. Mert, A. Gupta, Z. Al-Wahab, C. Tebbe, S. Dar, J. Chhina, S. Giri, A. Munkarah, S. Seal, R. Rattan, BMC Cancer, 2016, vol 220, pp. 220
4. P. V. Ruijgrok, P. Zijlstra, A. L. Tchebotareva, M. Orrit, Nano Letters, 2012, vol 12, pp. 1063 – 1069
5. V. Juve, A. Crut, P. Maioli, M. Pellarin, M. Broyer, N. Del Fatti, F. Vallee, Nano Lett., 2010, vol 10, pp. 1853 – 1856
6. H. Portales, L. Saviot, E. Duval, M. Fujii, S. Hayashi, J. Chem. Phys., 2001, vol 115, pp. 3444 – 3447
7. C. Kittel, Introduction to Solid State Physics 8th Edition, John Wiley & Sons, Inc, New Jersey, U.S.A, 2005
8. E. Ghavanloo, S. A. Fazelzadeh, H. Rafii-Tabar, International Materials Reviews, 2015, vol 60, pp. 312 – 329
9. J. H. Hodak, A. Henglein, G. V. Hartland, J. Chem. Phys., 1999, vol 111, pp. 8613 – 8621
10. S. Wheaton, R. M. Gelfand, R. Gordon, Nature Photonics, 2014, vol 9, pp. 68 – 72

Chapter 2: Literature Review on Ceria Nanoparticles

Nanoparticles are arguably the most versatile matter to currently exist. Nano-scale sized elements and compounds have differing properties to their bulk counterparts, creating a potential for multifunctional applications. This is one of the many reasons why nanoparticle research is of great interest to the scientific community. The medical field have successfully implemented multiple uses of nanotechnology, applications as "simple" as imaging to more intricate, functioning uses such as cancer treatment. Nanoparticles are also researched for their optical properties, stemming from their phenomenon of quantum confinement.

At the nano-scale, particles exhibit a high surface area to volume ratio. As the particle diameter decreases, an increase in the lattice parameter is observed[1]. In addition, when the diameter decreases, the surface area to volume ratio increases. It can therefore be said that an increase in the lattice parameter causes an increase in the surface area to volume ratio. The property of nanoparticles having a high surface area to volume ratio allows for a wide application in catalysis.

2.1 Molecular Dynamics

Molecular dynamics is a simulation technique which allows for the study of particles and systems by applying Newton's mechanics. This computational technique can be used to deduce a variety of information including; thermodynamic properties, catalytic behaviour, mechanical observations, intramolecular interactions and the calculation of energy band gaps. Newton's equation of motion is one of the most basic, yet fundamental laws existing for classical mechanics. This equation is also the basis for the molecular dynamics calculations, from which integrations occur to form the backbone of this computational technique. It serves as a tool for assisting in providing some of the most accurate representations of molecules and their interactions, thereby, allowing theoretical studies to occur before an experimental realisation. However, most studies involving molecular dynamics are not concerned with recreating an experimental result, but to simulate physical properties to investigate its origins and to simulate the reaction of systems under conditions that are difficult to produce in experiment. Molecular dynamics bridges the gap between theory and experiment.

The first step is the initialisation of the atomic positions and the velocities, which are randomly selected and then subjected to temperature scaling. The forces are then recalculated to find the positions and velocities per time step. Once the forces are calculated, the motion of molecules are computed. The results from which are then applied and analysed to find the specific physical quantities of interest. An important calculation step includes defining the potentials needed to simulate the interactions between atoms. A common example, is the Lennard-Jones potential,

$$U(r_{ij}) = \frac{A}{r_{ij}^{12}} - \frac{B}{r_{ij}^{6}} \qquad (Equation\ 1)$$

where $U(r_{ij})$ is describing the potential energy interactions between atoms 'i' and 'j' as a function of bond distance, r , A is the parameter describing the repulsion and B is the parameter involved with attraction. The first term on the right-hand side is the repulsive component, which is dominant when there is a short distance between the atoms, and the second term is the attractive component, which prevails at larger distances. This potential was created to represent a van der Waals interaction.

Potential parameters describe the short range and long range interactions between an atomic pair but are often simplifications of the actual interaction for reasons such as reducing computational cost. The potentials are therefore not an exact representation of the actual interaction and have a certain degree of accuracy. The methods employed for obtaining the potentials are a lengthy process and involve dedicated research groups that derive these values. One method includes assigning values of experimental properties such as defects and lattice parameters to simulation potential parameters, and adjusting the parameters to fit them to be in agreement with experimental data. There may not be experimental data existing for all properties, in which case, electronic-structure calculations are employed where quantum chemical calculations are conducted for molecular systems and density functional theory calculations are performed for condensed phases[2]. However, the method of fitting experimental values to the parameters is often preferred.

There are many advantages to using molecular dynamics. The most prominent advantage being the computational time. Depending on the requirements and how specific they are, a task such as synthesising and characterising nanoparticles may take as long as half a year to experimentally produce. Contrastingly, this would probably take half the amount of time or even less, using molecular dynamics. Perhaps the reasoning behind the ability to achieve such fast results is due to the utilisation of periodic boundary conditions, a construct allowing the determination of bulk material properties through the calculation of a few periodic images.

Another advantage is the ease of use, with a majority of the molecular dynamics simulations requiring just a high-speed computer and a supercomputer to connect to. The "laboratory" can be portable if the software is used on a laptop, allowing facile communication between collaborators to exchange and discuss simulation results. Also, mistakes and errors are easily rectified through coding. Something as intricate as changing an element in a compound would require an entirely new chemical to be ordered in for an experimental group, whereas a task as such for computational researchers would involve simple coding and not require as much effort.

As everything is conducted on computers, the health hazards and risks associated with using computer simulation techniques are not instantaneous, in comparison to the risks an experimentalist would face. For example, scientists working with chemicals face dangers such as, spillage, burns and exposure to harmful substances, to name a few. The dangers posed by continuously sitting in front of a computer monitor screen may not be an instant effect, but the most prominent long-term repercussions include a decline in vision and eye health, and possibly the development of bad posture from sitting at a desk for prolonged periods of time. The main difference between computational and experimental methods, with regards to health and safety, is that the risks posed by using computational methods

are not immediate, unlike experimental methods, but the long-term effects could be seen to be as equally damaging.

The costs for acquiring supercomputers and obtaining licensing for software vary, but are generally expensive. Computational time is also costly, with software companies often requesting reports of the progress on the theoretical experiments attempted with the software. Also, multiple computational users submitting jobs to the supercomputer would result in creating a virtual queue. Depending on how many processors are available, queue times can often last days and in the worst-case scenarios, weeks. The time spent waiting for a simulation to be submitted could be spent experimentally conducting the study. As well as having a simulation queue time, there is also the issue of run time. The time it takes for a simulation to complete its job varies by case. A simple equilibration simulation could initially take minutes for a system of a few particles, but a larger system may take hours. Despite this, the issue of computational time is of a small scale compared to conducting an experiment physically.

Another disadvantage is that depending on the simulation package, the software usually needs updating. New discoveries are occurring fast and for molecular dynamics to have the most accurate representation of atoms and their interactions, updates to their potentials are needed. Structures most likely do not exist in an ideal, crystal form, so the atomic models may be subject to interpretation in terms of whether they are sufficient representations of the compounds. This also means that the values obtained theoretically may differ to experimental results. An example of such case includes the acknowledgement of point defects, dislocations and structural impurities observed experimentally, which may not be accurately represented in a computational model. These differences from a perfect model would need to be implemented for acquiring the most accurate results possible, a difficult task considering that the addition of point defects and dislocations is already a challenging task in itself.
An incredible amount of research has been accomplished using molecular dynamics. Conclusively, it is clear that the advantages of simulation outweigh the disadvantages.

2.2 Ceria and Shape

For the general public, the sphere is perhaps the most common shape that comes to mind when imagining a nanoparticle. In reality, tubes, stars and more complex nanostructures also exist and are becoming increasingly implemented in applications. Nanoparticle shape is an important area to consider when selecting which nanostructures are used for application, especially as a wide variety of shapes can be adopted during synthesis. In particular, nanoparticles with morphologies resembling cubes and cylindrical or polyhedral shaped rods may have sharp edges or blunt edges that can cause damage to cells, so nanomedicine tends to give preference to spherical or near spherical shapes. Morphological differences can affect the type of properties or behaviour a structure will exhibit.

Pulido-Reyes et al.[3] studied the toxic effect of ceria nanoparticles on a biological system. Not only was the size varied, but shape also. Three, spherical nanoparticles were tested, with diameters of around 5 nm, 7 nm and 18 nm, with percentage of Ce^{3+} sites on the surface of 58%, 28% and 40% respectively. They found that the nanoparticles with 58% and 40% percentage Ce^{3+} surface sites to be toxic. The other nanoparticle shapes studied were

nanorods and nanocubes, of diameters 350 nm by 20 nm, and 50 nm, respectively. The percentage content of Ce^{3+} surface sites were 36% and 26% respectively. Both shapes were found to not be toxic. Whether this is due to the shape is uncertain as only one group of nanorods and nanocubes were tested. Had there been more nanorods and nanocubes of different percentage Ce^{3+} surface sites experimented upon, a more viable conclusion could be made as to whether shape really does influence toxicity. Despite this, Pulido-Reyes et al. were content with concluding that the toxicity is not shape dependent.
In crystallography, a grain is observed as an individual component consisting of a crystallite that repeats itself, forming the overall structure of the polycrystal. A grain boundary is defined as the junction or interface between separate grains and is usually of high energy due to being disordered, as the normal crystal structure is disrupted. In a polycrystal, the repeating units are the grains and within each grain, periodicity is observed. However, observing the polycrystal on a larger scale would show that there is no periodicity between the grains. Contrastingly, the repeat units in a single crystal are all connected to form an infinite long-range order throughout the entire structure, allowing periodicity to be observed across the whole crystal. The way the grains are positioned within the crystal contribute to the formation of the overall structure and shape of the crystal.

2.2.1 Surface Planes

Different types of surface planes exist and with it comes varying reactivity. The faces that are dominantly exposed on the surface of a crystal are often due to that specific plane being more energetically favourable than the other planes. This drives that specific plane to be generated during nanoparticle synthesis. The more energetically favourable planes are more stable and resultantly, less reactive. The less energetically favourable planes (less stable) are more susceptible to a reaction and more catalytically active. Due to the difference in how energetically favourable each surface plane is, their reactivities are different and their efficiency as a catalyst active site is also different.

The truncated octahedron is the most commonly observed morphology of ceria nanoparticles. An octahedron has 8 identical faces and as the {111} planes are the most stable[4] and energetically favourable plane adopted during synthesis, all of the surface planes in a ceria octahedron are of the {111} type. A ceria adopting a truncated octahedron structure would show a majority of the exposed planes being of the {111} type, but there is also a minority of the less stable planes such as the {110} and the {100} type[5]. A truncated octahedron will have 8 faces with the surface plane {111}, which has a greater surface area in comparison to the other planes, but will also have 6 faces of the {110} or the {100} type.

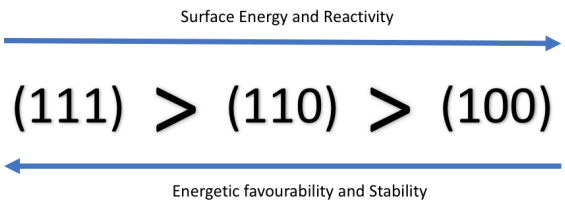

Figure 3: The surface planes listed in order of increasing energetic favourability and stability, and in order of increasing surface energy and reactivity. These properties were grouped together to show how one affects the other. For example, a plane with a high energetic favourability is a stable plane, which also has a low surface energy and low reactivity. A plane with a high surface energy means that it is more reactive and more susceptible to a reaction[4]. As shown in the figure above, the (111) plane is the most stable and would

therefore be the plane that is energetically driven the most to be produced during synthesis, but would also be the least reactive plane when compared to planes (110) and (100). As the (111) is the lesser reactive plane, it is also the less efficient catalytically active site and would experience a weak adsorption[6]. The (100) plane would be the most catalytically active site as it has the highest surface energy and would produce a stronger adsorption.

Depending on the stability of the surface, the ease of producing an oxygen vacancy varies. The most stable form of ceria has cations in the Ce^{4+} oxidation state. The presence of Ce^{3+} would lead to the formation of oxygen vacancies in an attempt to maintain charge neutrality. These oxygen vacancies provide an active site for a catalytic reaction to occur. A stable surface would require more energy to generate an oxygen vacancy, as opposed to a less stable surface which would require less energy. There is also another point to note that an oxygen vacancy on a (111) plane would be less catalytically active than the oxygen vacancy on a (100) plane, or in other words, adsorption and desorption would be stronger on the (100) plane. Yang et al.[6] simulated the conversion of CO over the (111) and the (110) plane of ceria. They observed that the (111) plane held a weak adsorption but the less stable, more reactive plane (110) held both weak and strong adsorptions. The (100) plane was not tested but as this plane is less stable and more reactive than the (110) plane, it was assumed that the (100) plane would hold stronger adsorptions.

Zhou et al.[7] synthesised spherical ceria nanoparticles with the {111} type of surface exposed the most and then synthesised ceria nanorods which produced the {001} and {110} type of plane as the most exposed plane. The spherical ceria nanoparticles had a mean size of 8 nm, and the nanorods had diameters ranging from 13 – 20 nm. The samples were subjected to two cycles of temperature-programmed reduction of hydrogen as the authors stated that this technique was widely used for testing the oxygen redox ability of ceria. The first run showed that the nanoparticles adsorbed thrice the amount of hydrogen compared to the nanorods, suggesting that the nanoparticle had more surface oxygen. The samples were then oxidised with oxygen so that the authors could conduct a second run. The second run showed that the nanoparticle had a significant loss in its reductive ability due to losing ~ 80% of its surface oxygen content. The authors noted that the surface area of the nanoparticles had decreased. Unlike the nanoparticles, the nanorods still had Ce^{4+} reduction ongoing on its surface. These observations show that the redox ability of the nanoparticle significantly reduces after each redox cycle, suggesting that the catalytic ability would also reduce with each cycle.

The authors found that the nanorod gave a better response as a catalyst when compared to the spherical nanoparticles. For example, the authors subjected the nanostructure to CO oxidation to which they reported that the nanorods converted thrice the amount of CO than the nanoparticles. This finding conflicts the general assumptions of what makes a better catalyst. Generally, the structure with the largest surface area to volume ratio and most edges and corners exposed (providing more active sites) would be the better catalyst, as opposed to a structure with a smaller surface area to volume ratio and larger size. The nanorod had a smaller surface area to volume ratio (due to its larger diameter) but still managed to perform better as a catalyst. This is some form of evidence that the type of surface planes may sometimes hold a greater influence on the catalytic ability of the nanostructure, instead of overall size and shape.

2.3 Surface Charge Ratio of Ceria

The ability of ceria to release oxygen at high temperatures, producing vacancies, and to reabsorb oxygen, is highly beneficial for catalytic use. It involves the continual changing of the oxidation state between Ce^{3+} and Ce^{4+}, where a regenerative cycle occurs on the surface of ceria. As mentioned above, oxygen vacancies form when Ce^{3+} is present. These oxygen vacancies allow ceria to be used for oxygen storage where oxygen can be stored (adsorbed) and removed (desorbed). The catalytic activity of this site is increased when there is an ease in the removal of oxygen. In terms of ease, this refers to the site having a low oxygen vacancy formation energy[8], a value which is lower for the less stable (100) plane and generally high for the more stable (111) plane.

Ceria is used in vehicle exhausts as a catalytic converter[8-9], where it oxidises carbon monoxide, hydrocarbons and nitrous oxide compounds. The equations below demonstrate a few of the reactions that occur.

$$CeO_2 + CO \rightleftharpoons CeO_{2-x} + CO_2 \qquad (Equation\ 2)$$

In Equation 2, CeO_2 is reduced to CeO_{2-x} and CO is oxidised to CO_2.

$$CeO_{2-x} + NO \rightleftharpoons CeO_2 + \frac{1}{2}N_2 \qquad (Equation\ 2.1)$$

$$CeO_{2-x} + NO_2 \rightleftharpoons CeO_2 + NO \qquad (Equation\ 2.2)$$

Equations 2.1 and 2.2 are showing the oxidation of CeO_{2-x} to CeO_2 and the reduction of the NO and NO_2 to ½ N_2 and NO respectively.

2.3.1 Surface Charge Ratio and Reactive Oxygen Species

A lot of the catalytic capabilities of ceria has been widely attributed to the surface charge ratio, Ce^{3+}/Ce^{4+}. Ceria can exist in two oxidation states, Ce^{4+} and Ce^{3+}, with Ce^{4+} as the more stable state. Despite this, both states can co-exist on the surface as a result of ceria adopting a cubic fluorite lattice structure. The vicinity of Ce^{3+} and the oxygen vacancies has been found to have a low electrostatic potential[10], indicating that those regions are catalytically active sites. This makes ceria ideal for adsorbing and desorbing a reactive oxygen species (ROS), exhibiting anti-oxidant behaviour and therefore, ideal for use as a catalyst. In addition to this, the low reduction potential of the Ce^{3+}/Ce^{4+} charge ratio[11] means that it is not too difficult for ceria to switch between oxidation states. This also means that the dual ability of ceria to act as an anti-oxidant and an oxidant can be exploited to enhance the effect of one or the other.

A reactive oxygen species (ROS) is a chemical species produced as a by-product of cell metabolism, in which incomplete reduction of oxygen has occurred, producing oxygen related components such as peroxides and radicals[12]. Low levels of ROS are associated with redox reactions involved in cell signalling and are not viewed as toxic[13]. However, oxidative stress occurs when an increased amount of ROS is present within cells, causing damage to DNA and protein, some of which may be permanent. High levels of ROS therefore are thought to contribute to the development of cancer and other diseases such as Parkinson's and Alzheimer's. One way of producing high levels of ROS is when the electron transport

chain outside a mitochondrion is somewhat inhibited to prevent the movement of electrons, causing a build-up of electrons which are eventually collected by oxygen molecules passing by. This results in the formation of a compound containing the superoxide anion radical and consequently, the ROS is formed. As there are multiple oxygen molecules, multiple ROS are formed. These ROS can then move into the nucleus of the cell, disrupting the DNA and cause the cells that are produced to be malignant and cancerous. The ROS is formed as a result of reduction and because the species contains a radical, they remove electrons from any surrounding molecules, causing oxidation. Anti-oxidants would prevent ROS from acting as an oxidising agent and therefore, prevent oxidation from occurring. Removing or decreasing the levels of these ROS by exploiting the anti-oxidant behaviour of ceria is therefore ideal.

According to a review by Schieber et al.[13],a cancer cell will experience an increased metabolism where there will be an elevated production of ROS to promote cell proliferation and signalling. The elevated levels of ROS would still eventually cause the cancer cell to experience an oxidative stress induced cell death, so the cancer cell counters this threat by increasing the anti-oxidant activity. This way, the balance of redox activity is maintained. By introducing an agent that induces the production of ROS, past the point of being able to be controlled by the cancer cell's own anti-oxidant system, this would further impose oxidative stress and lead to cell death[14]. To summarise, preventing high levels of ROS from developing can prevent the formation of cancer, but in the event of cancer occurring, the increased production of ROS would be a possible method of chemotherapy. This method of causing oxidative stress induced cell death by increasing the levels of ROS would need to be a technique where the production of ROS surpasses the standard rate seen in cancerous cells. This is to ensure that the ROS generated does not promote further cell proliferation[13].

Another issue mentioned was that the agents used would need to be able to target the anti-oxidant systems in cancer cells, but avoid the ones used by normal cells. An example of a similar type of behaviour was reported by Hijaz et al.[15], in which the authors conjugated ceria nanoparticle to folic acid in order to target folate receptors and induce their cell death. The authors reported that ceria nanoparticle by itself can induce the production of ROS and when conjugated to folic acid, ROS production was still induced but at lower levels. This is a compromise because the production of more ROS was limited, which would delay the process of oxidative stress induced cell death. However, conjugating a folic acid to ceria would allow the nanoparticle to target specific components and induce cell death by increased uptake of the nanoparticles, whilst avoiding the non-cancerous cells.

An example of another study attempting to induce the formation of ROS for the purpose of cancer cell death is the one reported by Wason et al.[16]. The authors found that an acidic environment in pancreatic cancer cells caused the ceria nanoparticles to induce the formation of ROS. The ceria nanoparticles converted superoxide radicals to form H_2O_2 which removed the damaging radicals from the cancer cell. The continual conversion of radicals to oxygen species led to the accumulation of ROS.

If levels of ROS are not high enough, standard cell proliferation occurs instead of cell apoptosis. For this reason, some studies have opted to investigate the lowering of ROS content as this would prevent any cell signalling and therefore, prevent any more cancerous

cells from being produced. Schieber et al.[13] debated whether increasing the ROS to cause oxidative stress induced cell death or whether lowering the ROS to prevent the mechanism behind the spread of cancer from functioning would be the better option for chemotherapy. Ceria has demonstrated an aptitude to act as an anti-oxidant, attributed to its high Ce^{3+}/Ce^{4+} surface charge ratio. The ability of ceria to switch oxidation state would mean that this anti-oxidant behaviour can be reversed and can be exploited to increase the production of ROS, where this occurrence is desired.

2.3.2 Surface Charge Ratio and Nanomedicine

The ability of ceria to module oxygen has been widely applied in research for potential medical use. One particular study introduced ceria nanoparticles into chicken embryonic cells, to which the damaged blood vessels started to heal. The process of angiogenesis is the formation of new blood vessels from existing blood vessels, which Das et al.[10] were attempting to induce by in vito and in vitro methods. The authors also tested human umbilical vein endothelial cells (HUVEC) for the effect of ceria inducing endothelial tube formation and cell proliferation.

Das et al. tested for endothelial tube formation because this is often an indication that angiogenesis is occurring. They produced two sets of ceria nanoparticles, the difference between the sets was the method of synthesis. The authors found that both sets of ceria nanoparticles induced the formation of these tubes and investigated whether it was the surface Ce^{3+}/Ce^{4+} ratio causing this effect. They tested this by inverting the surface charge of ceria and observed that there was no difference, proving that the surface charge ratio was not the cause for the tube growth. They also observed that the only nanoparticles inducing endothelial tube formation were the ones with a diameter smaller than 15 nm. Specifically, the nanoparticle groups with the size distributions of 3 – 5 nm and 10 – 15 nm. This is perhaps a reflection that the properties intrinsic to nanoparticles are magnified further as the nanoparticle size decreases.

Another observation worth noting is that Das et al. tested the reaction of HUVEC cells, in terms of toxicity, to the ceria nanoparticles. They found that the use of nanorods gave slightly lower levels of cell proliferation compared to the other shapes tested such as the spherical nanoparticles. This may be useful information for cases where angiogenesis is unwanted. However, the reduction in cell proliferation was not huge and so it may be worth investigating ways of exploiting the nanorod to enhance this effect.

Although the induction of endothelial tube formation was not due to the surface charge ratio, the authors still suggested that this ratio induced angiogenesis. They mentioned that a transcription factor used in angiogenesis was heavily influenced by the concentration of oxygen in neighbouring cells, where angiogenesis would occur. By modulating the concentration of oxygen, the effect of the transcription factor inducing angiogenesis would be enhanced. Therefore, ceria nanoparticle induces angiogenesis by modulating the concentration of oxygen, influenced by the surface charge ratio. This in turn, affects the transcription factor used in angiogenesis. The majority of this study was experimental but the authors also conducted a simulation where they investigated how the surface charge ratio modulated the ROS.

The ceria models used in the simulation part of the study were made up of 24,696 atoms. The Ce^{4+} oxidation state is the most stable form and is usually the state that cerium has in a ceria molecule. Ce^{3+} was therefore predicted to be adsorbing the ROS. The authors decided to replace a few Ce^{4+} ions with Ce^{3+} in a region located on a (100) plane on the nanoparticle surface as these planes {100} are less thermodynamically stable than the {111} planes and more susceptible to a reaction. They also decided to visually represent the electrostatic energy of the entire nanoparticle in an attempt to find the areas with the lowest electrostatic energy and consequently, the areas where the desorption of oxygen is likely to occur with the most ease. This was based on their reference that the ease of catalytic desorption of oxygen is due to the electrostatic energy[17]. Their results confirmed their predictions in which the area surrounding Ce^{3+} had the lowest electrostatic energy, indicating that the oxygen in that area would experience an easier removal from the surface compared to the oxygen within the Ce^{4+} regions.

To summarise, Das et al. found that ceria nanoparticle induces angiogenesis by modulating the oxygen concentration, which affects the transcription factor that induces angiogenesis. The cause of this oxygen modulating effect is a result of the surface charge ratio, but it is also worth reminding that the nanoparticle size also determined whether angiogenesis was induced.

Ceria is effective in reversing the oxidative damage caused in cells, which leads to the healing of dermal wounds[18]. Chigurupati et al.[18] synthesised a solution of ceria nanoparticles with particle diameters ranging from 3 – 5 nm. The authors applied the solution of ceria nanoparticles to human keratinocyte cells and mice fibroblast cells, with varying concentrations of ceria. The observation reported was that a higher concentration of ceria increased cell proliferation. The authors also applied the solution to the wounds of mice and observed a faster rate of wound closure in the treated mice, compared to the control mice. In the days following the closure of the wounds, another observation was made in which the mice treated with ceria had a higher level of an immune reaction caused by the protein actin. They eventually concluded that the presence of ceria nanoparticles increases the immunoreactivity by inducing cell differentiation of myofibroblast. Myofibroblast is a combination of a fibroblast, a cell which is commonly found in connective tissue and can produce collagen, and a muscle cell. The presence of this cell is associated with wound healing. The cause of this healing effect observed upon application of ceria nanoparticles was attributed to the anti-oxidant behaviour of ceria, similar to the observation of ceria inducing angiogenesis from the removal of ROS, as mentioned above in the study by Das et al[10].

Hijaz et al.[15] conducted a study in which the anti-cancer behaviour of ceria nanoparticle was observed in multiple ways. To elaborate, the authors produced two types of compound, CNP-FA, which was ceria nanoparticle conjugated to folic acid, and CNP-FA/CisPt, which was CNP-FA combined to cisplatinum. The authors subjected these compounds to multiple tests related to tumour growth, both in vitro and in vivo, to which optimistic results were produced and stated these compounds could be an effective therapeutic agent in ovarian cancer. To summarise, they found that CNP-FA slowed tumour growth without causing any abnormalities in the affected organs to develop (based on a dosage of 0.1 mg/kg twice a week over a period of 4 weeks), and CNP-FA/CisPt enhanced the prevention of tumour

growth, as well as further reducing unwanted angiogenesis and also inducing desired apoptosis.

In this study, the authors chose to use folic acid in order to target the folate receptors in cancer cells. Folate is an essential component in DNA synthesis and is commonly found in tumour tissue, as well as normal tissue. Normal tissue mainly uses a folate carrier to bring folate into the cells, but tumour tissue uses folate receptors for this purpose. These folate receptors are predominantly located in tumour tissue and almost non-existent in normal tissue, making these receptors ideal to be targeted. High levels of folate receptors are detected in patients who have responded negatively to chemotherapy[19], which is even more reason to test the effect of ceria because chemotherapy has toxic side effects, and conjugated ceria therapy may reduce folate receptor expression but also provide less toxic results. There is a lot of research utilising ceria in chemotherapy but the behaviour is not usually targeted or specialised. These authors were using ceria to try and target specific components (folate receptors) by using a folate related component (folic acid).

By conjugating ceria nanoparticle to folic acid, the authors observed a heavily increased uptake of this conjugated compound by the cancer cell, as opposed to using only ceria nanoparticle. This led to the suggestion that using only ceria for cancer treatment would have the cancer cell uptake ceria but not high enough levels to provide an effective treatment. By including a folate related compound, the cancer cell would uptake more of these CNP-FA compounds because the cancer cell is naturally susceptible to the uptake of folate. The increased uptake of these CNP-FA compounds would eventually lead to an internalisation induced cell death.

The authors previously observed that a ceria nanoparticle had no effect on the tumour growth[20] and decided to test whether the same observation would occur for CNP-FA. As there was an increased uptake of CNP-FA into the tumour cell, the authors wondered if this would lead to a side effect of increased cell proliferation. If CNP-FA induced tumour cell growth, then a different approach would be needed. Their results were optimistic and showed that there were no signs of cell proliferation. Instead, they observed an increase in cell death and a reduction in cell viability, caused by an increased uptake of CNP-FA, consequently increased levels of internalisation. In other words, CNP-FA can prevent tumour growth due to decreased cell proliferation and increased cell death. Combining CNP-FA with cisplatinum enhanced these observations further. This is insight into how other types of cancer can be targeted, in which ceria could conjugate to a compound related to the target and induce cell death by increased internalisation.

Cisplatinum was incorporated into their study because it is already being used as a chemotherapy agent in which it binds to DNA, eventually leading to oxidative stress and also causing the activation of caspase-3. Caspase-3 is a marker which promotes cell death. The presence of cisplatinum in a tumour cell activates more caspase-3 than the presence of CNP-FA alone would, but a combination of both compounds activates more of this marker, further promoting cell death. This is further insight into how ceria can be combined with other current chemotherapy agents to target specific cells, minimising cell death of normal cells and therefore, reducing the unwanted side-effects of chemotherapy.

As shown above, Das et al.[10] used ceria to induce angiogenesis in embryonic cells, but Hijaz et al.[15] used ceria to prevent angiogenesis from occurring. This shows that the anti-oxidant and oxidant behaviour in ceria can be exploited according to what the situation is. Angiogenesis is advantageous for damaged tissue but in the study conducted by Hijaz et al.[15] angiogenesis was undesired because the formation of new blood vessels in a tumour would allow oxygen to be brought into the tumour cells. Preventing these blood vessels from forming would restrict the oxygen content and other nutrients being sent to the tumour cells, decreasing cell performance.

2.4 Vibration

There are many types of vibration and different types of vibrational modes. Normal modes is the term used for describing different vibrational motions, with each mode differing in the type of motion observed. Normal modes include the typical molecular vibrations observed in IR spectroscopy, such as the asymmetric and symmetric stretch, bending, wagging, rocking and twisting. A superposition of these normal modes contributes to the overall molecular vibration.

Vibrational modes are discrete and quantised which means they can only occur at specific energy levels and consequently, specific frequencies. Each vibrational mode is observed if the molecule absorbs the frequency that these modes vibrate at. The frequency (and wavenumber) of a vibrational mode can be found from the bond strength and the mass of the particle. The energy of these vibrational modes are related to the quantum harmonic oscillator,

$$E_n = \left(n + \frac{1}{2}\right)\hbar v \qquad (Equation\ 3)$$

where E_n is the energy for the energy level n (quantum number), $\hbar$ is the reduced Planck's constant and v is the frequency. The frequency can be defined as,

$$v = \frac{1}{2\pi}\omega \qquad (Equation\ 3.1)$$

$$\omega = \sqrt{\frac{k}{\mu}} \qquad (Equation\ 3.2)$$

where k is a constant for the bond strength and μ is the reduced mass, which can be defined as,

$$\mu = \frac{m_i m_j}{m_i + m_j} \qquad (Equation\ 3.3)$$

where m is the mass of atoms 'i' and 'j'. Equation 3.1 can therefore be rewritten as,

$$v = \frac{1}{2\pi}\sqrt{\frac{k}{\mu}} \qquad (Equation\ 3.4)$$

The definition relating frequency and wavelength is,

$$\lambda = \frac{c}{v} \qquad (Equation\ 3.5)$$

where c is the speed of light and λ is the wavelength. Substituting Equation 3.4 into Equation 3.5 would give,

$$\lambda = \frac{c}{\frac{1}{2\pi}\sqrt{\frac{k}{\mu}}} \qquad (Equation\ 3.6)$$

$$\lambda = 2\pi c\sqrt{\frac{k}{\mu}} \qquad (Equation\ 3.7)$$

The definition of wavenumber, $\bar{\nu}$, is given as,

$$\bar{\nu} = \frac{1}{\lambda} \qquad (Equation\ 3.8)$$

Substituting Equation 3.7 into Equation 3.8 would give,

$$\bar{\nu} = \frac{1}{2\pi c}\sqrt{\frac{k}{\mu}} \qquad (Equation\ 3.9)$$

The frequency of a normal mode vibration is dependent on the force needed to stretch or compress the bond, also known as Hooke's Law, given by,

$$F = -kx \qquad (Equation\ 4)$$

$$x = r - r_{eq} \qquad (Equation\ 4.1)$$

where F is the force, x is the displacement of the mass from the interatomic distance at equilibrium, r_{eq} is the interatomic distance at equilibrium and r is the interatomic distance after the 'stretch motion' (vibration). At equilibrium, x = 0. When x > 0, the force attempts to bring the displacement back to 0, bringing the interatomic distance back to equilibrium. The negative sign in Equation 4 is to show that the force acts in the opposite direction to the displacement, x. The components of Equation 4.1 are shown visually below in Figure 4.

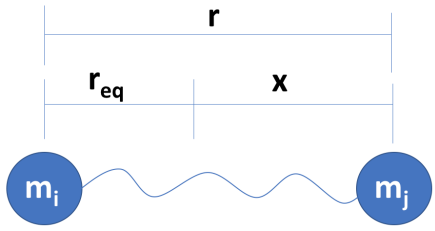

Figure 4: Diagram showing a molecular vibration represented by atoms of mass connected by a 'spring'. The displacement of the atoms 'i' and 'j' with a mass m, during a vibration stretch mode, where r_{eq} is the distance between the atoms at equilibrium, x is the distance gained from the equilibrium position after the vibration stretch and r is the new distance after the vibration.

When a molecule absorbs energy or is excited enough that some of their vibrational modes increase in energy level (n = 0, 1, 2, 3…), the excited vibrational mode is enhanced and observed. At absolute zero temperature, the vibrational modes are not at rest. This is shown in Equation 3 where the zero point energy or the ground state at n = 0, is given to be, $E_0 =$

$\frac{1}{2}\hbar\omega$. This vibrational state is termed the zero point vibration and shows that for a molecule or system related to the harmonic oscillator, the energy of the vibrational modes are not at zero energy and will always have some energy.

For nanoparticles, the morphological differences can cause intrinsic properties to change, changes which could also include frequency. Differing sizes and shapes give different vibrations, vibrations which can be quantified by frequency. This supports the idea that nanoparticle size and shape may be distinguishable from acoustic vibrations by calculating the frequency.

2.4.1 Raman Spectroscopy

Rayleigh scattering is an elastic type of scattering where the energy and wavelength of the incoming photon is the same as the emitted photon. To elaborate, the incoming photon will strike the molecule, causing the molecule to polarise from the ground state to a higher energy level, termed the "virtual" energy state. The molecule then relaxes back to the ground state but releases a photon during this relaxation process. No energy is lost or gained because the molecule was polarised from the ground state and relaxed back to its original state, the ground state. Therefore, the scattered photon is of equal energy and wavelength to the incoming photon, so the Rayleigh scattering process is elastic. This is also termed as a 'scattering' process because the emitted photon can be released in any direction causing a scattering effect.

The Raman effect is similar to the Rayleigh scattering, except that the Raman scattering is inelastic. Two types of Raman scattering are observed, the Stokes scatter and the anti-Stokes scatter. Stokes scattering occurs when an incoming photon polarises the target molecule from the ground state to a "virtual" energy state, but the molecule relaxes to a vibrational state, instead of relaxing back to the ground state. This causes a loss of energy and so the scattered photon is of less energy and longer wavelength than the incoming photon.

$$E_{photon} = hv \qquad (Equation\ 5)$$

Equation 5 is the general formula for the energy of a photon, with E denoting the energy of the photon, h is the Planck constant and v is the frequency.

$$E_{photon} = h\frac{c}{\lambda} \qquad (Equation\ 5.1)$$

Equation 5.1 shows the relation between energy and wavelength, where c is the speed of light and λ is the wavelength. Higher energy would give a smaller wavelength and vice versa.

The anti-Stokes scattering is observed when an incoming photon polarises the molecule from a vibrational state to a "virtual" energy state, to which the molecule then relaxes to the ground state. The molecules observed in an anti-Stokes scatter are originally situated at a vibrational state, and as they are relaxed to the ground state, which is a lower energy level than the vibrational state, this accumulates energy and causes an increase in energy. Resultantly, a shorter wavelength is observed and the emitted photon is higher in energy than the incoming photon.

Rayleigh and Stokes scattering have a higher intensity compared to anti-Stokes scattering, due to the population of molecules in each state. A molecule is more likely to exist in the ground state rather than existing in a state where it is already vibrating, the vibrational states. This can be represented in the equation given below,

$$N \propto exp\left(\frac{-E}{k_B T}\right) \qquad (Equation\ 5.2)$$

where N is the population of molecules, E is the energy, k_B is the Boltzmann constant representing the population and T is the temperature. Equation 5.2 is saying that the population is exponentially proportional to lower energy, which also means that there is less chance of having molecules originally existing in the vibrational states. The latter is the condition needed in an anti-Stokes scatter, but there are less molecules in the vibrational states, which means there is less of an anti-Stokes scatter observed. As the Raman effect is weak, a high sensitivity is often needed to detect these signals.

The spectral resolution defines to what extent an absorption will have merged close lying peaks, or split, sharper peaks. A low spectral resolution will merge close lying peaks and a high spectral resolution would split the peaks, producing sharper and more fine peaks. A high resolution prevents the loss of detail that a low resolution would produce. A low spectral resolution is able to be used for standard sample identification but would be disadvantageous for studies where anisotropic properties are separated by close lying frequencies. Vibrational spectra can tell information about properties such as the size and shape, but also mechanical and material properties, which often require a more intricate level of detail in the peaks to be able to obtain such information from. For this reason, a high spectral resolution is often desired in Raman spectroscopy.

Raman spectroscopy is akin to IR. Generally, IR inactive modes are Raman active so the combination of both techniques would allow for the detection of a wider range of vibrational modes. In IR spectroscopy, IR radiation of varying frequencies (polychromatic) is directed at the molecule. Different vibrational modes occur at different frequencies so if one of these frequencies are directed at the molecule, the radiation of that frequency will be absorbed. The result of this is that the molecule is excited to a higher vibrational energy state. The spectrometer detects the frequencies that have passed through the molecule and also the intensity of the frequencies absorbed by the molecule. The frequency of the vibration is still the same but the amplitude at which the mode moves is now increased. Relaxation back to the ground state occurs accompanied by the emission of heat. In Raman spectroscopy, the incident photon from a monochromatic radiation source interacts with the electron cloud of the molecule, causing a transition from a lower energy state to a ‘virtual’ energy state. Relaxation back to the ground state occurs, in which a photon is emitted and detected. A given vibrational transition will still give the same frequency for both spectroscopic techniques, but the selection rules for each technique means that different vibrational modes are observed.

Raman active modes only occur if there is a change in the polarisability of the molecule. The polarisability can be defined as the tendency of the electrons to be polarised by an applied,

external electric field. The applied electric field in this case is coming from the incoming photon. In other words, the polarisability measures the tendency of the charge distribution (mobility of electrons) in the molecule to be directed in a specific direction. This leads to an induced dipole moment forming, which is given by the formula,

$$\vec{\mu}_{induced} = \alpha\vec{E} \qquad (Equation\ 5.3)$$

where μ is the induced dipole moment, α is the polarisability and E is the applied electric field.

The IR spectroscopic selection rule involves a change in the dipole moment for an IR active mode to occur. The dipole moment in Raman spectroscopy is the "induced" dipole moment, and the one acknowledged in IR spectroscopy is the "permanent" dipole moment. The "permanent" dipole moment is stronger if the charge and the distance between the atoms is larger. A strong dipole moment also means that it is unlikely the electrons will be easily moved to cause polarisation, as the molecule is already strongly polarised, and is therefore likely to give a weak polarisability measurement.

2.4.2 Breathing Mode and Raman Spectroscopy

Breathing modes are a type of vibrational mode involving a contraction and expansion, with all the atoms moving together in the radial direction, usually occurring in the same phase and with the same amplitude. For a fullerene, this vibrational mode involves all the carbon atoms moving synchronously, whereas for a ceria, this mode is most commonly observed as a ring of the oxygen atoms causing the "breathing" motion. The breathing modes of most nanostructures occur in the same phase, but a counter phase breathing motion has been observed for a multi-walled nanotube[21]. This can be described as the inner wall moving together in one phase, whilst the outer wall moves together in a different phase. Breathing modes are caused by phonons and are of the longitudinal acoustic type. As phonons are quantised, the frequency of these breathing modes are also quantised and exist at discrete energy levels. Breathing modes have been observed experimentally, the majority of the literature coming from carbon nanotubes, benzene rings and spherical nanoparticles. According to a review by Ghavanloo, the radial breathing mode occurs within the frequency range of 100 – 500 cm^{-1}.

These vibrational modes are of the symmetric stretch type of mode and occur at low frequencies. A change in the dipole moment is not usually observed for a symmetric breathing mode and therefore, a peak does not usually show for this mode in an IR spectrum. The breathing mode is a Raman active mode and can therefore be observed in Raman spectroscopy.

McBride et al.[9] synthesised ceria compounds with the formula $Ce_{1-x}RE_xO_{2-y}$ where RE represents La, Pr, Nd, Eu, Gd and Tb. These compounds were analysed using X-ray diffraction and Raman spectroscopy. A standard ceria will adopt the cubic fluorite structure and McBride et al. aimed to dope ceria with the "RE" dopants, whilst maintaining the fluorite structure. For this particular type of structure, a Raman active symmetric breathing mode can be observed which they stated as having been caused by a ring of oxygen atoms surrounding the cation. They attributed this vibrational mode to the oxygen atoms as they

stated that it is only these atoms moving. For a bulk ceria, they reported this breathing mode frequency to be given at 465 cm^{-1}.

McBride et al. doped the ceria compounds in an attempt to test whether the ability of ceria to store and release oxygen improved. This was based on the assumption that the oxygen vacancies were causing the increased catalytic activity of the ceria surface. In other words, the replacement of a Ce^{4+} cation with a trivalent cation would also show the same, or ideally an increased, catalytic activity.

Dos Santos et al.[22] synthesised ceria powders consisting of nanoparticles. These particles adopted a spherical morphology and had average diameters ranging from 4.8 - 10.4 nm. They obtained a peak using Raman spectroscopy at 464.5 cm^{-1} which was attributed to the breathing mode. This is in agreement with the breathing frequency obtained for the bulk ceria in the study conducted by McBride et al.[9], but the value has shifted to a slightly lower frequency.

Similar to the study reported by Dos Santos et al.[22], Goharshadi et al. also synthesised powder ceria. The authors produced four samples with average crystallite sizes of 6.45 nm, 5.85 nm, 7.54 nm and 7.27 nm for the first, second, third and fourth samples respectively. These samples produced breathing modes obtained by Raman spectroscopy with frequencies given at 463 cm^{-1} for the first sample and 461 cm^{-1} for the second, third and fourth samples. They also noted that the breathing mode for bulk ceria is known to occur at 464 cm^{-1} and acknowledged the shift of breathing mode frequency to be small when comparing between a bulk and nanoparticle size. The size range of these nanoparticles are similar to the diameters obtained in the study conducted by Dos Santos et al., which is reflected in their observation of breathing modes within the same frequency range.

Babitha et al.[23] synthesised four samples of powder ceria with each sample consisting of ceria nanoparticles of different diameters. Their first, second, third and fourth samples had average diameters of 7.3 nm, 13.56 nm, 18.45 nm and 30.65 nm respectively, which were calcinated during synthesis at temperatures of 400 K, 550 K, 700 K and 850 K respectively. Each sample produced breathing frequencies obtained using Raman spectroscopy to give frequencies at 462.49 cm^{-1}, 464.81 cm^{-2}, 465.9 cm^{-1} and 465.98 cm^{-1} for the first, second, third and fourth samples respectively. The trend observed in this study is that an increasing average diameter caused an increase in the breathing mode frequency. This observation conflicts the trend observed by Goharshadi et al., and deviates from the trend that an increasing diameter causes a lower frequency. The authors have also stated that an increasing calcination temperature leads to greater size distribution amongst the particles. This is perhaps the cause behind the shift in breathing frequency.

Choudhury et al. synthesised ceria nanoparticles with a crystallite diameter of 7.5 nm, and also synthesised Nd doped ceria nanoparticles of percentage Nd doping at 1.0%. 2.5% and 4.0% giving crystallite sizes of 6.4 nm, 5.2 nm and 4.0 nm respectively. Their non-doped ceria nanoparticles produced a breathing mode frequency of 462.15 cm^{-1}, which is within the standard range observed by the above mentioned studies[1, 22]. For the Nd doped ceria nanoparticles, the breathing mode frequency was given at 455.73 cm^{-1}. Again, these frequency values are in good agreement with the bulk counterpart but shifted slightly.

To summarise, McBride et al. obtained a Raman active breathing mode frequency for bulk ceria given at 465 cm^{-1} and the more recent literature obtained a Raman active breathing frequency for ceria nanoparticles given between 461 – 464 cm^{-1}. The values show that the breathing frequency of a ceria nanoparticle is almost identical to the one given for the bulk ceria, but is shifted a few wavenumbers. Choudhury et al.[24] calculated this Raman shift using a formula derived by Li et al. [25] and obtained a shift of 1.85 cm^{-1} for pure ceria. In other words, a non-doped ceria nanoparticle will shift around 1.85 cm^{-1} from the breathing frequency of its bulk counterpart.

Breathing modes can be resonantly excited. A resonant vibration is one which has been induced by an external force, driving the vibration to occur by exciting the subject to oscillate at a specific frequency, but with an increased amplitude. When the energy (and frequency) of the incident radiation "matches" the energy (and frequency) of the subject's natural oscillations, the subject will resonantly vibrate at a greater amplitude. Resonance Raman is another form of spectroscopy which can produce resonant vibrations allowing for the magnitude of the scattering to increase, enhancing the detection of low frequency signals.

2.4.3 Breathing Modes and Ultra-fast Spectroscopy

Breathing modes occur at low frequencies, some of which have been shown to be excited from radiation within the IR region of the electromagnetic spectrum. However, as this mode is a symmetric stretch type of vibrational mode, a change in the dipole moment is not often observed. This would make the mode IR inactive and resultantly, the majority of literature probing breathing modes use Raman spectroscopy. However, ultra-fast spectroscopy is another technique that has been used to observe breathing modes of nanoparticles.

Ultra-fast pump-probe spectroscopy is a method of optical excitation in which the first pump laser pulse excites the electrons in the sample, and the time delayed second probe pulse monitors the absorbance over time. It is sometimes termed as the 'transient absorption pump-probe' technique as the sample may be monitored at time intervals. A different lens is used to focus each laser. The ultra-fast laser excites the electrons, causing the lattice to heat up, leading to a breathing mode occurring. In other words, the energy from the laser pulse absorbed by the electrons is transferred to the lattice[26]. The lattice is then cooled as the heat from the particles diffuse away. The first pump laser causes the excitation and the second laser, the probe, modulates the resulting motion. The intensity of the laser probe is modulated by tuning to a frequency the breathing mode occurs in, so that the incident radiation of that specific frequency can get absorbed. The remaining frequencies are transmitted and detected by a photodiode from which the absorbed frequencies can be identified by observing the intensities.

Hodak et al.[27] obtained acoustic breathing modes from metallic nanoparticles of diameters ranging 2 – 120 nm using this spectroscopic technique. They investigated single Au nanoparticles, as well as bimetallic nanoparticles comprising combinations from elements such as Au, Ag, Pt and Pb. These bimetallic compounds had a metallic core of one element and a shell of a different metallic element. The authors found that an increase in the particle diameter caused a decrease in the frequency, which was reflected from their range of

results including a gold particle of 8.3 nm having a frequency of 11.6 cm^{-1} and a gold particle of diameter 120 nm with a frequency of 1.0 cm^{-1}.

Ruijgrok et al.[28] used this spectroscopic method to observe the acoustic vibrations of gold nanoparticles immersed in water. In addition to the pump-probe lasers, the authors used a near IR laser of wavelength 1064 nm to optically trap the nanoparticles. This IR laser prevented the nanoparticles from moving around in water, allowing them to be subjected to the pump-probe method for several hours. The nanoparticles they examined were gold nanospheres of diameters around 80 nm and gold nanorods with dimensions around 25 nm width by 60 nm length. They detected a breathing mode from the nanospheres at 40 ± 0.3 GHz and the breathing mode obtained for the nanorods was given at 73 ± 0.7 GHz.

Pelton et al.[26] conducted a similar study by synthesising bipyramidal gold nanoparticles in different solvents and characterised them using TEM. These particles were probed using ultra-fast pump-probe spectroscopy to observe the acoustic vibrations. The frequencies were reported to occur from 16 – 20.6 GHz. The authors also simulated the breathing mode vibration of bipyramid gold nanoparticles, with diameters of the models to match the diameters obtained from their TEM results. The simulated frequencies obtained ranged from 13.8 – 19.8 GHz and are in good agreement with their experimental data.

Juve et al.[29] also used the pump-probe technique to probe the breathing modes of platinum and silica embedded platinum nanoparticles. These nanoparticles had diameters ranging from 1.3 – 3 nm and gave breathing mode frequencies of 1.1 – 2.6 THz. They observed the period of the breathing modes and found that the silica embedded and non-embedded nanoparticles provided similar results, suggesting that the silica encapsulation had little effect on the duration of the breathing mode. The authors therefore attributed the oscillation decay to the natural dephasing of the in phase breathing motion.

A single nanoparticle scatters the photon weakly and is therefore, difficult to detect or obtain a sufficient reading for when using Raman spectroscopy. Wheaton et al.[30] found a method for observing these weakly scattered signals from single nanoparticles such as polystyrene and titanium dioxide, with diameters ranging 20 - 50 nm, using “Extraordinary acoustic Raman” spectroscopy. The “Extraordinary” part of the name is a reference to the high resolution adopted in their study, which was ~ 0.5 cm^{-1}. This method involved using two lasers with each laser beating at a single, differing frequency. The authors used a combination of acoustic Raman spectroscopy and an ultra-fast technique, optical Kerr spectroscopy, the latter of which, bases its mechanism on inducing an electrostriction force. An electrostriction force is one that applies an electric field, causing the positive ions to displace towards the direction of the applied field, and the negative ions to displace in the opposite direction, leading to strain and consequently, a change in the particle shape. This force is produced by the two lasers and is tuned to the acoustic resonance of the nanoparticle, causing the nanoparticle to resonantly oscillate and thus, a resonant vibration occurs. The change in the thermal motion is then able to be recorded. This technique of measuring the thermal motion characteristic of vibrations instead of the emitted photon allows for the previously, weak Raman signals to be detected using a higher resolution.

For a high-resolution system, the resolution is generally around 1 cm^{-1}. In addition to this, an interference notch filter is often needed to filter out the Rayleigh scattering, which provides a much stronger signal than the Raman signals. This filter prevents the Rayleigh signal from being detected but the disadvantage is that the vibrations of frequencies below 10 cm^{-1} are also filtered out. This means that the nanoparticles that give vibrations above 10 cm^{-1}, in other words, smaller nanoparticles, are the only ones that can be detected using conventional Raman spectroscopy. Therefore, the acoustic vibrations from larger nanoparticles including quantum dots, proteins, DNA and other biomolecules may be filtered out. Wheaton et al. used a resolution of ~ 0.5 cm^{-1}. The 'extraordinary resolution' allowed them to obtain Raman frequencies of 0.7 – 10 cm^{-1}, due to their method of measurement. Unlike conventional Raman spectroscopy, the authors directly measured the fluctuations of the thermal motion of the nanoparticle. This meant that the scattered light was not measured and therefore, there was no need for filtering out the Rayleigh scattering.

The authors first tested this method on polystyrene nanoparticle with a diameter of 20 nm, obtaining frequencies of 44 GHz (1.47 cm^{-1}) and 68 GHz (2.28 cm^{-1}). The peak at 68 GHz was stated as having been caused by a breathing mode. They then tested titanium dioxide with a diameter of 20.5 nm, obtaining frequencies of 158.5 GHz (5.29 cm^{-1}) and 165.8 GHz (5.52 cm^{-1}).

Wheaton et al. obtained the Raman active modes of titanium dioxide, polystyrene and globular proteins. These molecules produced characteristic vibrational spectra which means that these components, in particular the proteins, may be able to be detected in aqueous solutions or other media. This would assist in the identification of pathogens, in which the proteins that are characteristic of these pathogens could be identified from the resonant vibrations. One of the modes detected was a breathing mode which suggests that their technique could be used as a method for measuring the breathing modes of other nanoparticles. This particular spectroscopic method would therefore, also be able to lead to information about the size, shape and material properties from the probed breathing modes.

2.4.4 Breathing Mode and Nanoparticle Shape

Different types of nanoparticle shape and nanostructure give rise to different breathing mode frequencies. This is reflected by multiple studies in which formulas have been developed for determining the breathing mode frequency of their respective nanostructures. The review on radial breathing modes conducted by Ghavanloo stated that the studies mentioned the radial breathing mode frequency to decrease with increasing diameter. This is reflected in the formula composed by Jishi et al.[31],

$$\omega_{RBM} = \frac{A}{d} \qquad (Equation\ 6)$$

where ω_{RBM} is the frequency of the radial breathing mode, A is a constant and d is the diameter. The main advantage of being able to determine the diameter was that the chirality of the single walled carbon nanotubes could also be determined. This is one example of how finding the diameter and size of the nanotube from its radial breathing mode frequency can be applied to identifying other properties. A more detailed formula for the frequency of a radial breathing mode is shown below,

$$\omega = \frac{\tau}{R}\sqrt{\frac{E(1-v)}{\rho(1+v)(1-2v)}} \qquad (Equation\ 6.1)$$

where ω is the breathing mode frequency of a nanowire, τ is the eigenvalue, R is the radius, E is the Young's modulus, v is the Poisson's ratio of the nanowire and ρ is the density. Equation 6.1 was taken from reference[32].

$$\omega = \frac{1}{R}\sqrt{\frac{E}{\rho(1-v^2)}} \qquad (Equation\ 6.2)$$

Equation 6.2 represents the breathing mode frequency of a single walled carbon nanotube and was taken from reference[33]. Although Equation 6.1 and Equation 6.2 were derived from different authors, it is shown that the breathing mode of a nanowire and a single walled carbon nanotube is similar as the formula for the frequencies are also similar. The difference between the two equations is that the formula for the breathing frequency of a nanowire is accounting for a solid cylindrical shape, which is reflected by the formula having more components to consider. A single walled carbon nanotube is a hollow tube and the breathing mode frequency has a less complex definition.

Formulas for the breathing mode frequencies are given for other types of nanostructures in the review by Ghavanloo, all of which differ but have the common component that the frequency is inversely proportional to the radius.

A study by Szilagyi et al.[34] observed breathing mode excitations by conducting femtosecond X-ray scattering on a ~ 100 nm thick nanocrystal layer comprising CdSe spherical nanoparticles with diameters of 3.4 nm, and CdS rod shaped nanoparticles with dimensions of 4.5 nm x 18 nm. These nanocrystals were positioned on a thin SiN membrane. They used optical pulses with wavelengths of 400 nm to optically excite these nanocrystals and observed the shape changes as a result of strain. The authors found that as the nanocrystals were excited highly above their band gap, a breathing mode vibration was induced. The motivation for the authors' study was based on the knowledge that the stress and strain (shape change) response of a nanocrystal changes as the size changes. Stress and strain affects the mechanical properties which means that these properties are also size dependent. Using these nanocrystals to produce nanoscale thin films would mean that the function of these films are dependent on the mechanical properties, as a result of the characteristic stress and strain response.

When Szilagyi et al. excited the CdSe nanospheres, a short lived, symmetric strain was produced, indicating the occurrence of a breathing mode. Different crystallographic directions were probed and each resulting breathing mode produced gave a near identical response. This meant that the induced strain was isotropic for the nanosphere. The duration of the breathing mode excitation was calculated to be ~ 1.1 ps.

Probing the CdS nanorods also produced strains observed as breathing modes. As with the nanospheres, the strain was short lived and gave rise to a breathing mode response from the observation of a radial expansion and contraction. However, unlike the nanospheres, the amplitude of the nanorod breathing modes were demonstrated to be anisotropic. Different crystallographic directions produced strain responses (breathing modes) of varying levels of intensity. In the case of the nanorod, a breathing mode is produced in full effect when the plane being probed is positioned with a component along the radial direction, the direction in which the breathing mode occurs. For a plane (hkl) not orthogonal to the radial direction, the effect is less observed and the planes do not expand or contract with as high of an amplitude. In the case of their study, this meant that an enhanced breathing mode response was induced when the optical pulses were aimed at planes such as the (100) and the (110), as these sets of planes were perpendicular to the radial direction. Also reflected in their results was the (002) plane producing the radial expansion with the least amplitude, as this plane was perpendicular to the long axis, and not to the radial direction.

2.4.5 Phonons and Thermal Conductivity

Phonons are the quantised vibrational energy of a lattice. They can occur in bulk crystals as well as within a nanoparticle. In crystalline structures, the bonds between the atoms prevent any chance of a significant vibration developing from single atoms. Consequently, the lattice vibrations are said to arise from a collective of vibrational modes, propagating through the structure. These vibrational modes are only able to receive energy in discrete, quantised amounts, or known as phonons.

$$\epsilon = \hbar\omega \qquad (Equation\ 7)$$

Equation 7 shows the energy of a phonon, where ϵ is the energy, n is the $\hbar$ is the Planck constant over π and ω is the angular frequency.

As mentioned above, the radial breathing mode frequency can determine the diameter of the nanotube. This can also be shown in terms of the phonon energy[35],

$$\hbar\omega = \frac{meV}{R} \qquad (Equation\ 7.1)$$

where $\hbar\omega$ is the phonon energy, R is the radius of the nanotube and meV is the electron volt unit for the measured energy.

Phonons can be acoustic or optical. An acoustic phonon will occur at a low frequency where the atoms of the crystal are moving in phase to each other, in the same direction and of the same amplitude. Acoustic phonons are termed as such as they are long wavelength acoustic vibrations which can behave like sound waves. Optical phonons occur at higher frequencies, and is termed ‘optical’ as they can be excited by radiation with a frequency in the IR region. An optical phonon occurs with the atoms of the crystal moving out of phase to each other, in different directions and sometimes different amplitudes.

If p is the number of atoms in a primitive cell, then 3p is the total number of phonon branches for that crystal. The number of acoustic and optical branches can be determined using the formula 3p – 3, which gives the number of optical branches. There are 3 modes for

the acoustic branch. For each phonon wave vector, there are also longitudinal and transverse modes, including the longitudinal optical mode, transverse optical mode and the same for acoustic phonons. For an N number of the total number of primitive cells, 3pN gives the total phonon modes.

These branches can be represented graphically within the first Brillouin zone, with frequency as a function of the phonon wavevector K and boundaries of $-\frac{\pi}{a}$ and $+\frac{\pi}{a}$, where 'a' is the spacing between the sets of planes. It is also worth noting that 'a' represents the repeat distance from one type of plane to another plane of the same type, and not representing the distance between nearest neighbour planes. Any displacement or wavevector outside of this boundary can be treated so it is described by a wavevector within the first Brillouin zone.

Equation 4 above gives the formula for the force acting on an atom during a vibration (Hooke's law), which can be adjusted in terms of the lattice vibration caused by a phonon to give the below expression,

$$F_s = C(U_{s+1} - U_s) + C(U_{s-1} - U_s) \qquad (Equation\ 7.2)$$

where F_s is the force acting on the plane of atoms, s, C is the force constant, U_s is the displacement of plane s from the equilibrium position, U_{s+1} is the displacement of plane s at +1 and U_{s-1} is the displacement of plane s at -1. Equation 7.2 only accounts for the force on plane s from the nearest neighbour interactions, which involve the planes at ± 1 from plane s.

Phonons are thought to contribute to the lowering of thermal conductivity in materials at the nanoscale and this has been attributed to phonon scattering[36]. This is particularly useful for the field of thermoelectrics where thermoelectric devices comprise of a hot semiconductor junction and a cold semiconductor junction connected to one another. This produces a temperature gradient which allows a voltage to be produced. A low thermal conductivity of the material at the hot junction would prevent any thermal energy from transferring to the cold junction, which would maintain the temperature gradient. Thermoelectric devices currently operate at very low efficiencies which prevents their application in industry or the consumer market. Observing the mechanism of how phonons lower the thermal conductivity and enhancing this effect would increase the efficiency of thermoelectric devices.

A thermal conduction is based on contributions from both phonons and electrons, and in metals, the electrons are the dominant carrier of thermal energy so the contribution to thermal conductivity is mainly electron based. For non-metals, there are less free electrons for an electron based conduction to be dominant, so the phonons have a greater contribution to thermal conductivity. For metals, an electron based conduction is dominant in both thermal and electrical conduction. The Wiedemann-Franz law describes the electronic contribution to both forms of conduction in a relationship between the ratio of thermal and electrical conductivity as a function of temperature, disregarding any phonon contribution, as shown below,

$$LT = \frac{\kappa}{\sigma} \qquad (Equation\ 7.3)$$

where L is the proportionality constant (Lorenz number), T is the temperature, κ is the thermal conductivity and σ is the electrical conductivity. It is also worth noting the relationship between kinetic energy and temperature,

$$\frac{1}{2}mv^2 = \frac{3}{2}k_B T \qquad (Equation\ 7.4)$$

where m is the mass of the electron, v is the velocity, k_B is the Boltzmann constant and T is the temperature.

As shown in Equation 7.4, as temperature increases, the kinetic energy increases, in particular, the velocity. Electrons maintain charge neutrality during thermal conduction so there is no net movement. As the velocity of the electrons increase, they travel around the lattice at a faster rate. These electrons are carrying thermal energy so it would mean that they are also colliding with the lattice ions and transferring the thermal energy to these ions at a faster rate. As a result, thermal conductivity increases.

Contrastingly for electrical conductivity, a higher average electron velocity would cause a decrease in electrical conductivity. The electrons would collide with the lattice ions at a high velocity, increasing the likelihood of a diversion from the electrons' pathway towards the negative charge. This prevents a forward transport of charge and as a result, a lowering in the electrical conductivity.

2.5 References

1. E. K. Goharshadi, S. Samiee, P. Nancarrow, Journal of Colloid and Interface Science, 2011, vol 356, pp. 473 – 480
2. J. A. Martinez, D. E. Yilmaz, T. Liang, S. B. Sinnott, S. R. Phillpot, Current Opinion in Solid State and Materials Science, 2013, vol 17, pp. 263 – 270
3. G. Pulido-Reyes, I. Rodea-Palomares, S. Das, T. S. Sakthivel, F. Leganes, R. Rosal, S. Seal, F. Fernandez-Pinas, Sci. Rep., 2015, vol 5, pp. 15613
4. M. Baudin, M. Wojcik, K. Hermansson, Surface Science, 2000, 468, pp 51-61
5. Z. L. Wang, X. Feng, J. Phys. Chem. B, 2003, vol 107, pp 13563-13566
6. Z. Yang, T. K. Woo, K. Hermansson, Chem. Phys. Lett., 2004, vol 396, pp. 384 – 392
7. K. Zhou, X. Wang, X. Sun, Q. Peng, Y. Li, Journal of Catalysis, 2005, vol 229, pp. 206 – 212
8. T. X. T. Sayle, F. Caddeo, X. Zhang, T. Sakthivel, S. Das, S. Seal, S. Ptasinska, D. C. Sayle, J. Am. Chem. Soc., 2016, vol 28, pp. 7287 – 7295
9. J. R. McBride, K. C. Hass, B. D. Poindexter, W. H. Weber, J. Appl. Phys., 1994, vol 76, pp. 2435
10. S. Das, S. Singh, J. M. Dowding, S. Oommen, A. Kumar, T. X. T. Sayle, S. Saraf, C. R. Patra, N.E. Vlahakis, D. C. Sayle, W. T. Self, S. Seal, Biomaterials, 2012, vol 33, pp. 7746 – 7755
11. A. Karakoti, S. Singh, J. M. Dowding, W. T. Self, Chem. Soc. Rev., 2010, 39(11), pp. 4422 – 4432
12. B. D'Autreaux, M. B. Toledano, Nature Reviews, 2007, vol 8, pp 813 - 824
13. M. Schieber, N. S. Chandel, Current Biology, 2014, 24, 453 – 462
14. P. Schumacker, Cancer Cell, 2006, vol 10, pp. 175-176
15. M. Hijaz, S. Das, I. Mert, A. Gupta, Z. Al-Wahab, C. Tebbe, S. Dar, J. Chhina, S. Giri, A. Munkarah, S. Seal, R. Rattan, BMC Cancer, 2016, vol 220, pp. 220
16. M. S. Wason, J. Colon, S. Das, S. Seal, J. Turkson, J. Zhao, C. H. Baker, Nanomedicine, 2013, 9(4), pp. 558 – 569
17. A. Migani, G. N. Vayssilov, S. T. Bromley, F. Illas, K. M. Neyman, J. Mater. Chem., 2010, vol 20, pp. 10535 – 10546
18. S. Chigurupati, M. R. Mughal, E. Okun, S. Das, A. Kumar, M. McCaffery, S. Seal, M. P. Mattson, Biomaterials, 2012, 39(9), pp. 2194 – 2201
19. Y. L. Chen, M. C. Chang, C. Y. Huang, Y. C. Chiang, H. W. Lin, C. A. Chen, C. Y. Hsieh, W. F. Cheng, Mol. Oncol., 2012, 6(3), pp. 360 – 369
20. S. Giri, A. Karakoti, R. P. Graham, J. L. Maguire, C. M. Reilly, S. Seal, R. Rattan, V. Shridhar, PLoS One, 2013, 8(1), pp. 54578
21. E. Ghavanloo, S. A. Fazelzadeh, H. Rafii-Tabar, International Materials Reviews, 2015, vol 60, pp. 312 – 329
22. M. L. Dos Santos, R. C. Lima, C. S. Riccardi, R. L. Tranquilin, P. R. Bueno, J. A. Varela, E. Longo, Materials Letters, 2008, vol 62, pp. 4509 – 4511
23. K. K. Babitha, A. Sreedevi, K. P. Priyanka, B. Sabu, T. Varghese, Indian Journal of Pure and Applied Physics, 2015, vol 53, pp. 586 – 603

24. B. Choudhury, A. Choudhury, Current Applied Physics, 2013, vol 13, pp. 217 – 223
25. G. R. Li, D. L. Qu, L. Arurault, Y. X. Tong, J. Phys. Chem. C., 2009, 113, pp. 1235 – 1241
26. M. Pelton, J.E. Sader, J. Burgin, M. Liu, P. Guyot-Sionnest, D. Gosztola, Nat. Nanotechnol, 2009, vol 4, pp. 492-495
27. J. H. Hodak, A. Henglein, G. V. Hartland, J. Phys. Chem. B., 2000, vol 104, pp. 9954 – 9965
28. P. V. Ruijgrok, P. Zijlstra, A. L. Tchebotareva, M. Orrit, Nano Letters, 2012, vol 12, pp. 1063 – 1069
29. V. Juve, A. Crut, P. Maioli, M. Pellarin, M. Broyer, N. D. Fatti, F. Vallee, Nano. Lett., 2010, vol 10, pp. 1853 - 1858
30. S. Wheaton, R. M. Gelfand, R. Gordon, Nature Photonics, 2014, vol 9, pp. 68 – 72
31. R. A. Jishi, L. Venkataraman, M. S. Dresselhaus, G. Dresselhaus, Chem. Phys. Lett., 1993, vol 209, pp. 77
32. M. Hu, X. Wang, G. V. Hartland, P. Mulvaney, J. P. Juste, J. E. Sader, J. Am. Chem. Soc., 2003, 125, pp. 14925 – 14933
33. S. Basirjafari, S. Esmaielzadeh Khadem, R. Malekfar, International Journal of Engineering, 2012, vol 26, pp. 447 - 454
34. E. Szilagyi, J. S. Wittenberg, T. A. Miller, K. Lutker, F. Quirin, H. Lemke, D. Zhu, M. Chollet, J. Robinson, H. Wen, K. Sokolowski-Tinten, A. M. Lindenberg, Nature Communications, 2015, 6:6577, DOI: 10.1038/ncomms7577
35. C. Kittel, Introduction to Solid State Physics 8th Edition, John Wiley & Sons, Inc, New Jersey, U.S.A, 2005
36. M. Schrade, K. Berland, S. N. H. Eliassen, M. N. Guzik, C. Echevarria-Bonet, M. H. Sorby, P. Jenus, B. C. Hauback, R. Tofan, A. E. Gunnaes, C. Persson, O. M. Lovvik, T. G. Finstad, Scientific Reports, 2017, vol 7, pp. 13760

Chapter 3: Methods

3.1 Molecular Dynamics

Molecular Dynamics is a computational simulation technique modelling the motion and forces between molecules over a given time period. This process attempts to model how a system of particles would react under specific conditions, which are set by adjusting parameters such as the temperature and pressure. The algorithms work by applying classical mechanics to molecular systems, involving the integration of Newton's equation of motion to relate the positions of the atoms and velocities. Before any molecular dynamics simulation is able to be conducted, the initial velocities and positions of the atoms, as well as the pair-interaction potentials, needs to be defined.

3.2 Newton's Second Law and Application

In this sub section, the process for assigning the initial velocities and positions to the atoms is documented and then the process for obtaining the temperature of the system follows.

3.2.1 Forces, Leapfrog Algorithm, Initial Velocities, Positions

This sub section briefly describes the calculation of the forces, from which Newton's law can then be applied via integration to find the positions and velocities of the atoms. The energy of the interaction from the pair of atoms (potentials) can be used to calculate the forces acting on the atoms.

Starting with Newton's equation of motion,

$$\boldsymbol{F} = m\boldsymbol{a} \qquad (Equation\ 8)$$

where F is the force ($F_x = ma_x$, $F_y = ma_y$, $F_z = ma_z$), m is the mass of the atom and a is the acceleration in the (x, y, z) direction.
The formula for acceleration can be defined as the change in the velocity, V, over the change in time, t,

$$\boldsymbol{a} = \frac{d\boldsymbol{V}}{dt} \qquad (Equation\ 8.1)$$

Therefore, Equation 8 can be rewritten as,

$$\boldsymbol{F} = m\frac{dV}{dt} \qquad (Equation\ 8.2)$$

$$\boldsymbol{F} = m\frac{d^2\boldsymbol{r}}{dt^2} \qquad (Equation\ 8.3)$$

where r is the position of the atom. The force can be derived[1] in terms of potential energy to give,

$$\boldsymbol{F}_{ij} = -\frac{\partial}{\partial r_{ij}} U(\boldsymbol{r}_{ij}) \qquad (Equation\ 8.4)$$

where F_{ij} is the force of the atom pair 'i' and 'j' and $U(r_{ij})$ is the potential energy interaction between the atom pair 'i' and 'j'. The $U(r_{ij})$ term is taken from Equation 15.2 in the 'Potentials' sub section which is described in more detail further down this chapter. A vector sum can then be used to calculate the force of all the atoms, N, in the system, using a formula,

$$\sum_{i=1}^{N-1}\sum_{j>i}^{N} U_{pair}\left(i, j, \left|r_i - r_j\right|\right) \qquad (Equation\ 8.5)$$

where 'i' and 'j' are the atoms, U is the energy of the pair of atoms and r is the position of these atoms. The term 'j > i' prevents the double counting of the pair of atoms. Equation 8.5 was taken from the DLPOLY manual[2] and shows that the interactions of the system depend on the positions of the atoms.

An integration algorithm is implemented to find the initial positions and velocities of the atoms by integrating Newton's equation of motion. A range of integration algorithms are used in the DLPOLY code but the ones used in this study are based on the Verlet type of algorithm[2], where the two types including the Verlet leapfrog and the velocity Verlet. In this study, the leapfrog algorithm was used. The term 'leapfrog' is a reference to the velocities being calculated half a timestep behind, which corrects the timestep error obtained for the basic Verlet algorithm. This is described below, starting with the Verlet algorithm, in which a Taylor series expansion[1] is adopted to produce the formula,

$$\boldsymbol{r}(t + \Delta t) = \boldsymbol{r}(t) + \boldsymbol{v}(t)\Delta t + \frac{1}{2m}\boldsymbol{f}(t)\Delta t^2 + \cdots \Delta t^4 \qquad (Equation\ 9)$$

$$\boldsymbol{r}(t - \Delta t) = \boldsymbol{r}(t) - \boldsymbol{v}(t)\Delta t + \frac{1}{2m}\boldsymbol{f}(t)\Delta t^2 - \cdots \Delta t^4 \qquad (Equation\ 9.1)$$

where r is the position of the atoms, t is the timestep, v is the velocity, m is the mass of the atom and f is the force. There is an error in the timestep, which is large (Δt^4) and causes unnecessary fluctuations in the calculated energies, so the leapfrog version[2] is used to obtain velocities at half a timestep which are given by,

$$\boldsymbol{v}\left(t + \frac{1}{2}\Delta t\right) = \boldsymbol{v}\left(t - \frac{1}{2}\Delta t\right) + \frac{1}{m}\boldsymbol{f}(t)\Delta t \qquad (Equation\ 9.2)$$

These new velocities are then used to find the positions, given by,

$$\boldsymbol{r}(t + \Delta t) = \boldsymbol{r}(t) + \boldsymbol{v}\left(t + \frac{1}{2}\Delta t\right)\Delta t \qquad (Equation\ 9.3)$$

The velocities at a time t can then be given by,

$$\boldsymbol{v}(t) = \frac{1}{2}\left[\boldsymbol{v}\left(t - \frac{1}{2}\Delta t\right) + \boldsymbol{v}\left(t + \frac{1}{2}\Delta t\right)\right] \qquad (Equation\ 9.4)$$

which describes the velocity being calculated from the average of the velocities on one half

of the time step, and also the average of velocities from the other half of the timestep.

3.2.2 Kinetic model, Temperature of the System

Starting with the most basic expression for momentum,

$$\boldsymbol{p} = m\boldsymbol{v} \qquad (Equation\ 10)$$

where **p** is the momentum (p_x, p_y, p_z) , m is the mass of the object and **v** is the velocity (v_x, v_y, v_z) . Newton's second law states that the rate of change of momentum of an object is proportional to the net force acting on it. Linking in with Newton's first law, if the net force is equal to zero, then the momentum of the object is unchanged and the object will continue on its path of uniform motion or stay at rest. Similar to how an alternative way of expressing the change in kinetic energy is in the form of 'force x distance', the change in momentum can also be expressed in the form of 'force x time',

$$\boldsymbol{F}t = m(\boldsymbol{v} - \boldsymbol{u}) \qquad (Equation\ 10.1)$$

where F is the force, t is the time, m is the mass of one molecule, v is the final velocity and u is the initial velocity. This expression can be rearranged to give F as a proportionality,

$$\boldsymbol{F} \propto \frac{\Delta \boldsymbol{p}}{\Delta t} \qquad (Equation\ 10.1.1)$$

where Δp is the change in the momentum and Δt is the change in the time. Another way of expressing this is,

$$\boldsymbol{F} = \frac{m(\boldsymbol{v} - \boldsymbol{u})}{t} \qquad (Equation\ 10.1.2)$$

From the "SUVAT" equations, acceleration, a, can be defined as,

$$\boldsymbol{a} = \frac{\boldsymbol{v} - \boldsymbol{u}}{t} \qquad (Equation\ 10.2)$$

which can be subbed into Equation 10.1.2 to give the commonly known expression for Newton's second law,

$$\boldsymbol{F} = m\boldsymbol{a} \qquad (Equation\ 10.3)$$

The following account shows a general summary as to how the pressure of a gas can be found from the application of Newton's second law.

Consider a 3D cubic box with length, d, in the (x, y, z) direction, or to rephrase, the length, width and height are all a value of d. A molecule with a mass of m and a velocity of v is moving in this box. Assuming the collision to be elastic, the momentum of the molecule's movement will be 2mv if it travelled from one side of the box to the other side and back i.e. travelling in the x direction and then back along the –x direction. The momentum changes from 'mv with respect to the x direction', and then 'mv with respect to the –x direction'. If the molecule was to produce another collision with the wall, the distance to accomplish this

collision would be 2d. Therefore, the time taken for a collision to occur (based on the 'speed = distance/time' generic equation) is,

$$t = \frac{2d}{v_x} \qquad (Equation\ 10.4)$$

where t is the time, 2d is the distance travelled and v_x is the velocity in the x direction. Equations 10.1.1 and 10.1.2 describe the definition for force being proportional to the rate of the change of momentum, so we can substitute in $2mv_x$ for the change in momentum, and Equation 10.4 for the time to get,

$$\boldsymbol{F} = \frac{2mv_x}{\left(\frac{2d}{v_x}\right)} \qquad (Equation\ 10.5)$$

which simplifies to,

$$\boldsymbol{F} = \frac{m{v_x}^2}{d} \qquad (Equation\ 10.5.1)$$

The generic equation for pressure is 'pressure = force/area'. The area of a face of the box would be d^2. This would express pressure, P, as follows,

$$P = \frac{m{v_x}^2}{\frac{d}{(d^2)}} \qquad (Equation\ 10.6)$$

which simplifies to,

$$P = \frac{m{v_x}^2}{d^3} \qquad (Equation\ 10.6.1)$$

To account for all the molecules in the cube, N is included, and to account for an average over all of the velocities in the x direction, a bar is added,

$$P = \frac{m}{d^3} N\overline{v_x}^2 \qquad (Equation\ 10.6.2)$$

The generic equation for density is 'density = mass/volume'. This would give an expression for density as,

$$\rho = \frac{Nm}{d^3} \qquad (Equation\ 10.6.3)$$

where ρ is the density, Nm is the total mass and the volume is d^3. Comparing Equations 10.6.2 and 10.6.3, pressure can be simplified to,

$$P = \rho\overline{{v_x}^2} \qquad (Equation\ 10.6.4)$$

Equation 10.6.4 considers velocity for all molecules in the x direction. To account for the y and the z directions, a Pythagoras calculation gives the velocity as follows:

$$\overline{{v_x}^2} = \overline{{v_y}^2} = \overline{{v_z}^2} \qquad (Equation\ 10.6.5)$$

The average velocity squared in each direction (x, y, z) is equal.

$$\overline{v^2} = \overline{{v_x}^2} + \overline{{v_y}^2} + \overline{{v_z}^2} \qquad (Equation\ 10.6.6)$$

Equation 10.6.6 is showing Pythagoras' application to finding the total velocity squared, which would give, $\overline{v^2} = 3\overline{{v_x}^2}$,

$$P = \rho 3\overline{{v_x}^2} \qquad (Equation\ 10.6.7)$$

then this would simplify to $\frac{1}{3}\overline{\boldsymbol{v}^2}$ in Equation 10.6.7,

$$P = \rho \frac{1}{3}\overline{\boldsymbol{v}^2} \qquad (Equation\ 10.6.8)$$

where the $\overline{\boldsymbol{v}^2}$ term in Equation 10.6.8 now represents the velocity in the (x, y, z) direction (v_x, v_y, v_z).

Multiplying Equation 10.6.8 on both sides with volume, V, would then allow for the total mass Nm (mass of N particles), to be substituted via 'mass = density x volume', to get,

$$PV = Nm\frac{1}{3}\overline{\boldsymbol{v}^2} \qquad (Equation\ 10.7)$$

Factorising Equation 10.7 would make it easier to obtain an expression for the kinetic energy of a molecule,

$$PV = \frac{2}{3}N\left(\frac{1}{2}m\overline{\boldsymbol{v}^2}\right) \qquad (Equation\ 10.7.1)$$

Comparing Equation 10.7.1 with the ideal gas law 'PV = nRT' where n is the moles, R is the gas constant and T is the temperature, would allow the following equation to be expressed,

$$\frac{2}{3}N\left(\frac{1}{2}m\overline{\boldsymbol{v}^2}\right) = nRT \qquad (Equation\ 10.7.2)$$

$$\frac{1}{2}m\overline{\boldsymbol{v}^2} = \frac{3}{2}\frac{nRT}{N} \qquad (Equation\ 10.7.3)$$

As a reminder, n is the number of moles and N is the total number of particles. The Avogadro constant, N_A, can be substituted into the equation based on its definition (Equation 10.7.4) shown below,

$$N_A = \frac{N}{n} \qquad (Equation\ 10.7.4)$$

$$\frac{1}{2}m\overline{\boldsymbol{v}^2} = \frac{3}{2}\frac{RT}{N_A} \qquad (Equation\ 10.7.5)$$

Another substitution can be made to include the Boltzmann constant, k_B,

$$k_B = \frac{R}{N_A} \qquad (Equation\ 10.7.6)$$

$$\frac{1}{2}m\overline{\boldsymbol{v}^2} = \frac{3}{2}k_B T \qquad (Equation\ 11)$$

Equation 11 is the equipartition of energy and describes the average kinetic energy per degree of freedom.

$$T = \frac{1}{3}\frac{m\overline{\boldsymbol{v}^2}}{k_B} \qquad (Equation\ 11.1)$$

An adjustment of the kinetic energy term can be made to account for the degree of freedom,

$$KE = \frac{1}{2}m\overline{\boldsymbol{v}^2}N_f \qquad (Equation\ 11.2)$$

$$m\overline{\boldsymbol{v}^2} = \frac{2KE}{N_f} \qquad (Equation\ 11.2.1)$$

where KE is the kinetic energy and N_f is degree of freedom. Substituting Equation 11.2.1 into Equation 11.1 would give the temperature of the system, T,

$$T = \frac{2}{3}\frac{KE}{k_B N_f} \qquad (Equation\ 12)$$

The relationship between the temperature and kinetic energy has been shown. This means that the temperature can be controlled by multiplying the magnitude of each atom's velocity. This method of velocity scaling multiplies the magnitudes by a figure $\frac{\sqrt{T_B}}{\sqrt{T_{(t)}}}$ where T_B is the desired temperature and $T_{(t)}$ is the current temperature of the system[3] for a few timesteps at a time until the desired temperature is achieved. The Verlet integration algorithms presented above, provide the velocities used to obtain the instantaneous temperature of the system. In this current sub section, although momentum was included in the derivations, Equation 12 is under the assumption that the system has no net momentum.

3.3 Potentials

The force fields are the functions that govern the interactions of the system, to which parameters are assigned to formulate the correct forces. Aside from the application of Newton's laws, the force fields are arguably the most important aspect of molecular dynamics, in terms of acquiring accurate simulation results. When two atoms are in a close enough proximity, depending on how close the interatomic distance is, an interaction will occur to minimise any potential energy by either repelling or attracting. Pair potentials govern the interactions that form bonds between a pair of atoms. These potentials can then be multiplied and summated to produce the potential energy representing an entire lattice or the system.

One of the most common potentials used in molecular dynamics is the Lennard-Jones potential, where the interaction energy between two gaseous atoms, as a function of distance, is calculated. Another common example is the Buckingham potential, similar to

the Lennard-Jones potential, in which the term 'r^{12}' is replaced by an exponential parameter. This Buckingham potential was created to describe the short range interaction in ionic systems. Another similarity between the two potentials is that the Buckingham potential has terms for both an attractive and a repulsive component, a feature also seen in the Lennard-Jones potential. The Coulombic potential is a long-range potential, describing the electrostatic interaction between a pair of atoms. Both the Buckingham and the Coulombic potentials were used throughout this entire study.

3.3.1 Buckingham

The Buckingham potential[2] has terms describing both the attraction and repulsion between atoms,

$$U(r_{ij}) = A \exp\left(-\frac{r_{ij}}{\rho}\right) - \left(\frac{C}{{r_{ij}}^6}\right) \qquad (Equation\ 13)$$

where U is the potential energy describing the interaction between atoms 'i' and 'j' and r_{ij} is the interatomic distance between 'i' and 'j'. The symbols, A and ρ are potential parameters involved in describing the repulsive interaction, whereas C is the potential parameter used in the attractive term of the equation.

This potential is based on the Born model of the ionic solid, and as shown below, the Born model only includes the repulsive component of the Buckingham potential.

$$U(r_{ij}) = A \exp\left(-\frac{r_{ij}}{\rho}\right) \qquad (Equation\ 13.1)$$

The ceria models used in this study were obtained from Sayle et al.[4-6] and the generation process for these models is described further down below this chapter. The values for the Buckingham potential parameters were therefore, also sourced from Sayle et al.[4] and have been used in multiple studies[6-9]. It would be counter-productive to use new parameter values.

Atom i	**Atom j**	**A (eV)**	**ρ (Å)**	**C (eV. Å^6)**
Ce	O	1986.83	0.351	20.40
O	O	22764.30	0.149	27.96

Table 1: Table showing the values for the Buckingham potential parameters sourced from Sayle et al[4]. The authors sourced the values for the oxygen-oxygen interaction from Lewis and Catlow[10] and the cerium-oxygen interaction was derived by Sayle[11].

3.3.2 Coulombic

The Coulombic potential governs the electrostatic contribution to the interaction between the pair of ions,

$$U(r_{ij}) = \frac{q_i q_j}{4\pi\varepsilon_0 r_{ij}} \qquad (Equation\ 14)$$

where U is the potential describing the electrostatic interaction between ions 'i' and 'j', q_i and q_j are the charges of 'i' and 'j' respectively, ε_0 is the permittivity constant and r_{ij} is the

interatomic distance between ‘i’ and ‘j’.

The Coulombic interaction is generally representing attraction, as the ions involved are most often of opposite charge, but a repulsive electrostatic interaction could also be experienced if the ions are of the same charge.

Atom	Mass (amu)	Charge (e)
Ce	140.12	+4.0
O	16.00	-2.0

Table 2: Table showing the values for the mass and the charges of each atom used in the Coulombic potential.

3.3.3 Total Interaction Energy

The total energy configuration of a system in molecular dynamics can be generalised by,

$$U(r_1, r_2, \dots, r_N) = \sum Intramolecular\ bonds + \sum Intermolecular\ bonds + \sum Metal\ potential + \sum External\ field \quad (Equation\ 15)$$

where U is the total energy and (r_1, r_2, …, r_N) are the position vectors for a system of N atoms.

When the Coulombic interaction and the Buckingham potential is combined, the total energy of the interaction between the two atoms is given by,

$$U(r_{ij}) = \frac{q_i q_j}{4\pi\varepsilon_0 r_{ij}} + A\exp\left(-\frac{r_{ij}}{\rho}\right) - \left(\frac{C}{r^6}\right) \qquad (Equation\ 15.1)$$

The definition of the Coulombic interaction is less complex than the Buckingham interaction and the values needed to define the charges is a trivial matter, although the calculation of this interaction is computationally intensive. The Buckingham potential has parameters that are more difficult to define, such as *A*, ρ, *C*, and require the most attention in terms of getting accurate as possible values in order to obtain accurate simulations. The potential parameters can be calculated from quantum mechanical calculations or obtained experimentally from spectroscopic techniques. This means that one value obtained in literature may differ to a value obtained in another literature. The force fields used in molecular dynamics are a simplification of the true potential interaction and is simplified to reduce the computational cost. There is a compromise between being detailed enough to produce an accurate as possible pair interaction, but also a simple enough parameter so that the calculations are evaluated fast. Therefore, the potentials greatly affect the accuracy of the simulation results.

The total energy configuration can therefore be written as,

$$U(r_{ij}) = \sum_{ij} \frac{q_i q_j}{4\pi\varepsilon_0 r_{ij}} + \sum_{ij} A\exp\left(-\frac{r_{ij}}{\rho}\right) - \left(\frac{C}{r^6}\right) \qquad (Equation\ 15.2)$$

The conservation of the total energy is defined as,

$$E(r_{ij}) = \frac{1}{2}mv^2(r_{ij}) + U(r_{ij}) \qquad (Equation\ 15.3)$$

where E is the energy, m is the mass of the atom and v is the velocity. The first term on the right hand side is the kinetic energy component and the second term is the potential energy (Equation 15.2).

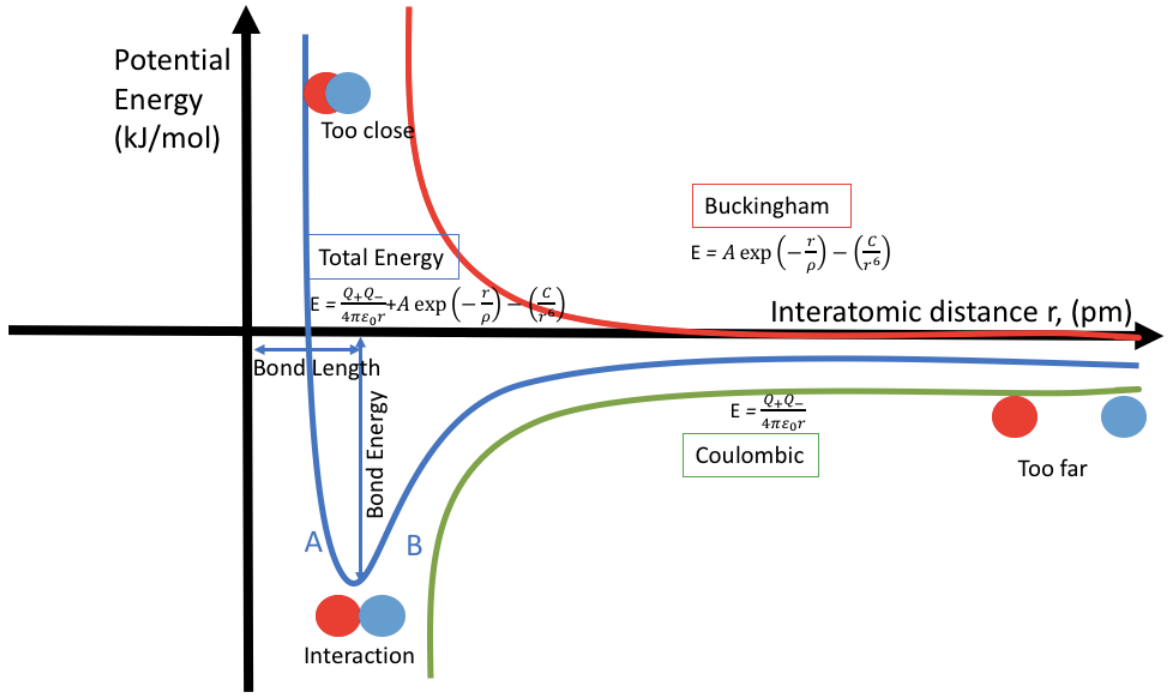

Figure 5: Figure showing the potential energy of a pair of atoms as a function of bond distance. The short-range interaction, Buckingham potential, is represented by the red line and the long-range interaction, Coulombic interaction, is represented by the green line. Both of these lines are drawn to show that the potential energy for these interactions eventually reaches zero, when the distance, r, reaches infinity. The figure is demonstrating the interatomic distance a pair needs to have, and consequently how much potential energy is produced, in order for an interaction to occur, leading to a successful bond formation. This total interaction energy is shown by the blue line. The point where attraction occurs is labelled as "A", whereas the point where repulsive forces are acting is labelled as "B". The point labelled "Too close" is where the attraction forces are dominant, and the point labelled "Too far" experiences repulsion as the dominant force.

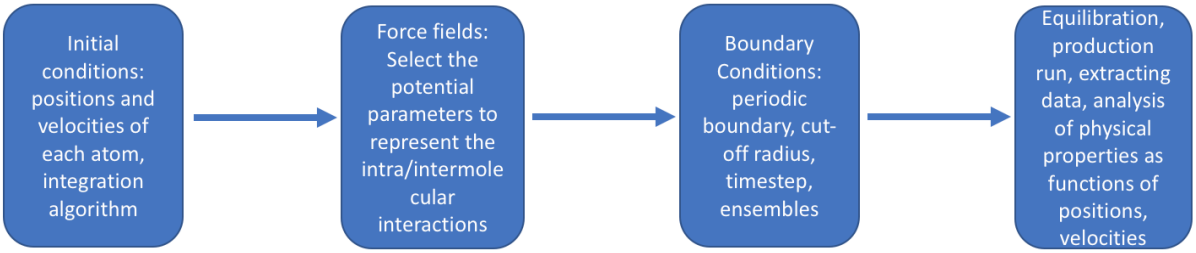

Figure 6: A basic outline of the molecular dynamics process summarised as a flowchart. The periodic boundary condition, cut-off radius, ensembles and equilibration mentioned in the flowchart are described in more detail in their own respective sub sections further down this chapter.

3.4 Simulation

3.4.1 Generating the Models

The ceria nanoparticle models used in this study were generated by Sayle et al.[5-6] and the nanocube was generated by caddeo[7]. The term 'polyhedron' can include the cubic shape and the nanorod used in this study, but in this report, the term nanocube will refer to the cubic ceria model, the term 'nanorod' will refer to the rod shaped ceria model and the term 'polyhedrals' will refer to the truncated octahedron ceria models.

All the ceria models were generated via the process of amorphisation and recrystallisation. This technique of simulating the synthesis has been used in multiple previous studies[5-7, 9, 12]. The procedure involved generating a model, simulating the amorphisation of the crystal model, simulating the recrystallisation of the structure and cooling to obtain the final, crystallised model. Therefore, each step in the synthetic process was conducted via molecular dynamics simulation. The NVT ensemble, which keeps a constant volume and temperature for a system of N particles, was implemented throughout the generation of all the ceria models to keep the temperature of the system constant. The polyhedral models had a majority of (111) facets and the (100) facets as the minority, whereas the nanocube had the (100) facet as the dominantly exposed plane and the (111) planes as the minority.

A cubic ceria model was generated comprising 1008 atoms (336 cerium atoms and 672 oxygen atoms). The simulation cell was large enough to ensure that only the interactions within the cell occurred, and not include interactions with the periodic images. The cubic model was amorphised for 50 ps at 3750 K. The process for obtaining the amorphous state involved adjusting the coordinates of all the ions in the lattice to incite an increase in the lattice parameter. The ions attempted to revert this increase in lattice parameter by moving towards the centre of the lattice. High tension was applied, which increased the mobility of the ions, causing them to collide and eventually an amorphous build was developed[12]. This amorphous precursor was then recrystallised for 4000 ps at 3750 K. The crystallisation process entailed the formation of two crystalline, nucleating seeds, which arose spontaneously from the random movement of the amorphous ions. The seeds formed on the surface of the model, both at opposite ends to each other, and gradually evolved over time to crystallise the entire structure. The joining of the two crystalline seeds led to the formation of grain boundaries. The (111) plane is the most thermodynamically stable plane, which drove the formation of this plane to be the preferentially exposed plane. The minority surfaces consisted of the (100) surface plane. During this stage, the formation of surface effects and microstructural features such as dislocations were developed naturally, without artificially editing the model[6]. The structure was then cooled to a temperature of 273 K.

The final, polyhedral ceria model adopted the cubic fluorite lattice, in which Ce^{4+} has 8 neighbouring O^{2-} situated at the corners, and an O^{2-} has 4 neighbouring Ce^{4+}. The most exposed plane was the most stable plane, the (111) surface. This surface plane had the largest surface area and the less stable (100) plane was the less exposed plane. The model containing 1008 atoms had a diameter of 2.7 nm. The following models, 1505 Ce, 4537 Ce and 6283 Ce[13], were generated using the same procedure but with the "starting" material comprising of 4515 atoms, 13611 atoms and 18849 atoms respectively. The 1505 Ce model gave a diameter of 4.5 nm, the 4537 Ce model gave a diameter of 6.7 nm and the 6283 Ce model had a diameter of 7.6 nm. The diameters of the models were measured using

Materials Studio[14].

The nanorod was generated using the same procedure but with a different "starting" ceria model as well as a different temperature and duration[5, 15]. Periodic boundary conditions were also used, but instead of aiming to keep the simulation cell large, the cell dimensions were reduced to allow for the interaction between neighbouring images to occur. This was to exploit the concept that the joining of the periodic images would lead to the formation of the "rod" structure and resultantly, the entire nanorod structure. A cluster of ceria comprising 15972 atoms (5324 cerium atoms and 10648 oxygen atoms) was amorphised for 1000 ps 8000 K and became molten. The molten structure fused with the model in a neighbouring image to form a section of the "rod". This action was repeated amongst the other neighbouring images to produce the entire structure. The nanorod was then recrystallised for 3827 ps at 3750 K and cooled to 10 K. The final nanorod structure had a hexagonal cross section, consisted of a near equal contribution of {111} and {100} facets to the surface and had a length of 9.6 nm.

The nanocube was generated[6-7] using a similar method but with a different "starting" ceria model and an additional annealing step. A cubic ceria model was generated comprising 20736 atoms (6912 cerium atoms and 13824 oxygen atoms). The model was amorphised for 50 ps at 8000 K. For the polyhedrals and the nanorod, the amorphisation process caused the model to reach a molten state without retaining any form of fixed lattice structure. The model used in the generation of the nanocube did not follow the same observation and instead, managed to retain the fixed cubic lattice fluorite structure as its core. This core was the cubic crystalline seed which drove the formation of the nanocube. The core contained 12000 atoms (4000 cerium atoms and 8000 oxygen atoms). This also meant that during the amorphisation process, the ions which amorphised were the ions surrounding the inner, cubic core. The model was then crystallised for 300 ps at 1500 K and annealed for 27 ns at 3750 K. The annealing process was to observe whether the cubic shape would be retained or whether a more thermodynamically stable form would evolve. The author observed that the cubic shape was retained throughout the entire structure, which indicated that as the model did not develop into a polyhedral (the energetically favourable shape), the cubic shape was stable. The preferentially exposed plane in the nanocube was the (100) surface. Additionally, these surfaces were on the faces of the nanocube and had a larger surface area compared to the (111) planes which were positioned at the truncated corners, and the (110) planes which were situated at the truncated edges. The author stated that if the {111} plane on the corners grew in size, then the morphology would have changed to a polyhedral. This was not observed and resultantly, the nanocube was in a stable form. The model was then cooled for 50 ps at 1K. The nanocube had a diameter of 8 nm.

The majority of the models used in this study were polyhedral shaped but a nanocube and a nanorod was also simulated. For the purposes of adopting a simple naming method, the polyhedrals are labelled as their cerium atom count, which is a third of the total atom count. For example, the smallest nanoparticle model simulated in this study contained 1008 atoms, but was given the name '336 Ce' as it contained 336 cerium atoms.

3.4.2 Equilibration

The nanoparticle models used in this study were taken from Sayle et al.[5-6, 13] and Caddeo[7], and have therefore, already been subjected to previous molecular dynamics simulations. This means that the models were equilibrated to the ensembles and conditions set by the previous simulation runs. Before any vibration simulations could be conducted in this study, an equilibration run was conducted to ensure that each model was brought to a configuration needed for the vibration runs. In other words, the equilibration procedure brings the model and the system to an equilibrated state, allowing the simulation of a vibration to occur at the desired conditions, which in this case, are attempting to represent the conditions of a nanoparticle at standard conditions (a pressure of 1 atm and a temperature of 298 K). This involved implementing a microcanonical NVE ensemble (constant volume and energy) and setting the temperature to 300K. A timestep of 0.005ps was used as this was only a preliminary stage and the data would not need to be analysed.

3.4.3 Vibration

Following the equilibration stage, vibrations were ready to be simulated. To induce nanoparticle vibration, energy was applied to the nanoparticle. This involved increasing the velocity of a (random) Ce^{4+} ion, producing the vibration through a single impact. A vibrational response induced by a single impact caused by one atom was favoured over using the method of increasing the velocity of multiple atoms at once. A single impact was used because a breathing mode is a resonant type of vibration. This means that the vibration is induced by an external force, which drives the nanoparticle to oscillate at specific frequencies but at greater amplitudes. To produce these vibrations at greater amplitudes, the external driving force does not have be large. This is due to the ability of the nanoparticle being able to store and transfer vibrational energy. In other words, a single impact was used to induce the simulated vibration because only a small driving force is needed to produce a breathing mode vibration.

In addition, studies in the literature review showed that the breathing modes all occurred at low frequencies. Increasing the velocity of multiple atoms would have a greater impact and may have induced a vibration of a slightly larger scale or cause the simulation to fail, the latter of which had actually occurred when more than one atom had an increase in velocity. Wheaton et al.[16] obtained two vibrational modes for single nanoparticles, the accordion mode and the breathing mode, which gave frequencies of 44 GHz and 68 GHz respectively. Both vibrational modes are of the same “bracket” of vibrations (acoustic) and the difference between the two modes are small.

This action may have been an unnecessary one as the results produced have shown to be an order of magnitude away from the expected range suggesting that these concerns of producing too high of a velocity were perhaps not needed.

The velocity of a single Ce^{4+} ion was increased by an order of magnitude. Varying velocities were tested on the same nanoparticle model in an attempt to observe whether the breathing frequencies differed. The units of length and time in the DL_POLY code is Å and ps respectively and resultantly, the velocity units are Å/ps. The velocities for all of the atoms, predetermined by the equilibration and previous simulation runs, were all within the range

of ~ $\pm$ 5 Å/ps. Multiple velocities were tested amongst the order of 100 Å/ps, (100 – 500 Å/ps), with the exception of the nanocube which was simulated at a velocity of 50 Å/ps.

The timestep used in the equilibration runs was 0.005 ps, but the timestep used in the vibration runs was adjusted to 0.00005 ps, in order to record more data points for the output files. The ensemble was set to NVT, with the temperature set to 300 K. The Ewald precision was set to 10^{-6}, and the equilibration was set to zero. There was also the option to adjust the 'print' value, which recorded the system data from the simulations, for every *n* timesteps as set by the print value. Another option, the 'traj' value, allowed for the customisation of the simulation images to be printed to the HISTORY file. The HISTORY file can then be viewed in the VMD visualiser, with the number of frames determined by a combination of variables such as 'traj' and timestep.

The calculated data of the atomic positions and velocities were outputted to the OUTPUT and STATIS files. The physical properties of the system (such as pressure) were then able to be analysed as a function of these calculated properties (positions, velocities). The pressure and timestep data was extracted to produce time-pressure graphs, which represented the frequency of the breathing mode vibration for that particular model. Frequencies were then calculated from these graphs.

The breathing mode vibration of the nanoparticle was recorded as fluctuations of the pressure. In particular, as all the atoms comprising the nanoparticle move ('breathe') outwards from the nanoparticle centre, the pressure reduces and becomes negative. Consequently, the attractive forces between the atoms start to counteract the kinetic energy, and the atoms decelerate until they reach zero velocity. The attractive forces then accelerate the atoms back to the centre increasing the pressure. The pressure is therefore a probe of the breathing mode as the system fluctuates about its (anharmonic) equilibrium, as shown in Figure 5. The breathing mode can be determined by observing the vibration using molecular graphics. However, the 'breathing' was subtle and the pressure fluctutations provided a more robust (and obvious) analytical tool.

The acceleration and outward velocity, in terms of calculating the pressure, is best described by revisiting the equation relating kinetic energy and pressure (Equation 16), the equation relating kinetic energy and the temperature (Equation 17) and the equation for finding the temperature of the system (Equation 18). Due to the presence of interatomic interactions, the expression for PV has the virial form (Equation 19),

$$PV = \frac{2}{3}N\left(\frac{1}{2}m\overline{\boldsymbol{v}^2}\right) \qquad (Equation\ 16)$$

$$\frac{1}{2}m\overline{\boldsymbol{v}^2} = \frac{3}{2}k_BT \qquad (Equation\ 17)$$

$$T = \frac{2}{3}\frac{KE}{k_BN} \qquad (Equation\ 18)$$

$$PV = Nk_BT + \frac{1}{3}S_{j>i}\,F_{ij}.r_{ij} \qquad (Equation\ 19)$$

where P is the pressure, V is the volume, N is the number of atoms of the system, m is the mass of the atom, v is the velocity, k_B is the Boltzmann constant, T is the temperature, KE is the kinetic energy (representing $\frac{1}{2}m\overline{v^2}$), F_{ij} is the interatomic force and r_{ij} is the interatomic distance. Equation 19 shows how Equation 16 can be rewritten to substitute in the temperature component of Equation 17, in other words, showing the relationship between calculating the temperature of the system and the pressure.

The consequence of these differing velocities caused an initial shock to the lattice, induced by the movement of the atom. This atom temporarily displaced itself from its original lattice position, creating a minor distortion to the surrounding structure, as shown in Figure 7.

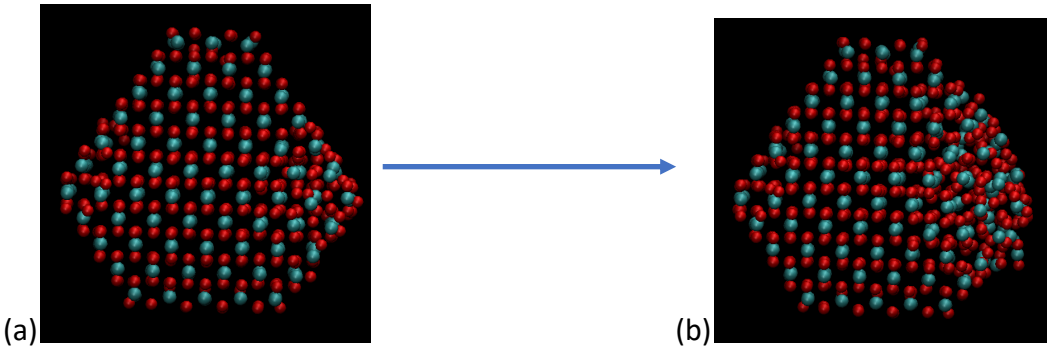

Figure 7: Images from the vibration simulation of the model 336 Ce (1008 atoms, 336 Ce atoms and 672 O atoms). (a) The vibration within the first 5 ps and (b) is the vibration after 10 ps. The displacement lasted a few ps before the atoms moved back to their original lattice sites.

It was predicted that the frequencies would decrease with increasing nanoparticle size. This assumption was based on the fact that a larger diameter, larger particle size and therefore, more atoms, would lead to the increase of the overall mass and cause the frequency to decrease. Polyhedral ceria models comprising of atom sizes from 1008 – 18849 atoms were tested at velocities ranging from 50 Å/ps – 500 Å/ps.

3.5 Simulation Code

DL_POLY[17] was the software code used in all of the molecular dynamics simulations, including the generation of the nanoparticle models and the velocity induced vibration simulations that followed.

3.5.1 Periodic Boundary Conditions

The simulations of every model in this study used periodic boundary conditions. The periodic boundary is a molecular dynamics construct which allows a small-scale model to behave as if it was of a larger size, allowing properties of a parent bulk material to be determined through the analysis of a smaller unit. In other words, these conditions allow for a smaller unit of a structure to be modelled, to which the smaller unit is representative of the entire structure. The central unit cell where all the interactions are calculated is termed the supercell[18] and the surrounding, infinite, repeat cells are termed as the periodic images, which are replicas of the supercell. This technique allows the parent bulk system or a larger molecular model to be represented by a smaller scaled model, as calculation of a bulk system is often restricted by computational limits.

The atoms within the supercell are the only ones considered in the calculations. If an atom from the supercell was to leave this cell through one of the cell "walls", the periodic boundary condition would cause a replica of the atom to enter through the opposite "wall". This image (replica) of the atom has the same properties as the atom that originally left the cell. The periodic images are therefore, exact copies of the supercell. Minimum image convention allows the interactions with some neighbouring repeat cells to be considered, but the interactions from the rest of the repeat cells are disregarded using a cut-off radius. This is described in further detail in the 'Cut-Off' sub section below.

For example, the nanorod model used in this study utilises the periodic boundary condition in such a way that represents the entire rod structure. A supercell represents a section of the nanorod, and the resultant periodic images can be viewed as forming the rest of the nanorod structure. Assuming the potential energy interactions within the supercell are the same throughout the entire structure, only the interactions in the supercell need to be calculated.

A single, polyhedral nanoparticle is not periodic and would not require a periodic boundary condition. A single nanoparticle would be able to fit within a single "box", and therefore, would not need a condition that represents a repetition of the supercell. However, the simulations in this study used an Ewald method of summation for calculating the Coulombic interaction and as a result, periodic boundary conditions were required.

3.5.2 Ewald Summation

An Ewald precision of 10^{-6} was used throughout these simulations and as with the rest of the parameters stated in this report, this value was chosen as it has been successfully used in previous studies, where the ceria models used in this report were involved.

In molecular dynamics, the Coulombic term describing the electrostatic interactions in an ionic solid is conditionally convergent. Depending on what parameter and what value is used, the result can be adjusted according to the order of the summation. The Coulombic interaction is slowly convergent, meaning that the contributions are calculated and summed together in a slow pace. Not using a parameter such as the Ewald sum would mean that the convergence of this interaction would stay a slow process, taking up computational time. Although, the use of an Ewald sum is still computationally expensive.

The Ewald sum treats the Coulombic interaction by separating this infinite long range interaction sum into two parts, a short range term and a long range term. The energy from each contribution has its finite sum rapidly converged in their respective spaces, where the short range contribution is calculated in real space and the long range contribution is calculated in the reciprocal space. The short range contribution is formed from the superposition of a Gaussian charge distribution of opposite charge to the charged ions of the system. This neutralises the ions of the system. The long range contribution is formed from adding a Gaussian cloud of the same charge as the original ions, to superpose the ions of the system. The ions of the system are therefore, no longer neutralised and their potential energies are calculated as a Fourier series[3]. These contributions are then combined and as such, the Ewald parameter treats the Coulombic interaction energy as two sums which leads to a rapid convergence. Using an Ewald summation reduces the time

taken for the electrostatic energies and forces to be calculated and is therefore, commonly applied to computational studies involving long-range interactions.

The Ewald sum can only be used in a three-dimensional periodic system. The long-range contribution is more complex and uses a calculation method where the formula for the Fourier sum includes a term to calculate the supercell, but also a term to calculate the infinite repeat cells (periodic images) created by the periodic boundary condition. In other words, using an Ewald parameter would assume the system is infinitely periodic.

$$U_{electrostatic} = \sum_{ij,R} \frac{q_i q_j}{|r_{ij} + R|} \qquad (Equation\ 20)$$

In Equation 20, $U_{electrostatic}$, is the potential energy, q_iq_j is the charge of the ions 'i' and 'j', r_{ij} is the position of the ions and R is the vector representing the periodic images. This equation shows that the formula for the Coulombic interaction is adjusted to account for the contribution of potential energy interactions from the periodic repeat images.

Resultantly, although a single nanoparticle would not need a periodic boundary condition, calculating the Coulombic interaction using an Ewald parameter would mean that a periodic boundary condition would need to be implemented, which is why these conditions have been used in this study. The Ewald summation allows for this converging process to occur more rapidly and resultantly, the order of summation determined by the Ewald value is a conditional parameter for the accuracy of the Coulombic interaction calculation.

3.5.3 Cut-Off

A cut-off value of 10.0 Å was used for both of the atom pairs (Ce-O, O-O) as this value has already been successfully implemented in previous simulations involving the nanoceria models used in this study[4, 7-8].

The use of a periodic boundary condition causes the potentials to calculate a sum for an infinite, periodic system. The potentials are defined in such a way that the interaction energies summed over the unit cells run over all the N number of particles within the periodic system and consequently, an infinite series is formed. The cut-off is the radius from which any interatomic potential summation past a specific distance is ignored. This means that any potential interaction beyond a specified limit is not computed. The cut-off stops the calculation of an infinite series and prevents an intensive computational cost from occurring.

$$U_{trunc}(r) = \begin{cases} U(r_{ij}), & r \leq R_{cut} \\ 0, & r > R_{cut} \end{cases} \qquad (Equation\ 21)$$

Equation 21 describes the modification of the potential energy interaction, where the truncation, U_{trunc}, is applied to restrict the energies that are calculated from atoms of position r, where the potential energies, $U(r_{ij})$, are considered if the positions are equal to or less than the cut-off radius, R_{cut}, and any atoms with positions further than the cut-off radius are disregarded.

According to Gonzalez[3], if L is the length of the supercell, the short range interaction

potentials are said to decay to negligible values at distances smaller than L/2. This makes short range interactions able to be subjected to a cut-off. Long range interactions decay slowly with distance, which means that their interaction energies, past the distance that short range interactions become negligible, should still be calculated. For this reason, short range interactions are subjected to a cut-off whilst the long range interactions are not usually subjected to the simple truncation scheme. In this study, the Buckingham potential energies were therefore truncated, whilst the Coulombic interactions were not.

Having a larger cut-off radius provides a more accurate result because more unit cells can have their interaction energies calculated and contribute to the overall result. However, as increasing a cut-off increases the number of atoms included in the calculation, the computational cost needed to account for this increase in unit cells is large. If R_{cut} represents the cut-off for a unit cell, increasing the cut-off radius would increase the number of unit cells included in the result, which scales to R_{cut}^3 because it is a three-dimensional vector so the scaling factor is cubic. For an N number of atoms, if we assume the simulation time to be roughly around the square of the number of atoms, denoted as N^2, the resulting computational time would be significantly increased if we also factor in the time taken to calculate the range increased by R_{cut}^3. There is a compromise between attaining an accurate result but also a computationally feasible time.

3.5.4 NVE, NVT Ensembles

For the integration algorithm calculations, an NVE ensemble was used. This meant that the number of particles, N, volume of the supercell, V, and the total system energy, E, was kept constant.

Depending on what ensemble is selected, multiple variables are able to be kept constant. For NVT, volume and temperature are the variables being kept fixed. This ensemble allows for temperature to be controlled by changing the velocities of the atoms, which changes the kinetic energies, and then changes the temperature of these atoms by applying a temperature factor to their velocities. This method of 'velocity scaling', involves applying a factor of $\frac{\sqrt{T_B}}{\sqrt{T_{(t)}}}$ where T_B is the desired temperature and T(t) is the current temperature of the system. The temperature factor is applied for a given timestep or once the temperature of the system has reached near the desired temperature. NVT is the default ensemble set by DLPOLY, but if the energy of the system and the temperature do not fluctuate excessively, velocity scaling can be applied using the NVE ensemble.

Other ensembles typically used include NPH (constant pressure and enthalpy), NPT (constant pressure and temperature) and NST (constant stress and temperature). Regardless of what ensemble is selected, the number of particles is always kept constant. Choosing the right ensemble allows for the simulations to imitate experimental conditions, keeping results as true as possible. For the equilibration, NVE was selected whereas NVT was chosen for the vibration runs.

3.6 Molecular Visualisation

3.6.1 VMD

Visual Molecular Dynamics[19] (VMD) is a 3D, visualisation software used to view graphical

models of molecules, nanoparticles and biological systems. This tool allows the advanced viewing of the molecular models for many purposes such as monitoring the progress of a simulation, or simply to analyse the visual properties of the molecules. It also contains various editing choices for rendering a molecule including; changing the colours of specific elements, editing the bond lengths, types of bonds and changing the viewing options in terms of being a perspective or an orthographic view. VMD also has the option for choosing from a wide variety of representation techniques of the molecules, two of which include viewing the model in the perspective of van der Waals' and also viewing the model using CPK, which is a mode showing atoms as spherical images and the bonds as cylinders.

In this particular study, VMD was used as a visualisation tool for observing whether the simulation was successful, or had crashed. It was also used to observe where the vibration source initiated from, and how the velocity changes affected the structural disorder. The viewing options selected to be represented were CPK, orthographic and sphere scales 5.0. These options were chosen as they seemed to present the models in a clear and easy manner for observing the atoms and their displacements, but also in a visually pleasing way. All the graphical representations of the models in the 'Results' section are screenshots taken from the VMD visualiser, unless stated as otherwise.

3.6.2 Materials Studio

Similar to VMD, Materials Studio[14] is a visualisation program, but can also be used to build, edit, view molecular structures and conduct simple simulation experiments. For the purposes of this study, the program was used to calculate the diameters of the nanoparticle models. It works by calculating the bond lengths between two atoms, and multiplies this with regards to the entire atom count.

3.7 References

1. R. Petrenko, J. Meller, Molecular Dynamics, 2010, In: Encyclopedia of Life Sciences (ELS), John Wiley & Sons, Ltd: Chichester, http://www.els.net DOI: 10.1002/9780470015902.a0003048

2. W. Smith, T. R. Forester, I. T. Todorov, The DL_POLY_2 User Manual, 2008, Version 2.19
3. M. A. Gonzalez, 2011, vol 12, pp. 169 – 200, DOI: 10.1051/sfn/201112009

4. T. X. T. Sayle, S. C. Parker, C. R. A. Catlow, 1994, Surface Science, 316(3), pp. 329 – 336

5. D. C. Sayle, X. Feng, Y. Ding, Z. L. Wang, T. X. T. Sayle, J. Am. Chem. Soc., 2007, vol 129, pp. 7924 – 7935

6. T. X. T. Sayle, F. Caddeo, X. Zhang, T. Sakthivel, S. Das, S. Seal, S. Ptasinska, D. C. Sayle, J. Am. Chem. Soc., 2016, vol 28, pp. 7287 – 7295

7. F. Caddeo, PhD thesis, University of Kent, 2016

8. S. Das, S. Singh, J. M. Dowding, S. Oommen, A. Kumar, T. X. T. Sayle, S. Saraf, C. R. Patra, N.E. Vlahakis, D. C. Sayle, W. T. Self, S. Seal, Biomaterials, 2012, vol 33, pp. 7746 – 7755

9. D. C. Sayle, S. A. Maicaneanu, G. Watson, J. Am. Chem. Soc., 2002, vol 124, pp. 11429 – 11439

10. G. V. Lewis and C. R. A. Catlow, J. Phys. C: Solid State Phys., 1985, vol 18, pp. 1149 – 1161

11. T. X. T. Sayle, PhD Thesis, University of Bath, 1993

12. T. X. T. Sayle, S. C. Parker, D. C. Sayle, Phys. Chem. Chem. Phys., 2005, vol 7, pp. 2936 – 2941

13. T. X. T. Sayle, S. C. Parker, D. C. Sayle, Chem. Commun., 2004, vol 21, pp. 2438 – 2439

14. Dassault Systèmes BIOVIA, Materials Studio Accelrys, Version 8.0, San Diego: Dassault Systèmes, 2017

15. T. X. T. Sayle, B. J. Inkson, A. Karakoti, A. Kumar, M. Molinari, G. Mobus, S. C. Parker, S. Seal, D. C. Sayle, Nanoscale, 2011, vol 3, pp. 1823 – 1837

16. S. Wheaton, R. M. Gelfand, R. Gordon, Nature Photonics, 2014, vol 9, pp. 68 – 72

17. W. Smith, T. R. Forester, DL_POLY_2.0, A general-purpose parallel molecular dynamics simulation package, J. Molec. Graphics, 1996, 14(3), pp. 136 – 141, Daresbury Laboratory, Daresbury, Warrington, UK

18. J. Li, Basic Molecular Dynamics. In: Yip S. (eds) Handbook of Materials Modelling. Springer, Dordrecht, 2005, DOI: 10.1007/978-1-4020-3286-8_29
19. W. Humphrey, A. Dalke, K. Schulten, “VMD – Visual Molecular Dynamics”, J. Molec. Graphics., 1996, vol 14, pp. 33 – 38

Chapter 4: Results

4.1 Calculating the Frequency

The first step was to count the number of peaks over a given timestep.

$$Frequency\ (ps^{-1}) = \frac{Number\ of\ peaks}{Timestep\ (ps)} \qquad (Equation\ 22)$$

The value is given in ps^{-1} so the answer was multiplied by (10^{12}) to give a value in s^{-1}.
The relation of frequency to wavelength is given as,

$$Frequency\ (s^{-1}) = \frac{Speed\ of\ light\ (ms^{-1})}{Wavelength\ (m)} \qquad (Equation\ 23)$$

$$v = \frac{c}{\lambda} \qquad (Equation\ 23.1)$$

This formula can be rearranged to find wavelength given as

$$\lambda = \frac{c}{v} \qquad (Equation\ 24)$$

Therefore,

$$\lambda = \frac{2.99792458\ x10^{8}}{v} \qquad (Equation\ 24.1)$$

$$m = \frac{ms^{-1}}{s^{-1}} \qquad (Equation\ 24.2)$$

This gives the wavelength in metres, m. The value was multiplied by (10^{2}) to give the wavelength in centimetres, cm. The wavenumber can therefore be found by,

$$\frac{1}{\lambda} = wavenumber\ (cm^{-1}) \qquad (Equation\ 25)$$

This was the method used to obtain all the wavenumbers recorded in Table 3 at the end of this chapter. For comparison purposes to literature data, the calculated frequencies in hertz were converted to wavenumbers as the majority of the experimental data are recorded in cm^{-1}. The frequencies were calculated by manually counting the peaks. Multiple counting procedures were conducted for each vibration simulation in an attempt to reduce human error. There is an uncertainty for each frequency which is given in each sub section and in Table 3.

4.2 336 Ce

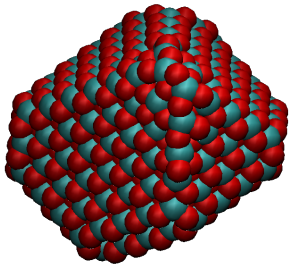

Figure 8: An image of the 336 Ce model obtained from the VMD[1] visualiser with a sphere scale point of 5.0. The sphere scale allows for the atoms to be adjusted larger or smaller for visualisation purposes. The higher the sphere scale, the larger the size of the atoms.

4.2.1 Equilibrate

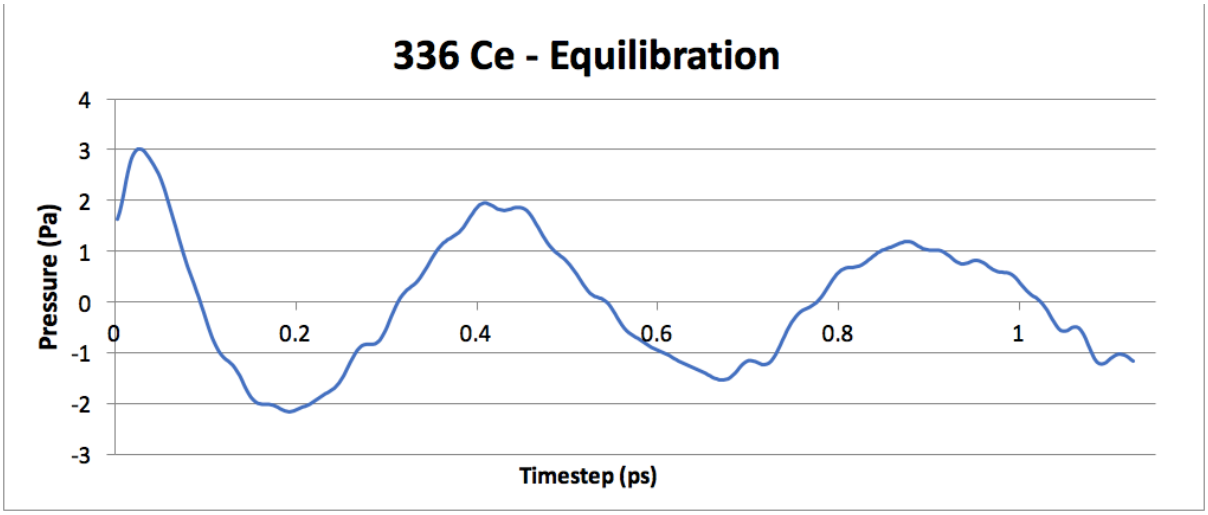

Figure 9: The time-pressure graph of the 336 Ce equilibration stage. An equilibration was able to be completed fast due to the size of the model (1008 atoms).

All of the nanostructure models were subjected to an equilibration simulation. The breathing mode did not occur in this stage and an observation of the pressure fluctuations was not needed. Resultantly, the frequencies of these equilibration stages were not calculated as they were only a preparatory phase. However, a time-pressure graph was still produced for each model as it provides a comparison on how the breathing motion differs from when the model is at equilibrium.

The velocities of the atoms in the model were within the range of +/- 5 Å/ps. The vibration in each model was produced by increasing the velocity of one atom by two orders of magnitude higher than the other atoms. Two orders of magnitude higher was chosen to ensure a great enough impact was simulated to produce a vibration sufficient enough to expand that specific surface. For the polyhedral nanoparticles, the velocity changes were coded onto a (111) plane in each model. In the time-pressure graphs that are presented in this chapter, the oscillation at the beginning of the graph is representing the vibration of the particular plane (111) from which the increase in velocity is occurring at. In the below example (Figure 10), the initial shock occurs from 0 – 1 ps, as indicated by the peak which is significantly larger than the rest.

It was predicted that a higher velocity would produce a greater vibration, causing a larger pressure fluctuation from the affected plane, which would be reflected in the pressure recordings in the time-pressure graph. The vibration originates from that particular plane and resultantly, the lattice in that region expands before any other region of the nanoparticle during the first moments of the vibration. The (111) plane is the most stable plane in a polyhedral ceria, so disrupting the surface by vibration, the atoms in that vicinity are displaced momentarily, leading to an increase in the surface energy. A higher surface energy would make the surface more reactive than before, which could lead to that particular region being a more catalytically active site.

4.2.2.0 100 Å/ps

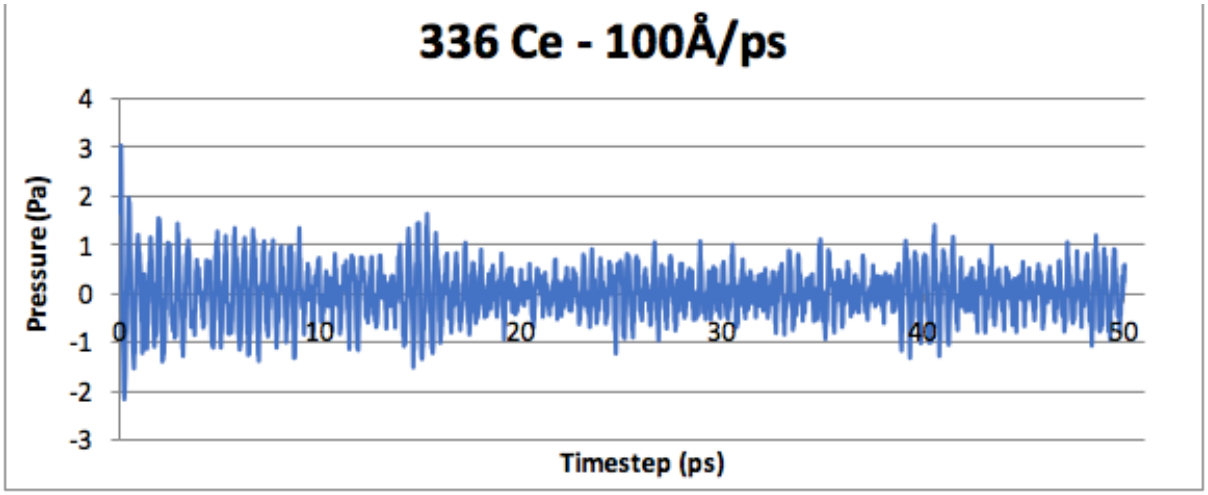

Figure 10: The time-pressure graph obtained for the 336 Ce – 100 Å/ps breathing frequency. The frequency calculated was 74.22 ± 2.17 cm^{-1}.

As shown in Figure 10, the initial shock of a single atom coded at 100 Å/ps caused the first oscillation of the breathing motion to reach a pressure fluctuation of ~ 3 Pa and a minimum of - 2.1 Pa. Around 15 – 17 ps, the pressure fluctuations increase in amplitude to ± 1.5 Pa, indicating the breathing motion is occurring at a greater effect than for the preceding time period of ~ 9 – 14 ps. From around 18 – 38 ps, the pressure fluctuations are steady and occur at the same amplitude around ± 1 Pa indicating the breathing motion is also occurring at a continuous amplitude. As the breathing motion is being detected from the pressure fluctuations, a high pressure reading would indicate the nanoparticle is experiencing the contraction part of the breathing motion and a low pressure reading indicates the expansion part. Therefore, the regions with the lowest pressure readings are indicating an expansion of the surfaces or the nanoparticle in general, increasing the surface energy and resultantly, increasing the reactivity of the surfaces. This makes these time intervals ideal for a catalytic reaction as it would lead to higher catalytic activity, or perhaps during a catalytic reaction, these time intervals are when higher catalytic activity occurs.

Visualiser – 336 Ce – 100 Å/ps

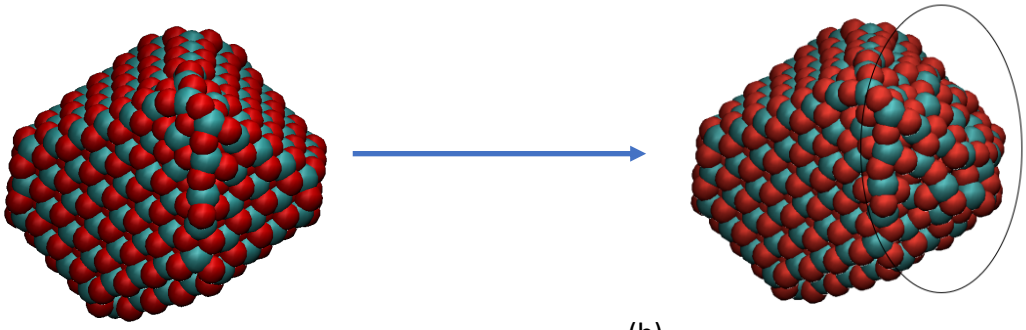

(a) (b)

Figure 11: Graphical representations of the 336 Ce – 100 Å/ps vibration taken from the VMD visualiser. (a) shows the nanoparticle at the beginning of the simulation, (b) shows the affected area and the source of the vibration.

In Figure 11, the effect of the velocity change is shown visually on one corner of the nanoparticle where there is a high degree of atomic disorder. This disorder is held momentarily before it returns to an equilibrative state. Initially, the affected atom causes only the immediate, local atoms to vibrate, which then causes further vibration to the surrounding atoms. Eventually, the vibration spreads throughout the entire structure.

4.2.2.1 200 Å/ps

Visualiser – 336 Ce – 200 Å/ps

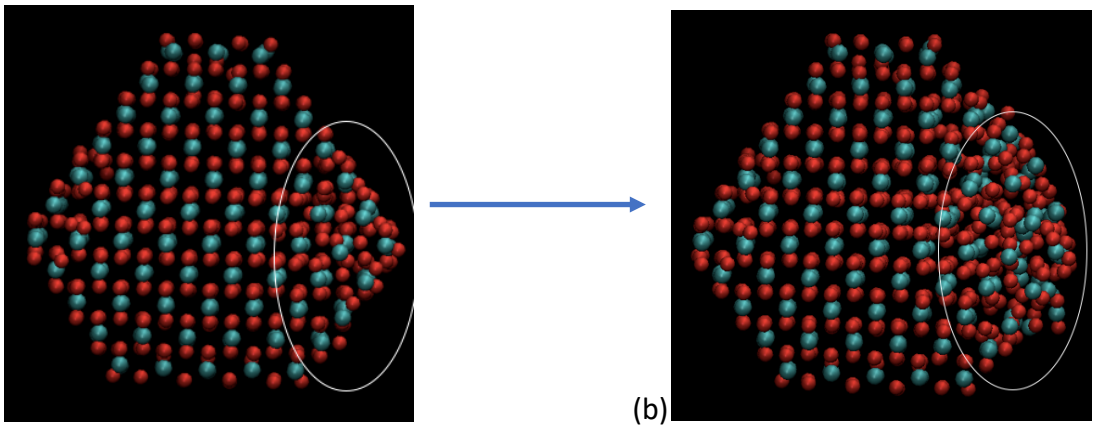

(a) (b)

Figure 12: The simulated vibration of 336 Ce – 200 Å/ps screenshots taken from VMD. (a) The location where the atom has a higher velocity is indicated by the white circle. The immediate, local atoms are already affected and have started to produce some disorder to the structure. (b) The disorder at its peak. Outside of the white circled area, the surrounding atoms are affected by the vibration as they have also become slightly displaced from their lattice points.

So far, the images of the models used in the simulations have been presented with a sphere scale of 5.0 for ease of visualisation. In Figure 12, the sphere scale is reduced to 2.0 in an attempt to show the disorder more clearly. The velocity change was coded onto the same co-ordinate as the one on 336 Ce – 100 Å/ps and as such, the disorder occurred in the same location. The most notable observation was that the disorder was slightly more aggressive than the run at 100 Å/ps. In conclusion, the higher the velocity (higher energy), the higher the degree of disorder.

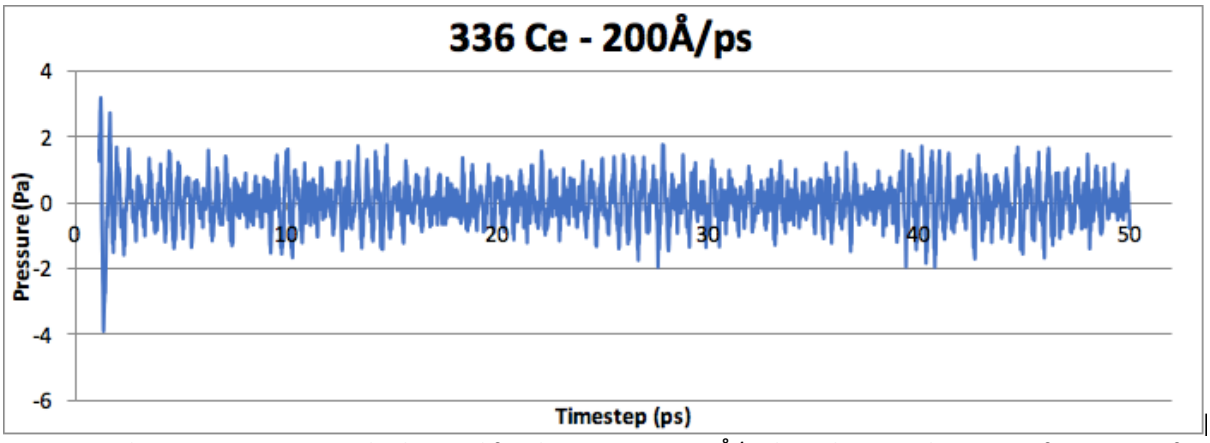

Figure 13: The time-pressure graph obtained for the 336 Ce – 200 Å/ps breathing mode giving a frequency of 71.82 $\pm$ 0.46 cm^{-1}.

In Figure 13, the majority of the smallest oscillations all have a maximum of up to 0.5 Pa with a minimum of up to - 0.5 Pa, in other words, the pressure fluctuations at these intervals have a $\pm$ 0.5 Pa range. These areas with the smallest oscillations include 7 – 9 ps, 11 – 13 ps, 16 – 18 ps, 31 – 33 ps, 35 – 39 ps and are where the lattice expansion is at its lowest. These time intervals are when the surfaces potentially have the lowest catalytic activity.

The time intervals where the greatest oscillations occur include 2 – 7 ps, 14 – 15 ps, 24 – 27 ps and 39 – 42 ps. There are also moments when an oscillation of great amplitude occurs but on a scale of 1 ps such as at 28 ps, 45 ps and 47 ps. The pressure fluctuations at these time intervals are an indication of when the reactivity of the surface is at its highest, and also, the duration that this increased reactivity is maintained.

The fluctuations in Figure 13 are very similar to 336 Ce 100 Å/ps (Figure 10), almost identical. The similarities are also reflected in their frequencies, 336 Ce – 100 Å/ps at ~ 2.225 THz and 336 Ce – 200 Å/ps at ~ 2.153 THz. The first two peaks are caused by the initial shock from the velocity impact, which have a maximum of around 3 Pa and a minimum of - 4 Pa. The breathing mode at 100 Å/ps (Figure 10) also had a first peak maximum of around 3 Pa and a minimum of around - 2 Pa. This comparison shows that an increase in the velocity leads to a slight increase in the amplitude of the vibration, as shown by the greater displacement in the first oscillation.

4.2.2.2 600K

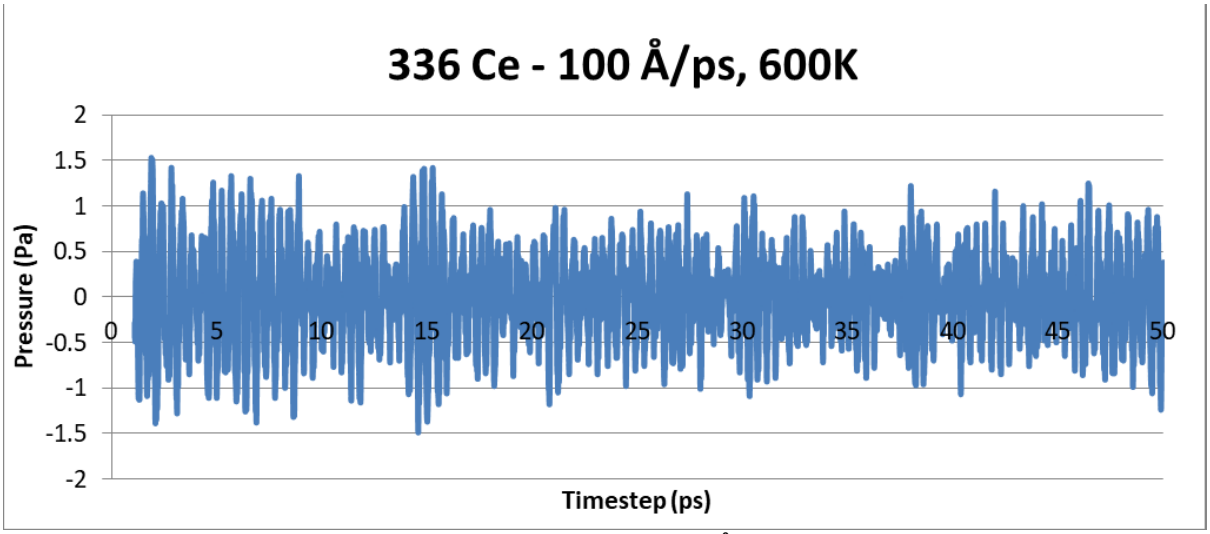

Figure 14: The time-pressure graph obtained for the 336 Ce – 100 Å/ps breathing vibration at a temperature of 600K. This was the first attempt at observing whether a higher temperature would have an impact on the frequency. The frequency was calculated to be 72.72 $\pm$ 0.67 cm^{-1}.

As a default setting, all the simulations were run at 300K. The exception was the 336 Ce simulation run at 600K. 336 Ce – 100 Å/ps (300K) had a frequency of ~ 2.225 THz (Figure 10), 336 Ce – 100Å/ps (600K) had a frequency of ~ 2.180 THz (Figure 14). From this observation, an increase in temperature causes a decrease in the frequency. This is unexpected as it was assumed that a temperature increase would increase the kinetic energy of the atoms, which would increase the thermal energy being supplied to the phonons. This was expected to cause a greater amplitude breathing motion to occur, as well as an increase in the frequency. The observation of a decrease in the frequency for a temperature increase, may be due to the system having been equilibrated to a temperature of 300 K, so perhaps conducting an equilibration at 600 K before the simulation of the breathing motion at 600 K would produce a different result.

Not enough data was acquired to make a certain assumption on whether temperature or velocity (acting as the source for the energy of the vibration) had the greater effect on the breathing motion frequency. Significant temperature increases such as an increase to 600K is unlikely to occur in an experiment or reproduced for a wanted effect so the effect of temperature was not investigated further.

4.3 1505 Ce

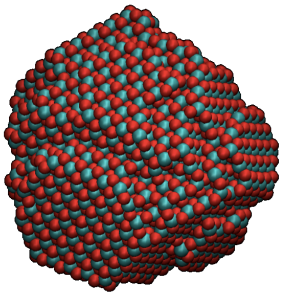

Figure 15: An atomistic model of the 1505 Ce model with 1505 cerium atoms and 4515 oxygen atoms.

4.3.1 Equilibrate

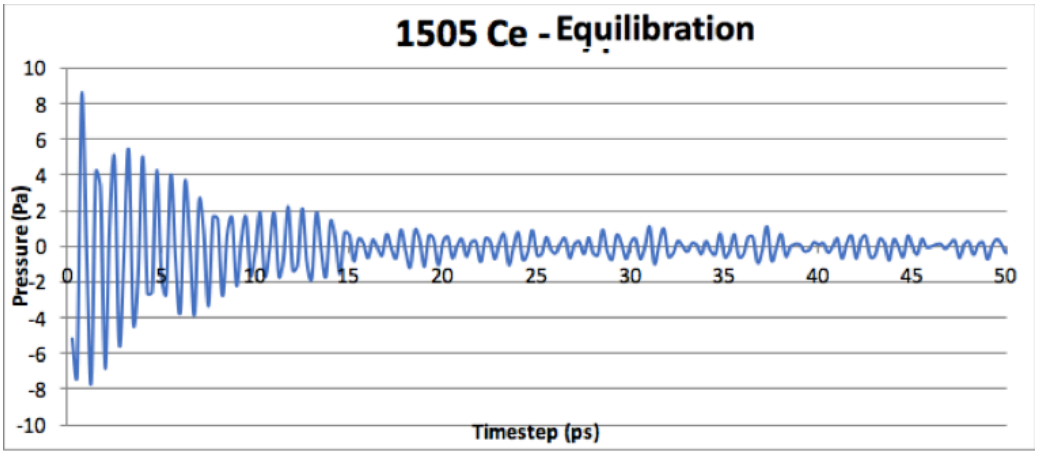

Figure 16: The time-pressure graph obtained for the equilibration stage of the 1505 Ce model.

As shown in Figure 16, the time taken for the 1505 Ce model to reach a state of equilibrium is around 15 ps. After 15 ps, the continuous, steady pressure fluctuations indicate that the nanoparticle is experiencing a zero point vibration. The 1505 Ce model took longer to reach a state of equilibrium compared to the 336 Ce model, which can be attributed to the size of the models in which 1505 Ce has over 4 times the amount of atoms the 336 Ce model has.

4.3.2.0 200 Å/ps

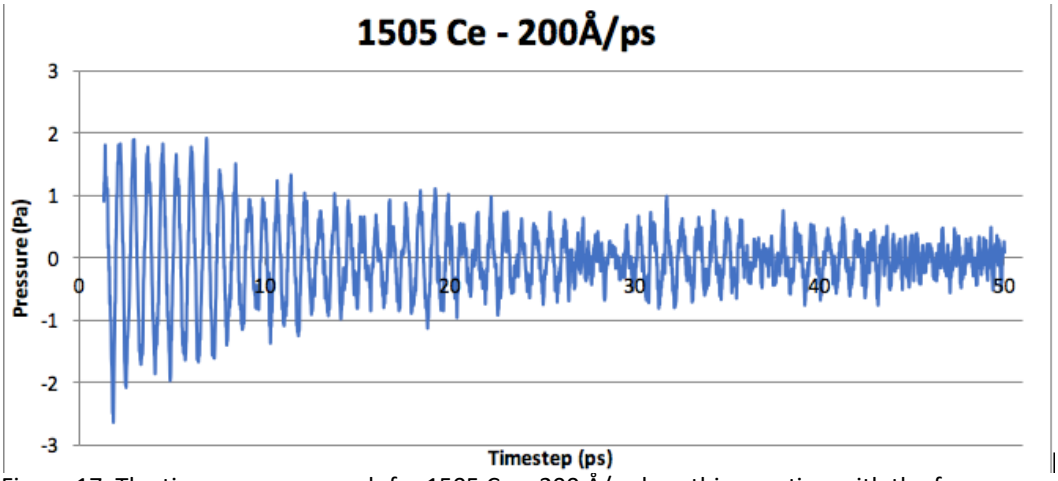

Figure 17: The time-pressure graph for 1505 Ce – 200 Å/ps breathing motion with the frequency given as 49.57 ± 1.17 cm^{-1}.

In Figure 17, the time period 2 – 8 ps is the breathing motion occurring at an enhanced amplitude, with a maximum contraction around 1.9 Pa and a maximum expansion at – 2.7 Pa, as a result of the increased velocity. In contrast to the breathing motions observed for the 336 Ce model, the oscillations at the start, affected by the impact of the velocity increase, occur for a longer duration. The time period of 2 – 14 ps is when the pressure readings are lower compared to the rest of the timesteps indicating the greatest surface expansion occurs at this interval and as such, the period of when catalytic activity is higher. The pressure fluctuations after 8 ps reduces ~ $\pm$ 0.5 Pa, but is still of a higher amplitude compared to the time periods around 27 – 30 ps and 40 – 50 ps.

Visualiser – 1505 Ce – 200 Å/ps

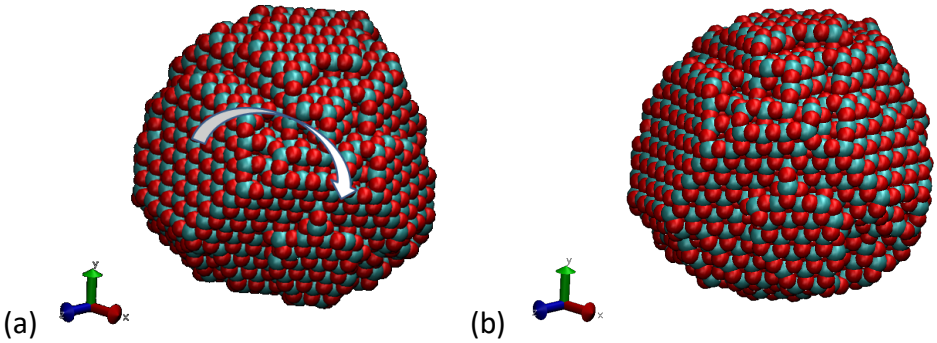

Figure 18: Screenshots obtained from the VMD visualiser of the rotational motion for the 1505 Ce breathing mode. The white arrow indicates the direction of rotational motion occurring. Translational motion also occurred at the same time but it was difficult to "capture" a visual of this without including an accompanying video clip of the movement. The axes are included to give a better perspective of the motion. (a) The nanoparticle at rest and (b) after rotational motion. This motion seemed to be independent of the changed velocities. Regardless of the nanoparticle size or whether the simulation was for an equilibration or vibration, the same rotational and translational motion occurred.

4.3.2.1 250 Å/ps

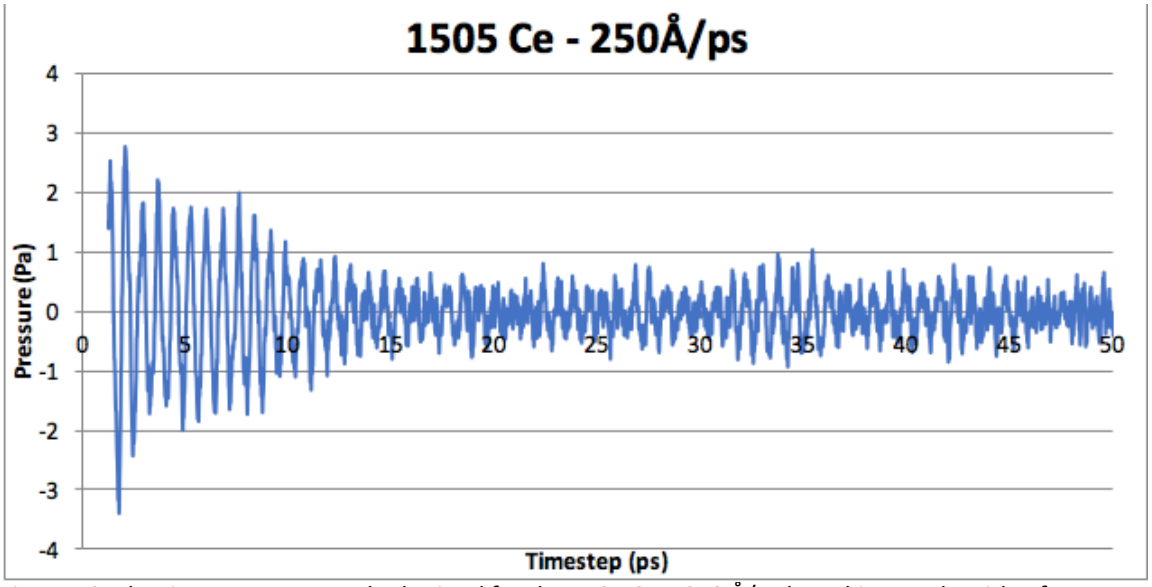

Figure 19: The time-pressure graph obtained for the 1505 Ce – 250 Å/ps breathing mode with a frequency of 45.36 $\pm$ 1.31 cm^{-1}.

In Figure 19, the pressure fluctuations are almost identical to the ones observed from 1505 Ce – 200 Å/ps (Figure 17). Compared to 1505 Ce - 200 Å/ps, the addition of 50 Å/ps to the velocity affected the highest and lowest pressure values by ~ ±1 Pa. The greatest amplitude of oscillation lasted from 2 - 10 ps, after which the amplitude immediately dropped to smaller amplitude oscillations. From around 32 ps, there is a sudden increase in the amplitude to ± 0.7 Pa, with a further amplitude increase at 36 ps to around 1.1 Pa, after which the amplitude drops back to around ± 0.5 Pa. Disregarding the oscillations from 0 – 13 ps, the oscillations at 32 – 36 ps are showing that the breathing motion is being experienced at a greater effect. The oscillation periods on either side of the 30 – 36 ps time range are at a lower amplitude and are examples of the periods in which the breathing motion is being experienced at its lowest effect.

4.3.2.2 300 Å/ps

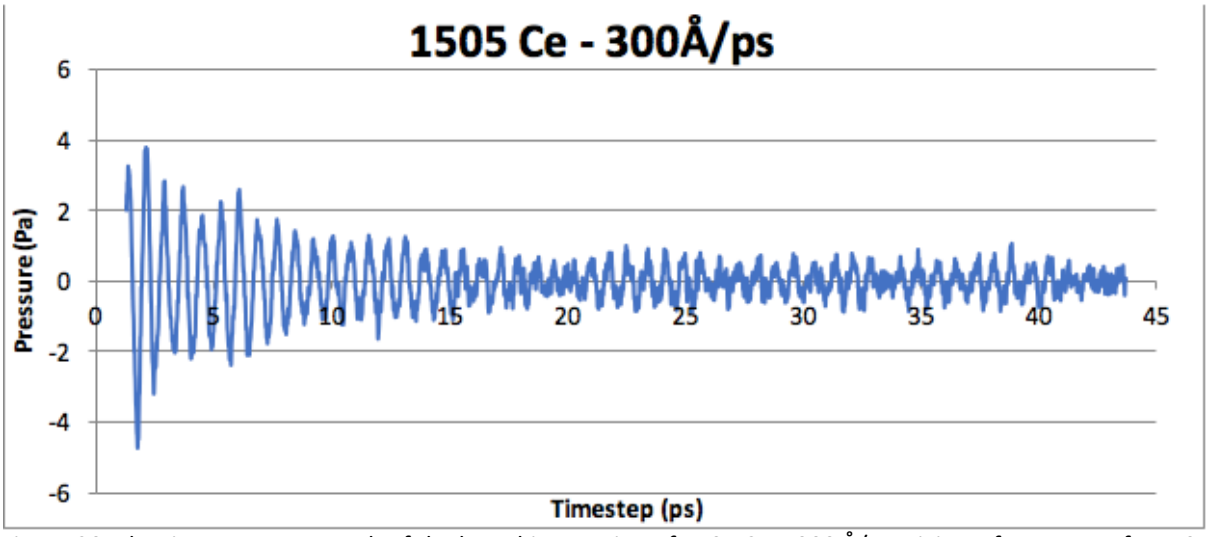

Figure 20: The time-pressure graph of the breathing motion of 1505 Ce – 300 Å/ps, giving a frequency of 44.13 ± 0.43 cm^{-1}.

As shown in Figure 20, the pressure fluctuations are similar to the ones produced for 1505 Ce – 250 Å/ps (Figure 19). The only difference is that the first few oscillations in the 1505 Ce – 300 Å/ps are of a slightly greater amplitude, with a maximum of 3.9 Pa and a minimum of – 4.8 Pa.

Visualiser – 1505 Ce – 300 Å/ps

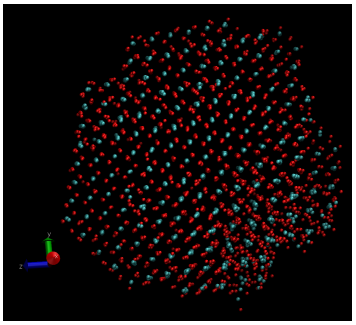

Figure 21: A visual image of the 1505 Ce model during the first few ps of the 300 Å/ps velocity induced vibration. A sphere scale of 1.0 was used to allow a better visualisation of the disorder.

4.3.2.3 400 Å/ps

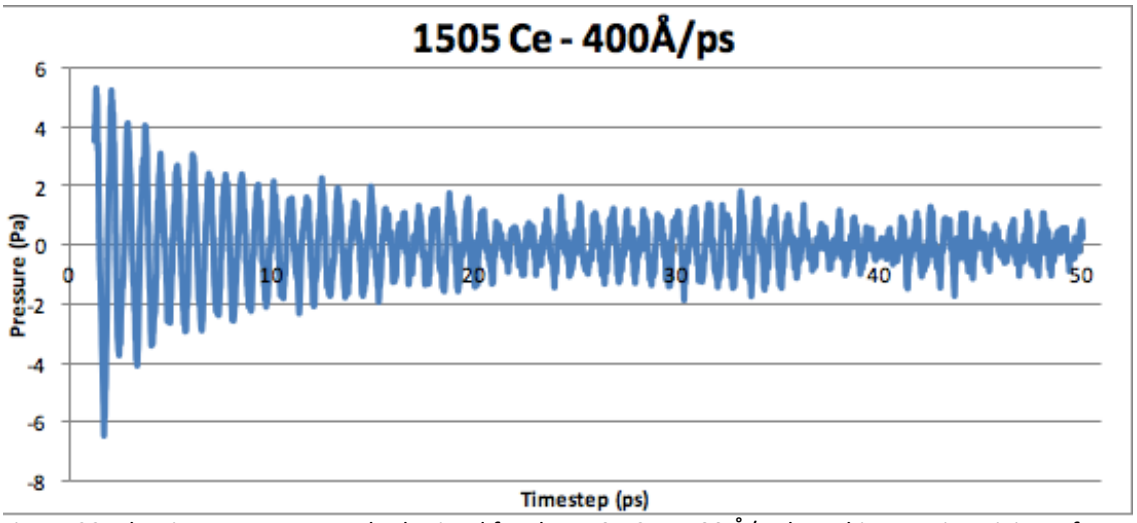

Figure 22: The time-pressure graph obtained for the 1505 Ce – 400 Å/ps breathing motion giving a frequency of 43.46 ± 0.36 cm^{-1}.

In Figure 22, the first oscillation occurs with a maximum of 5.5 Pa and a minimum of – 6.4 Pa. Compared to the previous velocities simulated for the 1505 Ce model (200 Å/ps, 250 Å/ps, 300 Å/ps), the vibration at 400 Å/ps produced a starting oscillation at the greatest amplitude. The oscillations from 2 – 20 ps are similar to the ones observed for the previous simulated velocities. The general observation from the range of velocities tested is that, with an increase in velocity (energy), the amplitude of the starting oscillations also increase.

4.3.2.4 200 Å/ps – y co-ordinate

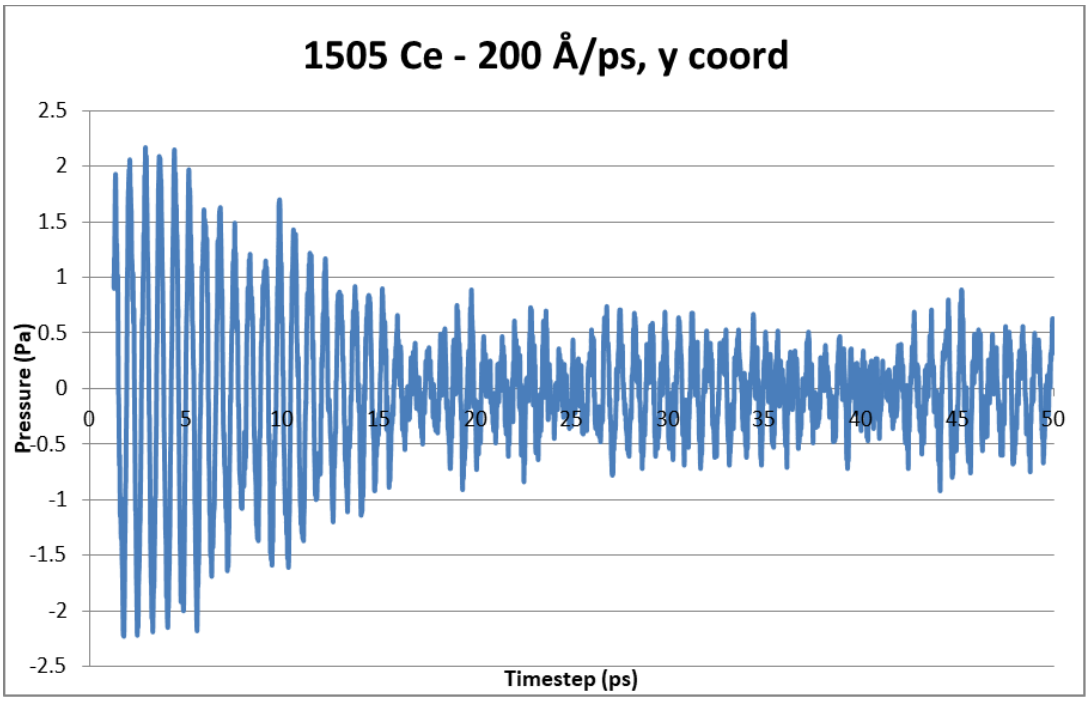

Figure 23: The time-pressure graph obtained for the breathing motion of 1505 Ce, induced by a velocity of 200 Å/ps coded onto the y co-ordinate instead of the default x co-ordinate position, giving a frequency of 45.40 ± 0.48 cm^{-1}.

As a default, all the velocity changes were coded onto the x co-ordinate. However, three simulations were tested with velocity changes on the y co-ordinate to observe any possible

effects; 1505 Ce – 200 Å/ps – y coord, 1505 Ce – 250 Å/ps – y coord, 1505 Ce – 300 Å/ps – y coord. It was predicted that changing the velocity onto a y co-ordinate would not have a significant affect as it was assumed that the breathing motion is isotropic. This is based on a previous study[2] where the strain applied on a nanosphere, inducing a breathing motion, was observed to be isotropic.

In Figure 23, the graph shows that changing the velocity on the y co-ordinate instead of the x co-ordinate decreased the frequency by ~ 0.125 THz ie (200 Å/ps – *x coord* at ~1.486 THz and 200 Å/ps – *y coord* at ~ 1.361 THz). There is a frequency difference which does not indicate the breathing motion to be an isotropic property, but the frequency difference is not significantly great enough to conclude that anisotropic behaviour has been observed. Aside from the ~ 0.125 THz difference in frequency, the vibrational graphs were very similar and there does not seem to be any major change from coding the velocity (impact of vibration) onto the y co-ordinate.

4.3.2.5 250 Å/ps – y co-ordinate

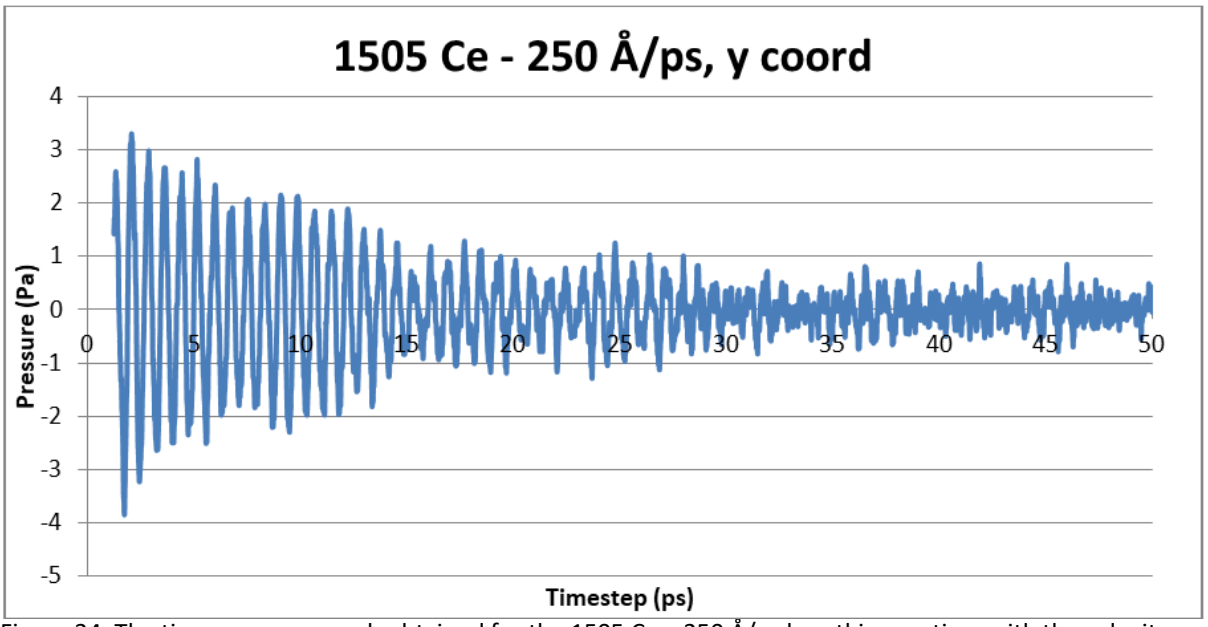

Figure 24: The time-pressure graph obtained for the 1505 Ce – 250 Å/ps breathing motion, with the velocity increase coded onto the y co-ordinate and the frequency given to be 44.83 $\pm$ 1.04 cm^{-1}.

Similar to the comparison between 1505 Ce – 200 Å/ps coded onto the x co-ordinate and 1505 Ce – 200 Å/ps coded onto the y co-ordinate, in which the frequency decreased when coded onto the y co-ordinate, the same observation occurs for the 1505 Ce – 250 Å/ps, y co-ordinate (Figure 24). The frequency obtained in Figure 24 is ~ 1.344 THz, whereas the frequency obtained for the same velocity but coded onto the x co-ordinate (Figure 19) is ~ 1.360 THz. This shows that coding the velocity change onto a y co-ordinate slightly decreases the frequency. However, when comparing the amplitudes of the starting oscillations in Figure 24 occurring from 2 – 14 ps, the breathing motion occurs at a greater amplitude than for the ones observed in Figure 19. The rest of the pressure fluctuations are similar to the ones observed in Figure 19. Overall, the breathing frequencies for the 1505 Ce simulations are around 1 THz lower than for the 336 Ce simulations.

4.4 4537 Ce

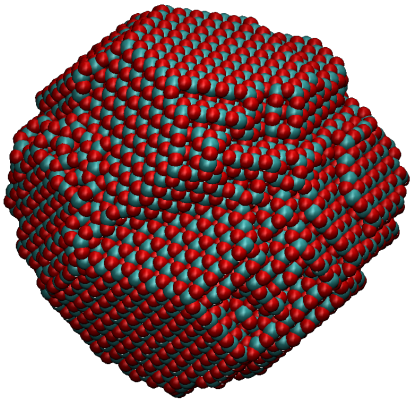

Figure 25: An atomistic model of the 4537 Ce nanoparticle comprising 4537 cerium atoms and 13611 oxygen atoms, viewed using VMD.

4.4.1 Equilibrate

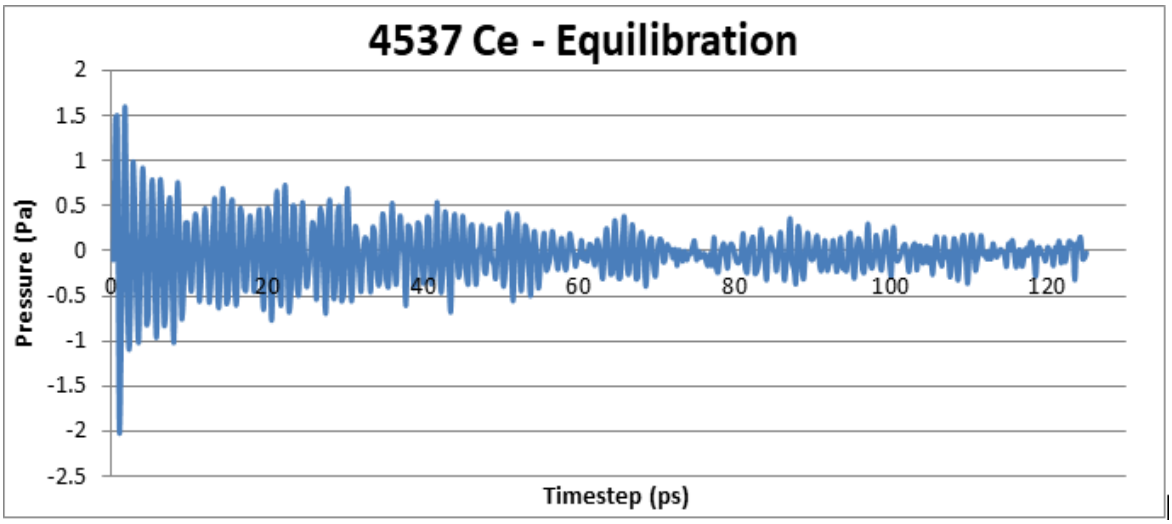

Figure 26: The time-pressure graph obtained for the equilibration of the 4537 Ce model.

In Figure 26, the time taken to equilibrate the model was over 120 ps, which is over double the time taken to equilibrate the 1505 Ce model. 1505 Ce reached equilibrium around 16 ps but 4537 Ce maintained a steady equilibrium from around 70 ps. A suggestion for the major time difference between the two nanoparticles is most likely due to the size difference, 4537 Ce is three times the size of 1505 Ce and as such, more atoms to equilibrate. Another observation made was that the pressure scale started with a maximum and minimum of around 1.5 Pa and -2.1 Pa, as opposed to the pressure scale maximum and minimum of 1505 Ce, which had values around 9 Pa and -7 Pa. Once equilibrium was reached, the pressure scale for 4537 Ce reached ~ ± 0.5 Pa, similar to 1505 Ce.

4.4.2.0 100 Å/ps

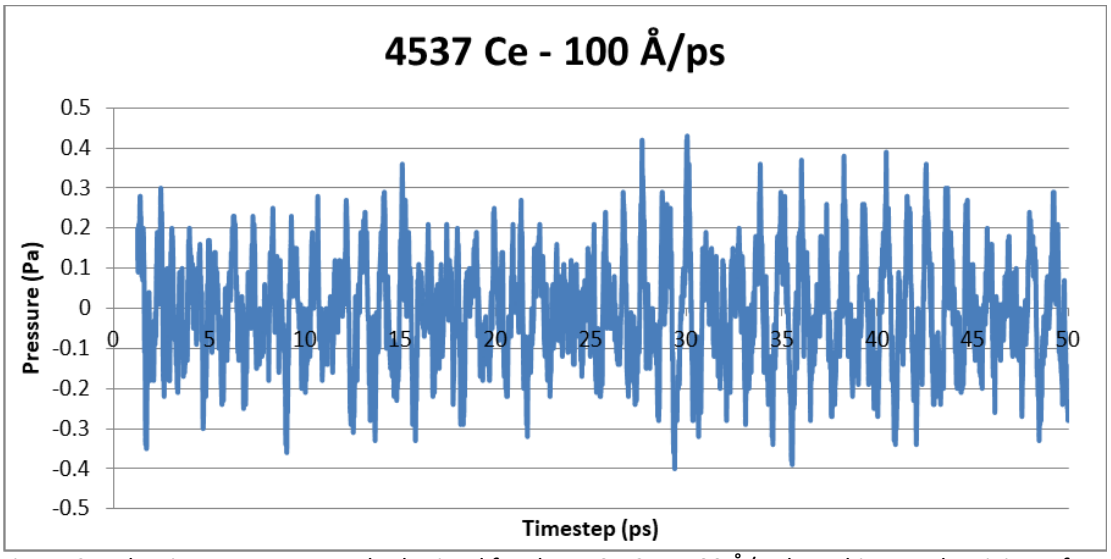

Figure 27: The time-pressure graph obtained for the 4537 Ce – 100 Å/ps breathing mode, giving a frequency of 36.59 ± 0.47 cm^{-1}.

In Figure 27, the highest levels of amplitude (breathing motion occurring at its greatest effect) occur around 27 – 30 ps where the maximum contraction is at 0.43 Pa and the maximum expansion is at – 0.41 Pa. At 34 – 45 ps, the breathing oscillations are also occurring at a higher amplitude with an average contraction measuring as 0.39 Pa and average expansions measuring as – 0.34 Pa. One of the most notable observations from Figure 27 is that the pressure scale has dramatically reduced compared to the previous, smaller sized nanoparticles. In other words, the amplitude is significantly smaller for a larger nanoparticle. There does not seem to be the same type of pressure fluctuations as the previous simulations. To elaborate, the previous models (Figure 10, Figure 17) experienced an initial shock from the velocity change, briefly causing a breathing motion to occur at an enhanced amplitude during the starting oscillations (~ 2 – 10 ps). Contrastingly for the 4537 Ce model, the oscillations near the start (2 – 10 ps) do not have as great of an enhanced amplitude. This may be due to the velocity inducing the vibration being of a small value relative to the model. In other words, the scale of impact for a velocity of 100 Å/ps on an atomistic model of 13611 atoms is not as great as applying the same velocity to a model of 1008 atoms. Perhaps applying a velocity of 500 Å/ps may have produced a similar effect of the starting oscillations occurring at an enhanced amplitude.

Another notable observation is that the breathing frequency produced for 4537 Ce is lower than the frequencies obtained for the smaller models, which fits the expected trend of increasing diameter producing a lower frequency.

4.5 6283 Ce

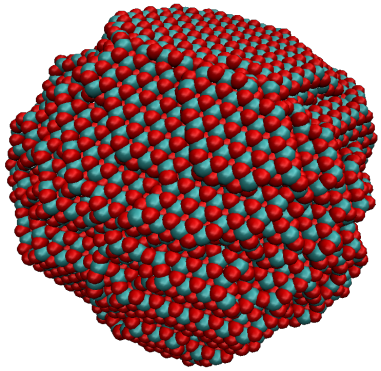

Figure 28: An atomistic model of the 6283 Ce model comprising 6283 cerium atoms and 18849 oxygen atoms, viewed using VMD.

4.5.1 Equilibrate

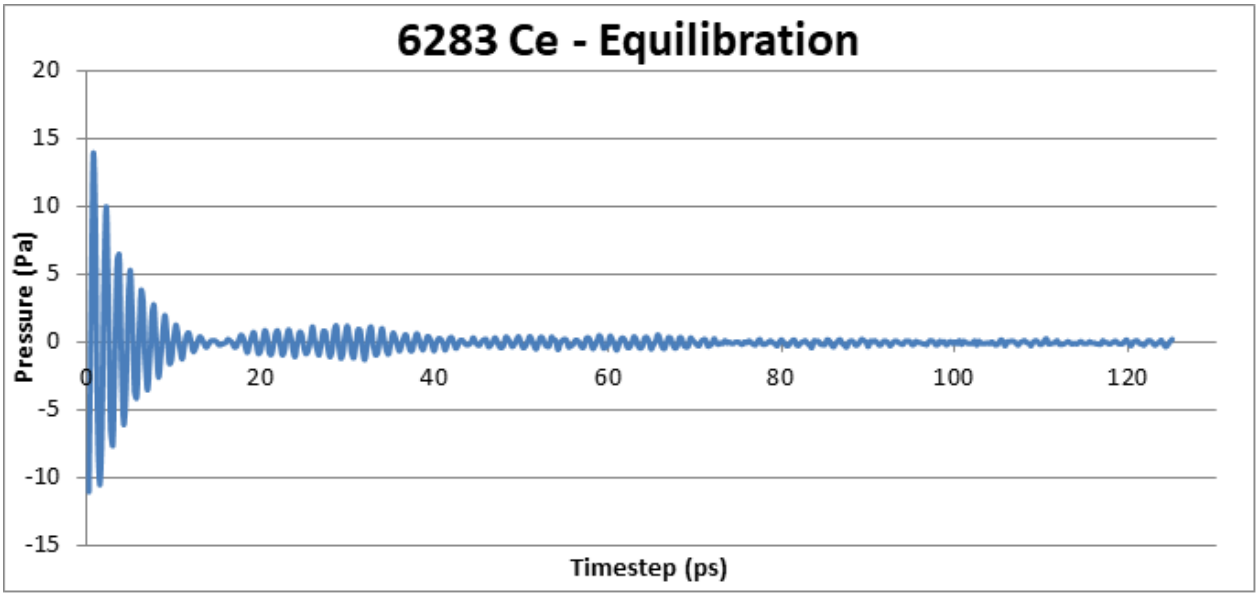

Figure 29: The time-pressure graph obtained for the 6283 Ce – Equilibration simulation.

The equilibration graph for 6283 Ce (Figure 29) seemed to have more similarities with the equilibration for 1505 Ce (Figure 16) rather than with 4537 Ce (Figure 26), which is surprising as 6283 Ce and 4537 Ce are closer in terms of size. For example, 6283 Ce has a maximum and minimum pressure of around 14 Pa and – 11 Pa, which is closer to the values for 1505 Ce (9 Pa, - 7 Pa) than for 4537 Ce (~ 1.5Pa, ~ - 2.1 Pa). As with the equilibration time-pressure graphs produced for the smaller sized polyhedrals, the pressure fluctuations are smooth and there are not irregularities.

4.5.2.0 100 Å/ps

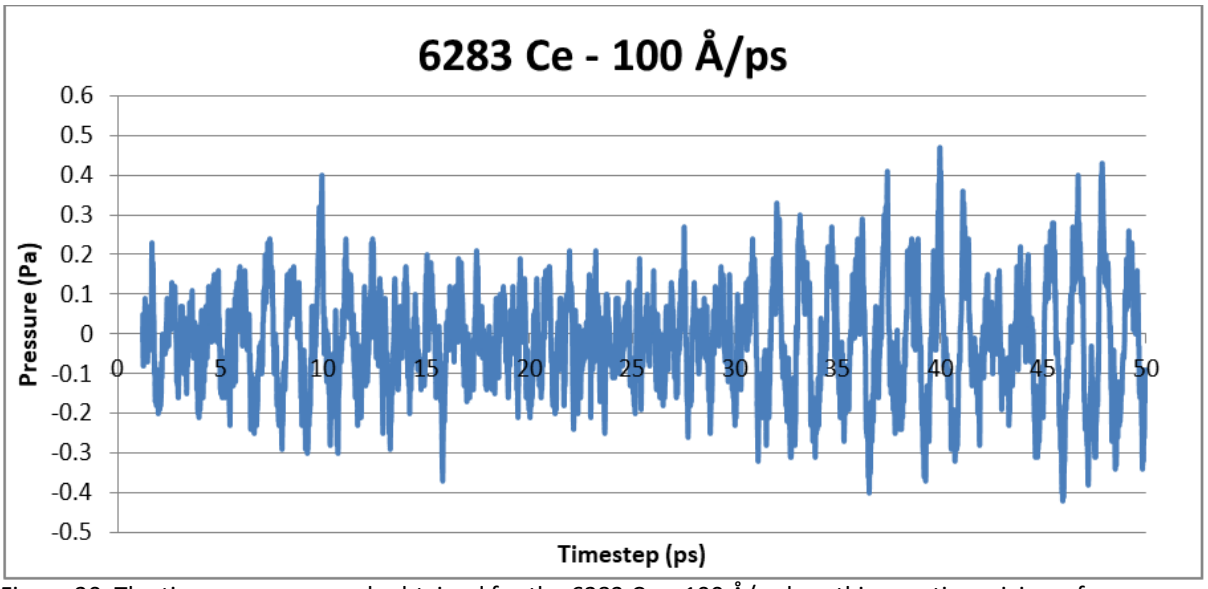

Figure 30: The time-pressure graph obtained for the 6283 Ce – 100 Å/ps breathing motion, giving a frequency of 34.76 ± 1.17 cm^{-1}.

The breathing frequency for the 6283 Ce model (Figure 30) is given as 1.042 THz. Similarly to the time-pressure graph for the breathing motion of 4537 Ce (Figure 27), the starting oscillations are not occurring at a significantly enhanced amplitude, unlike the observations for the 336 Ce and 1505 Ce models. Instead, the pressure fluctuations in the 6283 Ce model grow in amplitude as time progresses. This observation was not predicted as it was assumed that the velocity impact would produce the breathing oscillations at its greatest amplitude, which would eventually reduce in amplitude as time progressed, as observed for the 336 Ce and 1505 Ce models.

In line with the general trend observed so far, the 6283 Ce breathing frequency is lower than the smaller sized nanoparticles, further confirming that the frequency decreases as the size (diameter) increases.

4.6 Nanocube

4.6.1 Equilibrate

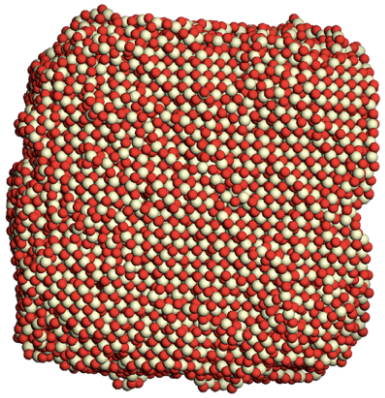

Figure 31: An atomistic model of the ceria nanocube of 20736 atoms comprising 6912 cerium atoms and 18849 oxygen atoms, viewed using Materials Studio[3]. The previous nanoparticle models in this report have been

screenshotted from VMD but the image of the nanocube was taken from Materials Studios. The way the nanocube was coded meant that in VMD, the image of the nanocube was not a complete square structure due to the periodic boundary conditions. Instead, only the "corners" of the nanocube would be shown, with a hollow core. Materials Studio allowed the editing of the file to convert the "corners" into a conventional cubic shape visually by repeating the unit cells.

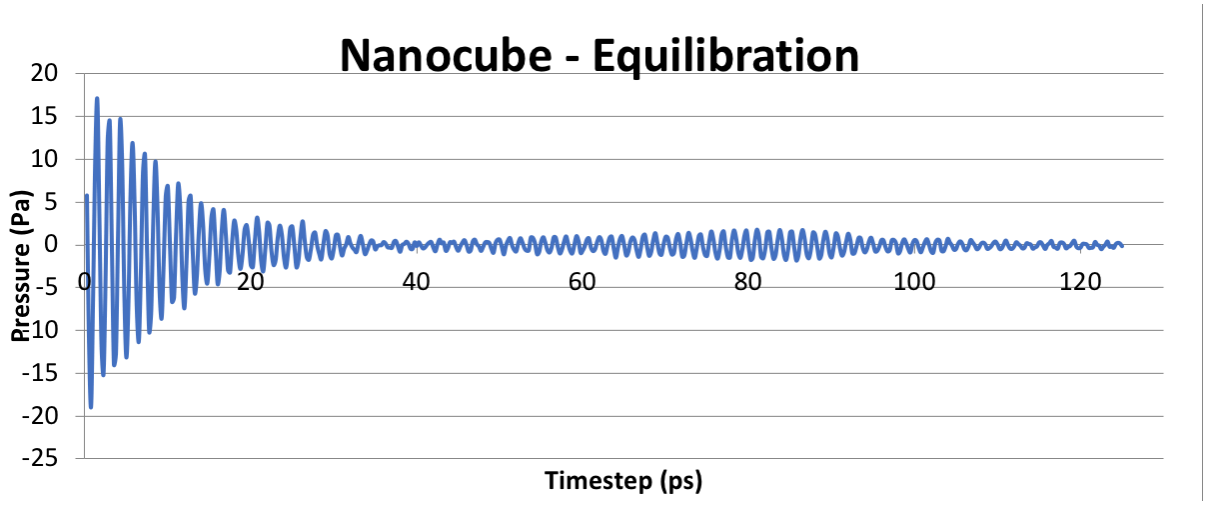

Figure 32: The time-pressure graph obtained for the equilibration of the nanocube.

Figure 32 shows that the nanocube equilibration is similar to the pressure fluctuations produced for the 6283 Ce equilibration(Figure 6283), except that the nanocube experiences a greater amplitude of pressure fluctuation towards the beginning of the timesteps. The time taken to equilibrate the nanocube is around 37 ps whereas 6283 Ce takes around 17 ps to reach equilibrium. As with the previous models, the oscillations are smooth and show no sign of abruptness.

4.6.2.0 50 Å/ps

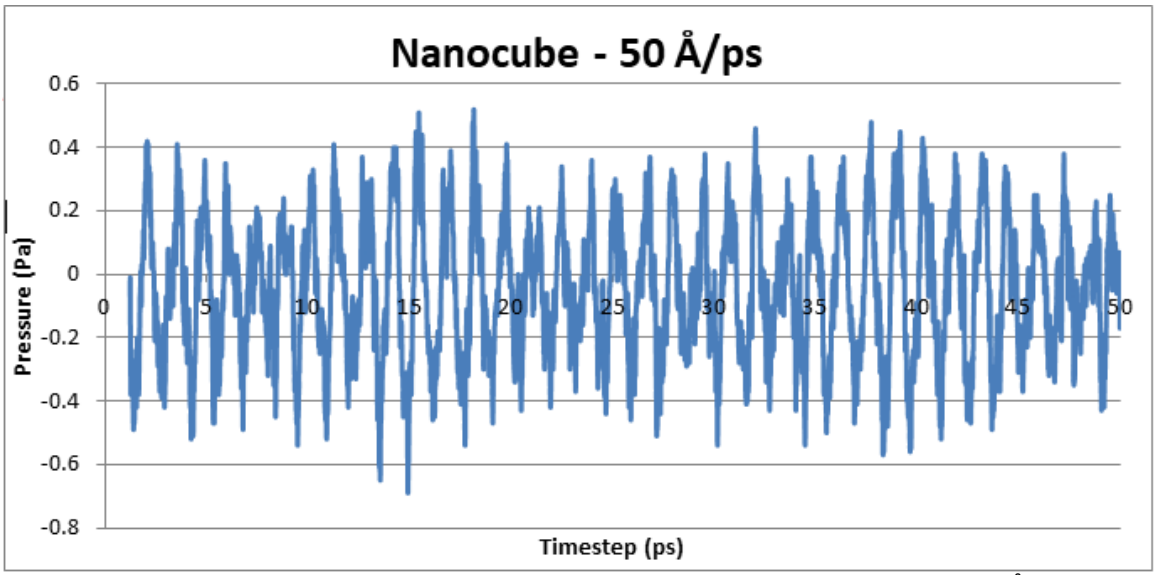

Figure 33: The time-pressure graph obtained for the breathing motion of the nanocube at 50 Å/ps. The frequency was calculated to be 26.65 $\pm$ 0.47 cm^{-1}.

The nanocube comprised of 20736 atoms (6912 cerium atoms) and produced a frequency of ~ 0.799 THz (Figure 33). The 6283 Ce model had a similar amount of atoms (18849 atoms)

and produced a frequency of ~ 1.042 THz (Figure 30). The nanocube has more atoms than the 6283 Ce model and as a result, the nanocube follows the general trend found that the frequency decreases for a nanoparticle of increasing size. The velocity used to obtain the frequency for the nanocube was half the velocity used for the 6283 Ce model. A velocity of 50 Å/ps was used for the nanocube because any velocity of a magnitude higher caused the simulation to crash. This was suggested to have been caused by the surface having a high reactivity. The preferentially exposed plane on the nanocube is the highly reactive (100) surface plane, but the truncated corners and edges are of the (111) and the (110) plane respectively. The velocity induced vibration was coded onto one of the (100) surface planes, the most reactive out of all the planes on the nanocube. Considering that the velocity increase is meant to represent the energy inducing the breathing motion, this implies that not a lot of energy is required to produce a breathing mode in this particular nanocube. The maximum pressure reading represents the contraction at its greatest effect, which was recorded as 0.5 Pa and the average contractions were recorded around 0.2 – 0.39 Pa. For the expansion part of the breathing motion, the largest expansions were around – 0.7 Pa and the average expansions were around – 0.5 Pa. Compared to the near spherical polyhedrals, the nanocube breathing motions occurred at lower amplitudes. For example, the 336 Ce model had breathing motion contractions at 3 Pa and expansions at – 2.1 Pa, whereas the nanocube had contractions at 0.5 Pa and expansions at – 0.7 Pa.

The computational time used to process the breathing motion for the nanocube exceeded the expected timeframe. As this model was the only nanostructure of a cube shape, the nanocube was not explored further.

4.7 Nanorod

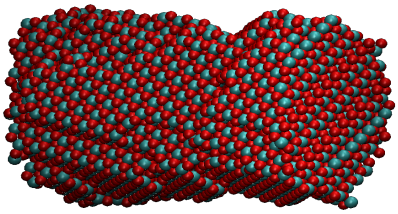

Figure 34: The atomistic model of the nanorod viewed in VMD comprising 15972 atoms with 5324 cerium atoms and 10648 oxygen atoms.

4.7.1 Equilibrate

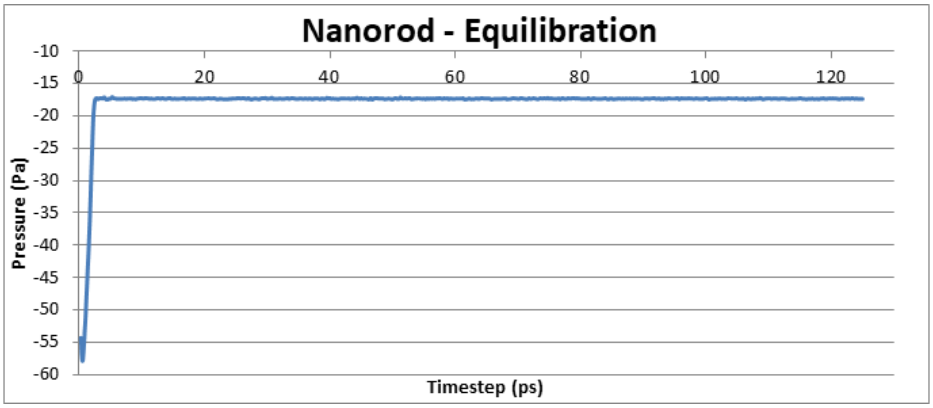

Figure 35: The time-pressure graph obtained for the equilibration of the nanorod.

In Figure 35, the graph shape is completely different to the nanoparticles. Instead of the harmonic style shapes the previous simulations gave, this graph initially starts with a

significantly low pressure at around - 57 Pa, and then a sudden rise to around -17 Pa, which then levels off. The axes scale, specifically the pressure axis, causes the pressure readings to seem as if there were no pressure fluctuations occurring. However, if the pressure axis was scaled to show only the readings between -15 Pa and -20 Pa, oscillations would show and the pressure fluctuations would be more visible. Nevertheless, it is clear that the equilibration for the nanorod is extremely different to the equilibration time-pressure graphs obtained for the polyhedrals and the nanocube.

4.7.2.0 200 Å/ps

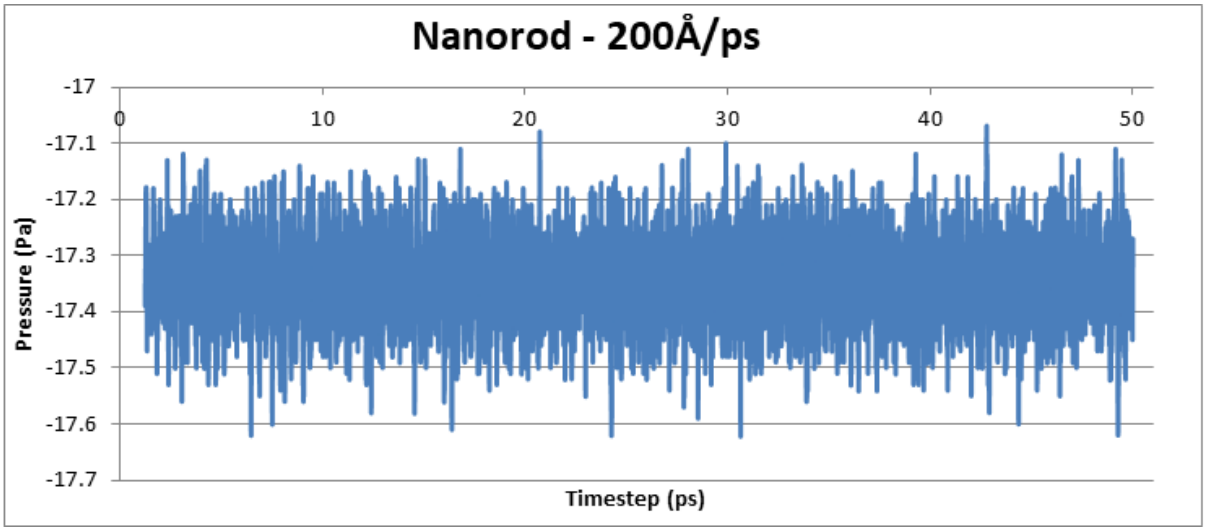

Figure 36: The time-pressure graph obtained for the breathing motion of the nanorod from a velocity of 200 Å/ps.

When the nanorod was viewed in the VMD visualiser, it seemed as if a breathing motion was successfully produced. Although the observation was different from the polyhedrals, where the polyhedrals experienced a spherical expansion and contraction in the radial direction, the entire structure moving as one unit. Contrastingly, the observation in VMD caused an assumption that the nanorod produced breathing motions simultaneously at various regions along the length of the rod. As shown in Figure 36, a frequency for the breathing motion could not be calculated due to the overlapping pressure fluctuations, which also supports the idea that multiple breathing motions were occurring at the same time.

A possible explanation for the overlapping may have been caused by the phonons reflecting off the dislocations, grain boundaries or point defects within the nanostructure, leading to the system recording more than simultaneous pressure fluctuations occurring at a single point. This is described in further detail in the 'Discussions' chapter.

4.7.2.1 500 Å/ps

A breathing motion was also attempted for the nanorod at 500 Å/ps as the simulation at 200 Å/ps produced a vibration, although a frequency could not be calculated. This was not successful and produced a similar graph to the one shown in Figure 36, in which there was severe overlapping of the pressure fluctuations. As the periodic boundary conditions were not compatible with the nanorod simulations, the time-pressure graphs produced had

severe overlapping of the pressure fluctuations and as a result, frequencies were not able to be calculated. For this reason, the nanorod structure was not investigated any further.

4.8 General Observations

The time-pressure graphs produced for the equilibration stages of each model were all smooth and showed no sharp edges. In contrast, the time-pressure graphs obtained from the vibrational data were a lot less smooth and the majority had a lot of abrupt edges. The most common observation from the breathing motion graphs showed that the pressure fluctuations were most active around the start of the simulation, caused by the initial shock of the velocity change. However, this was not the case for all of the nanostructures. The starting oscillations for the 4537 Ce and 6283 Ce models were not of an enhanced amplitude, unlike the smaller models.

The breathing frequencies vary with nanoparticle size but on a larger scale, the differences are not hugely significant.

Nanostructure	**Property Change**	**Frequency (THz)**	**Wavenumber (cm^{-1})**
Polyhedral, 336 Ce	100 Å/ps 200 Å/ps 100 Å/ps, 600K	2.225 ± 0.065 2.153 ± 0.014 2.180 ± 0.020	74.22 ± 2.17 71.82 ± 0.46 72.72 ± 0.67
Polyhedral, 1505 Ce	200 Å/ps 250 Å/ps 300 Å/ps 400 Å/ps 200 Å/ps, y coord 250 Å/ps, y coord	1.486 ± 0.035 1.360 ± 0.039 1.323 ± 0.013 1.303 ± 0.011 1.361 ± 0.014 1.344 ± 0.031	49.57 ± 1.17 45.36 ± 1.31 44.13 ± 0.43 43.46 ± 0.36 45.40 ± 0.48 44.83 ± 1.04
Polyhedral, 4537 Ce	100 Å/ps	1.097 ± 0.014	36.59 ± 0.47
Polyhedral, 6283 Ce	100 Å/ps	1.042 ± 0.035	34.76 ± 1.17
Nanocube	50 Å/ps	0.799 ± 0.014	26.65 ± 0.47

Table 3: A summary of the frequencies and corresponding wavenumbers calculated from the time-pressure graphs of the polyhedrals and the nanocube models, representing the breathing mode vibrations. The 'Property Change' column depicts the velocities used to produce the vibration, the temperature change applied when the default temperature of 300 K was not used, and the co-ordinate of where the velocity change was coded onto when the default x co-ordinate was not used. The models have been listed according to their atom count in ascending order, with the 336 Ce model having the lowest number of atoms and the nanocube having the largest number of atoms. Regarding the polyhedrals, as the diameter increases, the frequency of the breathing motion decreases. Similarly, when comparing the polyhedrals and nanocube together, the trend that a larger size produces a lower breathing mode frequency also applies.

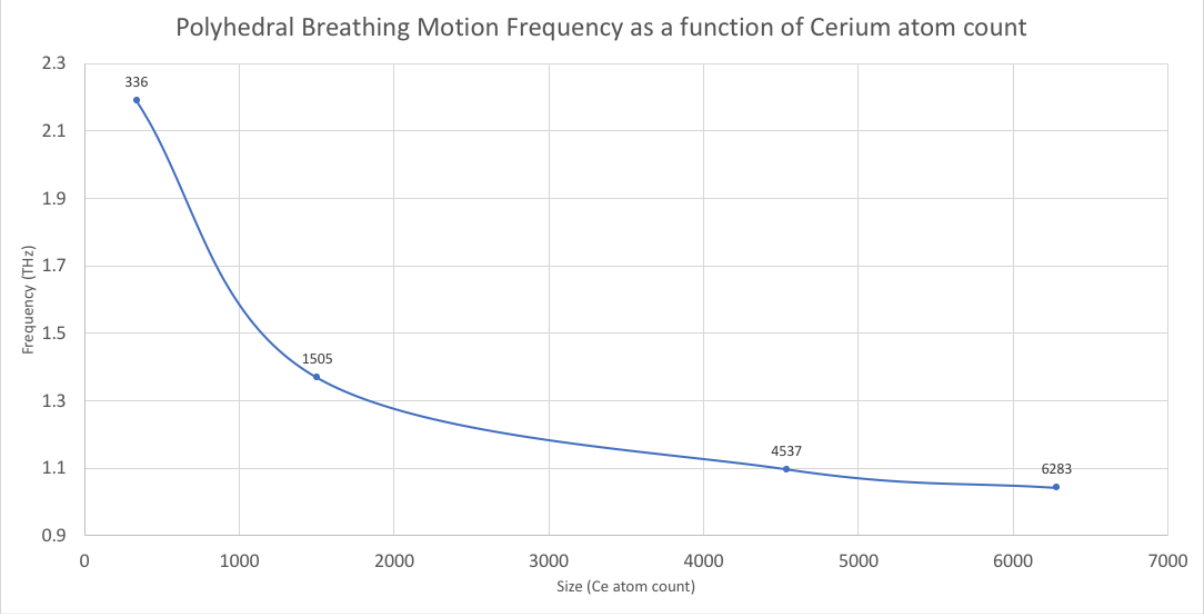

Figure 37: The average breathing mode frequencies given as a function of the cerium atom count of the polyhedrals. As labelled, the first, second, third and fourth points are the 336 Ce, 1505 Ce, 4537 Ce and 6283 Ce models respectively. For the average frequency of the 336 Ce breathing motion, the value obtained for the simulation at 600 K was not included. This gave the average frequency for 336 Ce to be 2.189 THz. For the average frequency of the 1505 Ce breathing motion, the vibrations with velocities coded onto the y co-ordinates were not included. This gave the 1505 Ce average breathing mode frequency to be 1.368 THz. The breathing motion frequencies of the 4537 Ce and 6283 Ce models were 1.097 THz and 1.042 THz respectively. Only one frequency was produced for the 4537 Ce and 6283 Ce models so there was no need to produce an average frequency.
The difference in frequency is larger for the smaller models compared to the frequencies for the larger models. For example, the decrease in frequency from the 336 Ce model to the 1505 Ce model is 0.821 THz but the decrease in frequency from the 4537 Ce model to the 6283 Ce model is 0.055 THz.

The frequencies found correspond with the IR region on the electromagnetic radiation spectrum, all the nanoparticles and the nanocube lying closer towards the far-IR region (low THz). More importantly, the data produced do not lie within the expected range of a breathing mode frequency and is a magnitude out, with the range compiled by Ghavanloo[4] which currently stands at 100-500 cm^{-1}. In particular, the ceria breathing mode frequency is given at 465 cm^{-1} as reported by McBride et al.[5] and 461 – 464 cm^{-1} as reported in multiple studies[6-8] for the bulk and nanoparticle respectively. Despite this, the data is closer to the lower end of the expected range, indicating that the values are not too far off and more robust results could perhaps be obtained at higher velocities (higher energy).
As all the frequencies obtained lie within the far IR region, it is assumed that if the ceria nanoparticle was to absorb a photon of frequency within the far IR region, then a breathing mode vibration would occur. For example, probing these breathing modes using lasers with wavelengths lying within the far IR region. The only issue is that these vibrational modes are a symmetric stretch type, which in the case of ceria, is IR inactive. This means that this particular mode will not absorb IR radiation for this mode to increase in energy level, and therefore, would not be observed in IR spectroscopy.
Breathing modes can be observed in Raman spectroscopy so this is one alternative. Another alternative would be the method produced by Wheaton et al.[9], where the authors used a combination of ultrafast optical Kerr spectroscopy and resonance Raman spectroscopy to resonantly excite the acoustic resonant vibrations of nanoparticles. This included the

induction of a breathing mode vibration. They used lasers to produce frequencies within the range of 10 GHz – 0.3 THz and when the laser frequency matched an acoustic resonant frequency of the nanoparticles, a vibration was induced. The laser range that Wheaton et al. used does not cover the breathing mode frequencies of the ceria models in this study, but the authors stated that the laser frequency range could be extended past 10 THz by using a laser with a "widely tuneable external cavity laser". This method could therefore be applied to the current study by using lasers of wavelengths perhaps within the range of mid GHz to mid THz, or any wavelength range that covers the frequencies obtained in this study.

An optical phonon can interact with electromagnetic radiation of frequency located within the far-IR region, which also means that they can occur at far-IR frequencies. Optical phonons have higher energy than acoustic phonons, and require a specific amount of energy for this mode to be excited. The frequencies obtained for the ceria nanoparticle models in this study are within the low THz range, which is included in the far-IR region. However, optical phonons occur when the atoms in the molecule move out of phase to each other during the vibration. This is not the case for a breathing mode, where the atoms are moving in phase to each other. The definition for an acoustic phonon involves the atoms moving in the same direction and in phase to each other, which would bring about the assumption that the breathing modes in this study are caused by acoustic phonons. Previous studies have also attributed nanoparticle breathing modes to acoustic phonons[9-11]. The breathing motion can therefore, be attributed to the longitudinal acoustic phonon branch.

4.9 References

(1) W. Humphrey, A. Dalke, K. Schulten, "VMD – Visual Molecular Dynamics", J. Molec. Graphics., 1996, vol 14, pp. 33 – 38

(2) E. Szilagyi, J. S. Wittenberg, T. A. Miller, K. Lutker, F. Quirin, H. Lemke, D. Zhu, M. Chollet, J. Robinson, H. Wen, K. Sokolowski-Tinten, A. M. Lindenberg, Nature Communications, 2015, 6:6577, DOI: 10.1038/ncomms7577

(3) Dassault Systèmes BIOVIA, Materials Studio Accelrys, Version 8.0, San Diego: Dassault Systèmes, 2017

(4) E. Ghavanloo, S. A. Fazelzadeh, H. Rafii-Tabar, International Materials Reviews, 2015, vol 60, pp. 312 – 329

(5) J. R. McBride, K. C. Hass, B. D. Poindexter, W. H. Weber, J. Appl. Phys., 1994, vol 76, pp. 2435

(6) M. L. Dos Santos, R. C. Lima, C. S. Riccardi, R. L. Tranquilin, P. R. Bueno, J. A. Varela, E. Longo, Materials Letters, 2008, vol 62, pp. 4509 – 4511

(7) E. K. Goharshadi, S. Samiee, P. Nancarrow, Journal of Colloid and Interface Science, 2011, vol 356, pp. 473 – 480

(8) B. Choudhury, A. Choudhury, Current Applied Physics, 2013, vol 13, pp. 217 – 223

(9) S. Wheaton, R. M. Gelfand, R. Gordon, Nature Photonics, 2014, vol 9, pp. 68 – 72

(10) J. H. Hodak, A. Henglein, G. V. Hartland, J. Chem. Phys., 1999, vol 111, pp. 8613 – 8621

(11) M. Ng, Y. Chang, J. Chem. Phys., 2011, vol 134, DOI: 10.1063/1.3563803

Chapter 5: Discussion

5.1 Comparison to Literature

For a series of ceria nanoparticle diameters of 2.7 - 7.6 nm, the values obtained in this report range from ~ 34.76 – 74.22 cm^{-1}. The nanocube produced a breathing frequency of 26.65 cm^{-1}.

McBride et al.[1] synthesised and analysed doped ceria compounds using Raman spectroscopy and X-ray diffraction. They stated that a metal dioxide with a cubic fluorite structure would produce a Raman active symmetric breathing mode, which they reported as 465 cm^{-1} for a bulk ceria. However, they also stated that this breathing mode is only caused by a ring of oxygen atoms surrounding the Ce^{4+} cation. The ceria compounds that McBride et al. probed are not of the nano scale but the more recent literature involving ceria nanoparticles have also mentioned to produce a breathing mode of a similar frequency but shifted a few wavenumbers[2-3]. The values obtained from the simulated ceria models are around an order of magnitude lower than the frequency observed by McBride et al.

Wheaton et al.[4] probed the acoustic vibrations of nanostructures using extraordinary acoustic Raman spectroscopy, which is a hybrid of ultra-fast spectroscopy and resonance Raman spectroscopy. The authors observed that polystyrene with a diameter of 20 nm produced acoustic vibrations at 1.47 cm^{-1} (44 GHz) and 2.28 cm^{-1} (68 GHz). The frequency to note is the peak that occurred at 2.28 cm^{-1} as this was stated to have been caused by a breathing mode. They also tested titanium dioxide, which had a diameter of 20.5 nm, and gave frequencies of 5.29 cm^{-1} (158.5 GHz) and 5.52 cm^{-1} (165.8 GHz). These values were obtained using a form of Raman spectroscopy, which is justified considering that the minimum frequency classed as IR radiation is around 300 GHz.

The near spherical, simulated models used in this current study gave frequencies within the low THz region (~ 1.042 – 2.225 THz) which lies within the far-IR region. The largest polyhedral model (6283 Ce) had a diameter of 7.6 nm, which gave a frequency of 34.76 cm^{-1} (~ 1.042 THz). This model is less than half the diameter of the polystyrene (20 nm) and gave a frequency of one order of magnitude larger than the breathing mode the authors obtained (2.28 cm^{-1}). This is a strong reflection of the inversely proportional relationship between particle size and frequency.

Despite having tested different nanoparticles, there lies a common finding between the results reported by Wheaton et al. and this present study, in which the frequencies decrease with increasing particle size. For example, the authors tested polystyrene with diameters of 20 nm, 30 nm and 40 nm which gave peak frequencies of 1.49 cm^{-1}, 1.08 cm^{-1} and 0.73 cm^{-1} respectively. This showed that the acoustic frequencies decreased as the diameter increased. However, it should be noted that these frequencies from polystyrene, aside from the peak given at 66 GHz, are not breathing modes and instead, are the "quadrupole accordion"[4] modes.

Dos Santos et al.[2] synthesised ceria powders which consisted of spherical nanoparticles with diameters of 4.8 – 10.4 nm. The nanoparticles produced a breathing mode detected by

Raman spectroscopy and gave a frequency of 464.5 cm^{-1}. Goharshadi et al.[3] also synthesised samples of powder ceria with the first, second, third and fourth samples consisting of average crystallite sizes 6.45 nm, 5.85 nm, 7.54 nm and 7.27 nm respectively. These samples produced breathing frequencies of 463 cm^{-1} for the first sample and 461 cm^{-1} for the second, third and fourth samples. If the second sample was disregarded, then it could be said that the larger sized particles gave a lower frequency. Both of these studies produced nanoparticles with diameters similar to the ceria models simulated in this current study, but gave breathing frequencies of around 461 – 464 cm^{-1}. This means that the breathing frequencies obtained for the ceria models are an order of magnitude out.

Choudhury et al.[5] observed the breathing modes of ceria nanoparticles, which had a crystallite diameter of 7.5 nm, giving frequencies at 462.15 cm^{-1}. They also observed the breathing modes of Nd doped ceria nanoparticles, which had crystallite diameters ranging from 4.0 – 6.4 nm, and gave frequencies around 455.73 cm^{-1}. The results show that the larger sized nanoparticles (7.5 nm) produced a higher breathing frequency than the smaller sized nanoparticles (4.0 – 6.4 nm), which is conflicting with the observations from Goharshadi et al. and Wheaton et al. This is a deviation from the standard view that a larger diameter causes a smaller frequency. However, Nd has a higher atomic mass than Ce, so doping ceria with Nd would give a compound of higher mass than pure ceria and as such, Nd would be the cause for this deviation. Doping has been previously observed to shift the breathing mode frequency of ceria nanoparticles[6].

Another study which produced similar results to Choudhury et al. is the one conducted by Babitha et al[7]. Babitha et al. synthesised four samples of powder ceria with the first, second, third and fourth samples consisting of particles with average diameters of 7.3 nm, 13.56 nm, 18.45 nm and 30.65 nm for the respectively, as well as calcinating at temperatures of 400 K, 550 K, 700 K and 850 K respectively. These samples gave breathing frequencies of 462.49 cm^{-1}, 464.81 cm^{-1}, 465.9 cm^{-1} and 465.98 cm^{-1} for the first, second, third and fourth sample respectively, using Raman spectroscopy. To summarise, the authors found that an increasing diameter produced a higher breathing mode frequency. This observation is a deviation from the trend that an increasing diameter causes a lower frequency, but the deviation is perhaps caused by the different calcination temperatures. The different calcination temperatures led to the formation of particles of varying diameters within each sample and as such, a differing size distribution for each sample. This would affect the breathing modes obtained because different particle sizes cause a shift in the frequency, even if it is only by a small amount. The authors have stated the samples to have average diameters, so as a result of the size distribution, the breathing modes obtained cannot be said to have been caused by a nanoparticle of one diameter, but caused by multiple nanoparticles of differing diameters.

Szilagyi et al.[8] probed the acoustic breathing modes from CdSe nanospheres of 3.4 nm and CdS nanorods of 4.5 nm x 18 nm by conducting X-ray scattering. They found that the nanospheres produced breathing modes, which occurred at amplitudes independent of the crystallographic direction. In short, the breathing mode responses were isotropic for spherical nanoparticles. They calculated the time taken for a breathing mode excitation to occur within the nanosphere to be given as ~ 1.1 ps. The nanorods produced anisotropic responses. Their study is evidence that a radial breathing mode can be produced at varying

levels of amplitude when different crystallographic directions are probed. For example, their results for the nanorod demonstrated that as the (100) and the (110) plane was perpendicular to the radial direction (direction in which a breathing mode occurs), the resulting breathing mode was experienced in full effect. Contrastingly, the (002) plane was positioned orthogonal to the long axis of the nanorod, therefore having no component in the radial direction. The (002) plane produced a breathing mode with the least effect.

The simulated nanorod in this current study produced overlapping pressure fluctuations of the system, from which a frequency was unable to be obtained from. Unfortunately, a comparison cannot be made with the findings obtained by Szilagyi et al., but their study sheds some light as to why the ceria nanorod produced overlapping fluctuations, as shown below in Figure 38.

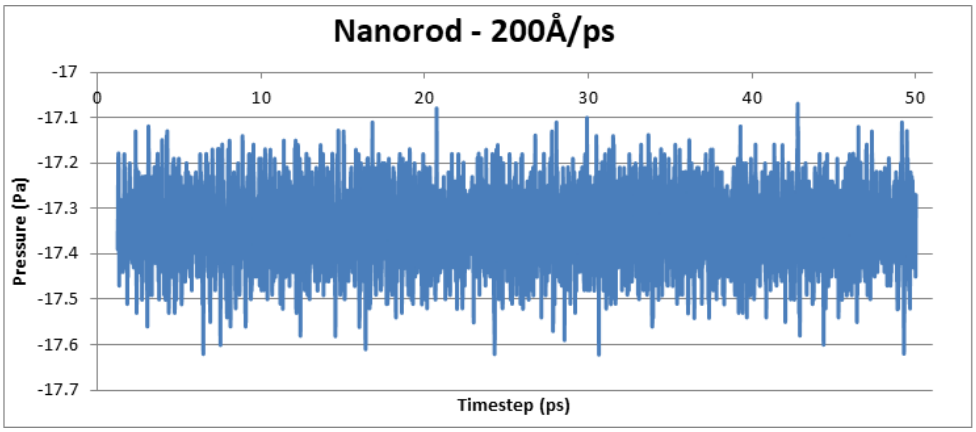

Figure 38: The time-pressure graph produced for the nanorod breathing motion.

In Figure 38, there is an overlap of the pressure measurements making it difficult for peaks to be counted and as such, a frequency could not be calculated. The overlapping pressure fluctuations is a result of the breathing modes occurring at different amplitudes for the different sets of planes. The affected planes were the {111} and the {100}, both of which are perpendicular to the radial direction, meaning that the breathing mode is experienced in full effect. There are multiple sets of these {111} and {100} planes so there are a lot of pressure fluctuation recordings, but as there are only two types of planes, there is not a heavy anisotropic response. If there were additional types of planes such as the {002} type, or other planes which are positioned orthogonal to the long axis, then there would be a greater overlap than the fluctuations produced in Figure 38.

The polyhedral ceria models in this current study are not completely spherical, but are somewhat similar to that morphology. A reminder that Szilagyi et al.[8] reported that spherical nanoparticles produce isotropic breathing modes, and if this can be applied to a polyhedral nanoparticle of near spherical morphology, then perhaps the same could be said for the polyhedral ceria models. To elaborate, the breathing modes were isotropic so regardless of what sets of planes had their pressure fluctuations recorded, the readings would still be of the same or similar amplitude. This meant that only one frequency reading would need to be obtained. In addition, multiple sets of planes on the polyhedral experienced the breathing vibration, meaning that there would be multiple recordings of the pressure fluctuations, but as they are isotropic, any overlap would not be as severe as observed for the nanorod.

Das et al.[9] simulated ceria models consisting of 24,696 atoms. Rewriting the atomic count of that model to make it easier to compare with the other models in this study, it could be termed as 8232 Ce (a third of the total number of atoms is the number of cerium atoms). The largest spherical nanoparticle used in this current study was 6283 Ce. Roughly speaking, there is a difference of about 2000 Ce atoms between the two models. The models in this study, 4537 Ce and 6283 Ce are also roughly around 2000 Ce atoms apart, and can be compared to reference the comparison between a 6283 Ce model and an 8232 Ce model. The frequency obtained for 4537 Ce (36.59 cm^{-1}) and the frequency obtained for 6283 Ce (34.76 cm^{-1}) showed a difference of ~ 2 cm^{-1}, which is not a large difference. It can therefore be assumed that perhaps the 8232 Ce model would also have a difference of ~ 2 cm^{-1} from the 6283 Ce model, giving an estimated frequency of 32.76 cm^{-1}.

The study conducted by Wheaton et al.[4] mentioned above has demonstrated that for a normal mode of vibration, an increase in the diameter causes a decrease in the frequency. However, the literature have shown that this does not apply for breathing modes when using Raman spectroscopy. To elaborate, the literature involves ceria nanoparticles of varying diameters, but the breathing frequencies are all within the range of 461 – 464 cm^{-1}. As the ceria breathing mode is caused by a ring of oxygen atoms surrounding the cerium cation[1], changing the cation size would not be expected to significantly affect the frequency. This is reflected from the literature as different sized ceria particles produced a breathing mode within the same frequency range. Despite this, the breathing frequencies obtained by Goharshadi et al. show some form of evidence that, although the shift is very small, a larger diameter produced a smaller frequency.

The overall difference is that the literature looking at ceria nanoparticle breathing modes are all obtained from ceria powders, consisting of various sized nanoparticles. The majority of the literature report the ceria nanoparticle diameter as an average, suggesting there is a size distribution to acknowledge. Contrastingly, the report by Wheaton et al. is an example of a study probing single, isolated nanoparticles. Although the authors' nanoparticles did not include ceria, breathing modes were still obtained which suggests that their method of probing single, isolated nanoparticles is more ideal for this current study than the other literature reported.

In general, the ceria models in this current study produced breathing frequencies an order of magnitude out. This may be due to the energy causing the vibration not being high enough, so perhaps the velocity was too low or perhaps the velocity increase needed to be coded onto multiple atoms to better emulate the applied energy. If the order of magnitude was accounted for, then the model with the breathing frequency closest to the literature is the 1505 Ce model, which produced a frequency of ~ 45.36 cm^{-1} for a velocity of 250 Å/ps. In other words, if the frequency was an order of magnitude higher, it would be ~ 450 cm^{-1} which, out of the simulated frequencies, is the closest to the experimental literature data.

The literature showed that using Raman spectroscopy to obtain the breathing frequencies would not produce significantly different results for nanoparticles of different diameters. In other words, different sized nanoparticles would produce near identical breathing frequencies. Using a different spectroscopic technique such as ultra-fast spectroscopy maybe able to produce a different result. The ultra-fast technique has been successfully

used to probe the breathing modes of nanoparticles such as gold, silver and platinum. Juve et al.[10] synthesised platinum nanoparticles of diameters from 1.3 – 3 nm, which produced breathing modes of 1.1 – 2.6 THz. Also, the study by Wheaton et al. mentioned above used a combination of a type of ultra-fast spectroscopy and resonance Raman spectroscopy, which was sensitive enough to probe and detect the acoustic vibrational response of single, isolated nanoparticles. Although the diameters of the nanoparticles from both of these studies are different from the ceria models, the authors from each study obtained breathing frequencies closer to the ceria models than the other literature that used Raman spectroscopy only. Using ultra-fast spectroscopy or the combination spectroscopy used by Wheaton et al. would perhaps be more sensitive to single ceria nanoparticles and the breathing frequencies produced could be more in agreement with the simulated data.

5.2 Why Breathing Modes?

5.2.1 Near-IR radiation and humans

Breathing modes occur at low frequencies so do not require high energy sources to be created. If a breathing mode can increase the reactivity of a specific surface plane on ceria nanoparticle, this would increase the catalytic effect of that plane and in turn, increase the effect of inducing angiogenesis. This would also mean that the ceria nanoparticle would have to be introduced into the human body to impose its 'healing' effect. The breathing modes, whilst in the human body, would therefore, have to be excited by a radiation source to occur. The breathing mode frequencies obtained from the ceria nanoparticle models in this study all lie within the far-IR region of the electromagnetic spectrum. This means that if the ceria nanoparticle was exposed to IR radiation of frequencies lying within the far-IR region, a breathing mode will occur. Within the entire IR spectrum, far-IR occurs at the lowest frequency, compared to near-IR as an example, which suggests that it would be the least damaging form of IR radiation for a human body to endure.

5.2.2 Identification and Detection of Ceria

Wheaton et al.[4] produced characteristic vibrational spectra of various proteins via acoustic Raman spectroscopy. This technique allowed for the identification of proteins and is beneficial in cases where the detection of proteins could help identify the presence of specific viruses or pathogens. The vibrations involved in his study were resonant vibrations, which are the type of vibrations that breathing modes are related to. The resonant vibration spectra obtained in his study could be used to detect proteins and therefore diagnose viruses, and it was assumed that perhaps the same could be said for resonant, breathing mode vibrations of ceria nanoparticles. Different vibrational modes are identified by their frequencies. Assuming that the breathing mode frequencies of ceria vary with differing sizes, this would allow for the detection of ceria but also be able to distinguish between particle size.

As observed by Goharshadi et al, a decrease in the particle diameter is correspondent to a lattice parameter increase. This observation was attributed to the increased formation of Ce^{3+} or oxygen vacancies. A breathing mode of a standard ceria nanoparticle, with no Ce^{3+} or oxygen vacancies, may produce a different frequency to one that does have Ce^{3+} and vacancies. This would assist with the identifying what type of ceria nanoparticle is present.

Also, Choudhury et al. observed the breathing modes of pure ceria nanoparticles and Nd doped ceria nanoparticles, obtaining frequencies of 462.15 cm^{-1} and 455.73 cm^{-1} respectively. A doped ceria nanoparticle will therefore, produce a breathing mode of differing frequency to pure ceria and these values would aid with distinguishing between the doped and non-doped. This would be useful for studies such as the one reported by Hijaz et al.[11] in which ceria was conjugated to folic acid in order to be taken up by folate receptors to induce cell death. Perhaps the authors would take a sample of the targeted cells and analyse the ceria content to investigate the concentration of ceria needed to induce cell death. The concentration of ceria cannot be determined by Raman spectroscopy or from the breathing modes. However, the identification of what ceria compound is present, via Raman spectroscopy probed breathing modes, could assist in the overall procedure in combination with a concentration determining analytical method such as UV-Vis spectroscopy. This is under the assumption that a folic acid conjugated ceria would produce a breathing frequency different to pure ceria.

5.2.3 Alternative and Increasing the Reactivity

Synthesising a shape different to the polyhedral ceria nanoparticle is one way to produce the more reactive planes, but an alternative option could perhaps involve increasing the reactivity of the {111} planes. The {100} plane is less energetically stable than the {111} type of plane, is more reactive and has a higher catalytic activity. This plane would therefore, act better as a catalyst than the {111} plane. However, the (111) plane is often naturally synthesised as it is thermodynamically more favourable.

Zhou et al.[12] synthesised ceria nanoparticles which produced the {111} plane as the dominantly exposed plane but also synthesised ceria nanorods which produced the more reactive {001} and {110} plane as the dominantly exposed plane. The nanocube is another shape which adopts the {100} plane as the majorly exposed plane[13]. However, synthesising a structure with the more reactive planes can be time consuming and difficult because it is producing the lesser thermodynamically stable planes.

Simulating the breathing mode in the region of a (111) plane would cause the vicinity to expand momentarily, displacing the atoms from their lattice positions and cause an increase in the surface energy. This would make the region more reactive, less stable than before and could turn it into a more catalytically active site. This effect would be observed for the entire structure as the breathing motion is not localised to one region, but to the whole structure. Perhaps the reactivities on the surface of ceria would increase.

Another observation worth noting from the study conducted by Zhou et al. was that they noticed the spherical nanoparticles experienced a loss in its redox ability after a cycle of reduction and oxidation. If a breathing mode vibration could increase the reactivity, then this could be a possible method to counter the loss of the redox ability.

However, there is an issue with this theory in which the vibration is only momentary and would mean that once the atoms return to their original lattice positions, the surface energy reduces back to its original level. Resultantly, the increase in reactivity would only occur for the duration of the oscillation where the structure is expanding. This is also reflected in the time-pressure graphs produced which showed that the initial oscillations (produced by the

breathing motion in the affected (111) region) lasted a few picoseconds, which suggests that the increase of reactivity for that vicinity would also only last for a few picoseconds.

By vibrating the nanoparticle, the lattice expands which would expose the surfaces further, making these surfaces less energetically favourable than they were when at rest. The natural assumption is that the grain in that particular area of impact would expand, but the grain boundary would also be affected. Grain boundaries are already a high energy component due to their structure being disordered, the surrounding normal crystal structure being disrupted, so by disrupting these junctions further, the energy would increase. In short, there would be a contribution in the increase of energy from both of the affected components, the grain and the grain boundary. Consequently, there may also be an increase in the reactivity of these specific surfaces as these components attempt to reduce the internal energy. In turn, this would increase the catalytic activity of the surface in that region.

5.3 Why Pressure and Frequency?

Pressure was selected as the property to be plotted against timestep to produce the frequency graphs. Pressure fluctuates with vibration, relative to the size of the system, and is expected to increase as the molecule withdraws and decrease when expanding. Therefore, observing the pressure movement as a function of time would be able to show when the lattice is expanding at its greatest effect, which would be when the pressure is at its lowest. This is in contrast to observing the vibration in terms of atomic displacement, a qualitative method, whereas observing the pressure fluctuations would describe the expansion and withdrawal motions quantitatively. Vibrational modes are identified by their frequency and so obtaining the breathing mode frequencies would allow for a quantitative comparison to literature data.

The first oscillation in the time-pressure graphs shown in the Results chapter is coming from the affected (111) surface plane. It represents that particular region expanding and gives somewhat of an indication of how much the reactivity may have increased by. To elaborate, the lattice expanding creates a momentary disruption between the intermolecular bonds within that region, in which the molecules are repelled from their original lattice positions. These movements would increase the surface energy and so the reactivity will have also increased. The graphs give an indication of the time frame of increased reactivity. When the affected region experiences the withdrawal part of the vibration, the molecules are returned to their original lattice positions, causing the surface energy to reduce back to its original level.

5.3.1 One Frequency, No Spectrum

There are many types of vibrational mode such as the symmetric and asymmetric stretch, the bending and wagging mode to name a few. These modes have variations in their movement and as a result, their characteristic frequencies all differ. In IR and Raman spectroscopy, this would mean that for a given compound, the absorption of radiation occurring at a specific frequency will excite a specific vibrational mode. A breathing mode is a symmetric stretch, for which there is only one variation this mode can move in, meaning that only one frequency will be obtained for this mode. In this study, only one frequency was extracted from each nanoparticle because only one vibrational mode was simulated,

the breathing mode. For an N number of atoms, a molecule will have (3N – 5) vibrational modes if it is linear. From these vibrational modes, (N – 1) will be the stretching modes which leaves ((3N – 5) – (N – 1)) as the number of bending modes. Ceria has 3 atoms, 3N, so it will have 4 vibrational modes, 2 of which are the stretch modes and 2 are the bending modes. The bending modes in ceria are degenerate so they produce the same frequency and resultantly, the same wavenumber. In IR spectroscopy, this would mean that only one absorption band would be shown for the bending modes, assuming a low resolution is used. The two stretching modes is the symmetric and the anti-symmetric stretch, of which the 'O = Ce = O' symmetric stretch is the breathing mode. Extracting the vibrations to produce an entire spectrum would mean that all of the vibrational modes of ceria would need to be simulated.

In addition, only one frequency was extracted because it is assumed that the breathing mode vibrations are being caused by phonons. Phonons are quantised vibrational energy, which means that they can only occur at discrete energy levels and as such, only specific values of energy and frequency are allowed. A crystal lattice vibration is caused by phonons, in which a collective of vibrational modes propagates through the lattice. These phonons supply each vibrational mode with quantised amounts of energy. The breathing mode is a longitudinal acoustic mode so only frequencies for this branch were obtained. Only one direction of wave propagation occurred and resultantly, only one wave vector was probed. On a graph of phonon frequency as a function of phonon wave vector, the breathing mode frequency of a single nanoparticle, where only one wave direction was probed (one wave vector), would account as one point on the graph. A spectrum would be obtained if other wave propagations were simulated, as this would mean that more wave vectors can be accounted for.

As mentioned in the comparison to literature sub section, a spherical nanoparticle produces isotropic breathing modes[8]. Applying this observation to polyhedral ceria of near spherical morphology would lead to the assumption that polyhedral ceria would therefore, also produce isotropic breathing modes. In other words, different crystallographic directions would experience the breathing mode at similar amplitudes. Only one frequency would need to be obtained for a breathing mode response representative of that particular polyhedral.

5.4 Calculating the Frequency

The method for calculating the frequency meant that it was easier to present the data in the standard form of frequency, Hz. These values were then converted to wavenumbers in an attempt to make the data easier to compare to literature.

The method for calculating the frequency was consistent but the selections of the data used in the calculations were not the same. To elaborate, some of the time-pressure graphs had their frequencies calculated from 0 – 50 ps because the first pressure fluctuations were recorded from 0 ps and the last pressure fluctuations at 50 ps. However, other graphs may have had their frequencies calculated from 2 – 50 ps as their pressure fluctuations were recorded from 2 ps. This was an attempt to acquire the most accurate representation of the breathing frequency. Uncertainties were included to account for the error obtained from human, manual counting.

5.4.1 Alternative: Velocity Autocorrelation Function Calculation

An alternative method for calculating the breathing mode vibrational frequency is by using the velocity autocorrelation function calculation[14]. This method is not complex and involves calculating an average of the velocities of the atoms per timestep, where velocity and its vector components are given by,

$$v_i = \Big(v_x(t_0), v_y(t_0), v_z(t_0)\Big)\, i \qquad (Equation\ 26)$$

where v_i is the velocity for each atom given as 'i', the velocity has components in in the x, y, z directions and t_0 is the timestep at zero, where t = 0. The first calculation in this method averages the velocities at t = 0 as a sum for all the 'i' atoms in the system,

$$C_v(t=0) = \frac{1}{N}\sum_{i=1}^{N}\big(v_i(t=t_0)\cdot v_i(t=0)\big) \qquad (Equation\ 26.1)$$

The next calculation would occur for the following timestep which can be generalised as,

$$t = t_0 + \Delta t \qquad (Equation\ 26.2)$$

This would change the velocity components for every atom 'i' to be given as,

$$v_i = \Big(v_x(t_0+\Delta t), v_y(t_0+\Delta t), v_z(t_0+\Delta t)\Big)\, i \qquad (Equation\ 26.3)$$

The averaging of the new velocities for this current timestep can then be calculated as,

$$C_v(t=\Delta t) = \frac{1}{N}\sum_{i=1}^{N}\big(v_i(t=t_0)\cdot v_i(t=t_0+\Delta t)\big) \qquad (Equation\ 26.4)$$

The general formula averaging the velocities and accounting for each timestep is given by,

$$C_v(t=n\Delta t) = \frac{1}{N}\sum_{i=1}^{N}\big(v_i(t=t_0)\cdot v_i(t=t_0+n\Delta t)\big) \qquad (Equation\ 26.5)$$

The average velocities are then plotted out against timestep and subjected to a Fourier space calculation to produce the vibration frequencies. The idea is that during a vibration, the atoms are moving in an oscillatory motion which entails velocity changes.

This calculation method is mainly used for fluids and liquids. The reason for selecting this method of calculation was based on the assumption that if ceria nanoparticles were to be introduced into the body for purposes such as inducing angiogenesis[9] or other biomedical applications, then it is possible that the particles would be in a solvent or immersed in a medium. Chakraborty et al.[15] reported that the acoustic vibrations of cylindrical nanostructures are dampened when immersed in fluids, with the vibrational energy dissipating into the medium. Also, Ruijgrok et al.[16] investigated the effect of damping on the

breathing modes of gold nanoparticles submerged in water, and found that the damping time and breathing frequencies for each nanoparticle was all within close proximity. This was in contrast to the breathing frequencies obtained for the gold nanoparticles in air, where there was a greater distribution in frequency and damping time. These two studies show that immersing nanoparticles in a solvent or liquid medium affects the resulting breathing mode frequency and if a breathing motion truly does increase the reactivity of the surface, then the damping could reduce this effect. If the breathing frequencies obtained in this current study were used to experimentally identify the size and shape of ceria nanoparticles, then there may not be a good agreement if the experimental ceria were submerged in solvents.

Although this calculation method is favoured for fluids and liquid systems, it has been previously used in a simulation study investigating the breathing modes of gold and silver nanoparticles[17]. However, this was beyond the scope of the project and the focus was kept on obtaining different frequencies for different sized ceria.

5.5 Ceria Models

The results have shown that the breathing mode vibrational frequencies produced differ with varying particle diameter. Ceria was the only compound tested but as the difference in frequencies was attributed to the particle size and the different surface planes, it can be assumed that a similar observation would be obtained for compounds with the same particle size and same surface planes.

5.5.1 Focus on Near Spherical Shape

Although three different types of nanoparticle shape were simulated in this study, most of the models were a near spherical, polyhedral shape. Sharp edged nanoparticles are not often used in nanomedicine due to their mechanical damaging effects on the body. Spherical nanoparticles are preferred and it would be counterproductive to simulate a whole collection of shapes that would lead to cellular damage. The spherical polyhedrals used in this study are not perfect spheres but out of all the available models, they are the closest to a standard spherical shape when compared to the nanocube and nanorod. As a result, more focus was given on investigating the spherical style polyhedrals as this type of nanoparticle was already used to induce angiogenesis[9], and therefore, would most likely be the shape implemented into medical use.

5.5.2 Ceria Size

The ability of ceria being able to modulate oxygen is a catalytic effect which means that this effect occurs on a catalytically active surface. It is well known throughout the nanotechnology community that the smaller nanoparticles have a higher catalytically active surface area compared to larger nanoparticles. Keeping in line with this statement, it made sense to simulate small nanoparticles and as a result, the models used in this study were all less than 10 nm in diameter. Also, the study by Das et al. observed that the ceria nanoparticles of a diameter larger than 15 nm did not induce angiogenesis. This is not to say that nanoparticles larger than 15 nm would not be useful in nanomedicine because there is a lot of research involving large nanoparticles implemented into medical treatment, but for

the purposes of this study and as the study by Das et al. was an inspiration for this project, the nanoparticle sizes were kept small.

Another point to note is that Deshpande et al.[18] reported that smaller ceria nanoparticles have a higher concentration of oxygen vacancies, vacancies which are only created when there is a presence of Ce^{3+}. A high Ce^{3+}/Ce^{4+} surface charge ratio is what drives the catalytic, anti-oxidant ability of ceria and so a smaller nanoparticle would be more ideal. Having said this, a simulation study would have had to have introduced the oxygen vacancies manually to the models, which can be time consuming and difficult to produce a model representative of an actual ceria nanoparticle with intrinsic oxygen defects. Therefore, models of ceria (Ce^{4+}) with no Ce^{3+} or oxygen vacancies were used, but was under the assumption that a smaller ceria model would produce somewhat similar results to a ceria nanoparticle of the same size but with oxygen defects.

Das et al. suggested the induction of oxygen modulation was due to the ratio of Ce^{3+}/Ce^{4+}. To assist this study, it may be worthwhile to investigate larger nanoparticles because a larger nanoparticle would provide a larger surface area for the Ce^{3+}/Ce^{4+} ratio to be adjusted. A smaller nanoparticle and a larger nanoparticle with differing amounts of Ce^{3+} and Ce^{4+} ions could have the same Ce^{3+}/Ce^{4+} surface area to volume ratio, but a larger nanoparticle would have more surface area and consequently, more cerium ions are able to be reduced, whereas a smaller nanoparticle would be limited in its choices of which ions can be reduced. Also, Zhou et al. reported that their nanorods performed better as a catalyst compared to the spherical nanoparticles, in which the nanorods were at least double the size in diameter. This shows that a smaller size may not be as effective when other factors such as the type of surface planes exposed, are taken into account.

As mentioned above, ceria nanoparticle has been successfully used to induce the process of angiogenesis. The authors[9] proposed that the reason causing the blood vessels to form was attributed to the different surface planes of the ceria nanoparticle having a different reactivity. In other words, they suggested that as the {100} planes on the surface were more reactive than the other surfaces {111}, they were more susceptible to anti-oxidant behaviour, preventing the ROS from causing any further oxidation.

A nanoparticle with a large diameter has a greater surface area to encompass more types of surface effects. The number of types of faces would still be the same, but the planes have a greater surface area to accommodate more oxygen vacancies. If the other factors affecting the reactivity were disregarded, then it could be said that the 6283 Ce model would be more reactive than the 336 Ce as the 6283 Ce model contains a larger surface area of each (100) plane for more oxygen vacancies to be implemented, and therefore, higher catalytic activity.

5.5.3 Why Nanorod?

A nanorod shape was tested because Zhou et al.[12] reported that their ceria nanorods demonstrated a higher catalytic activity when compared to the spherical nanoparticles. This study was conflicting with the standard view that a better catalyst usually consists of having a high surface area to volume ratio and more exposed faces, edges and corners (spherical nanoparticle), because the nanostructure with a low surface area and a large diameter

(nanorod) still showed higher catalytic activity. However, the nanorod had the more reactive planes as the dominantly exposed plane, and the spherical nanoparticles had the less reactive planes {111} as the dominantly exposed plane. If the nanorod was synthesised to have the less reactive planes {111} instead, then perhaps the spherical nanoparticle would have shown higher catalytic activity. This is evidence that the type of surface plane exposed seems to hold more influence in the catalytic ability of the nanostructure. Taking this into account, the nanorod was simulated to test whether the reactivity of specific surfaces could be increased by expanding the lattice in that region via vibration. This was the initial thought but after multiple unsuccessful attempts at simulating the nanorod vibration, it was decided that there would be no further investigation into the nanorod and the focus would continue with the spherical nanoparticles.

5.6 Nanorod Observations

5.6.1 Nanorod at 500 Å/ps, Grain Boundary Phonon Scattering

When the 336 Ce, 1505 Ce and the nanocube models were subjected to a velocity of 500 Å/ps, the simulations failed. Each model produced a “bursting” effect, possibly from the velocity being too high, suggesting that the energy applied was too great for the size of those systems (models). Contrastingly, the nanorod successfully vibrated which was confirmed visually in VMD.

A possible explanation for this could be due to the nanorod having a greater amount of atoms (15972), whereas 336 Ce and 1505 Ce had 1008 and 4515 atoms respectively. However, the nanocube had 20736 atoms, which is larger than the amount for the nanorod, but as mentioned above, the nanocube could not “endure” a velocity higher than 50 Å/ps. A definite conclusion cannot be made about this concept as the other polyhedrals, 4537 Ce and 6283 Ce, which both have large atom counts, could not be simulated at 500 Å/ps as the simulation duration was too computationally expensive.

Another possible explanation for the nanorod being able to “endure” a velocity of 500 Å/ps is perhaps due to the method of energy distribution. The nanorod distributes the applied energy (velocity induced breathing mode) in a seemingly different manner to the polyhedrals, in which the phonons are heavily reflected off the grain boundaries within the structure. This caused the pressure fluctuations to overlap, suggesting that a breathing motion was occurring in more than region of the nanorod, simultaneously. The phonons from these motions reflected off the variety of surfaces such as the grain boundaries and possible internal defects. This movement of being reflected back into the structure causes a “frustration” of somewhat amongst the particles due to the way the particles are positioned within the lattice. The phonon does not reflect back onto the original lattice point, but moves in a more random way and changes direction. The phonons overlapped, causing an overlap of the breathing motions, which was reflected in the time-pressure graphs as the pressure fluctuation recordings were overlapping, preventing a frequency from being able to be manually calculated.

Although a frequency could not be obtained for the breathing motion of a nanorod, the observations could be applied to thermoelectric research. The silicon nanowire and the ceria nanorod could be viewed as interchangeable in terms of shape, in which both are solid cylindrically shaped, the only difference being the aspect ratios. The observations from the

phonon movement in the ceria nanorod could perhaps assist in research involving the lowering of thermal conductivity in nanowires, which would increase the thermoelectric figure of merit, or in other words, the thermoelectric efficiency. Grain boundary scattering of phonons is one area of thermoelectric research looking at the origin of the mechanism and how it can be utilised to lower the thermal conductivity. The movement of the phonons causing these overlapping breathing motions in the ceria nanorod is caused by grain boundary phonon scattering. A deeper investigation of this could provide insight into the origins of the lowering of thermal conductivity in nanorods.

5.7 Abandoning the Nanocube and Nanorod

5.7.1 Nanocube

One nanocube was simulated in this study, other sized nanocubes were unavailable. This meant that a comparison between two or more nanocubes of different sizes was unable to be conducted because only one sized nanocube was tested. In other words, a definite conclusion cannot be made on whether the size of a nanocube can be determined from its breathing mode vibrational frequency. However, the frequency value obtained for the nanocube (28.35 cm^{-1}) is noticeably different from the range of values obtained for the polyhedrals (32.69 – 90.06 cm^{-1}). Without a second nanocube to compare to, it is difficult to conclude that this difference in frequency is caused by the shape of the nanoparticle. Another reason for the frequency difference between the nanocube and the polyhedrals may be caused by the size of the nanocube, and the number of atoms the model has. The near spherical polyhedral ceria nanoparticle is more used in application than the nanocube and resultantly, the nanocube was not investigated further.

5.7.2 Nanorod

When a nanorod vibrates, a wave like motion occurs in a similar manner to a regular nanoparticle vibration. Vibration within a nanoparticle from different planes and angles is outputted as an average, giving a graph with somewhat distinguishable peaks. This allows the frequency to be averaged in a relatively easy manner. In contrast, the vibrations in a nanorod give graphs which seem to look like they are from overlapping data measurements. Unlike a nanoparticle, where the vibration seems to flow as a continuous ripple through the structure, the nanorod vibrates in waves along the different planes, reflecting off other planes, causing these other planes to vibrate.

It is assumed that the breathing vibrations (pressure fluctuations) are being recorded simultaneously in an attempt to obtain an average, producing multiple layers of graphs with no clear peaks. Frequencies were attempted to be manually calculated from the time-pressure graphs but the values obtained were not following the general trend that was found for the other nanoparticles (frequency decreases with increasing nanoparticle size). For this reason, no further investigation into nanorods was conducted. A solution for this would be to create a much longer nanorod and change the periodic boundary conditions or adjust the cut-off value. However, as the nanorod would have boundary conditions different to the other nanoparticles, the results that would be produced may not be comparable to the other shapes.

5.8 Potentials and Parameters

One method of producing potentials is from assigning experimental values of the material properties, such as the lattice parameter, and as such, the potentials can have multiple parameters describing different properties of the material. Some properties can be described to a high degree of accuracy, but not all of the properties can be described so only the most important properties are assigned as a parameter[19]. Electronic-structure calculations are used to obtain property values for the parameters when experimental data is not available. The resulting potentials obtained as a result of these calculations have an error, as these values may be different to experimental data.

The potential parameters used in this study were sourced from Sayle et al.[20]. A study by Lewis and Catlow[21] adopted the method of empirical fitting, which included the assignment and correction of parameters to reach a medium between experimental and calculated values. They obtained potentials for a collection of ionic oxides, from which the oxygen-oxygen interaction was obtained by a study reported by Catlow[22]. The cerium-oxygen interaction values were obtained from T.X.T. Sayle[23].

Lewis and Catlow[21] obtained their potential values from two methods. One method involved an extrapolation process where they assigned the same hardness parameter to the cations which were similar, in terms of their charge and structure. The second method involved looking at the structural data of the oxides with a lower symmetry. The authors compared the cohesive energies of the calculated values against the experimental data and found a good agreement. Sayle et al.[20] noted that T.X.T. Sayle[23] deduced that the potentials obtained from these sources accurately represented the lattice parameters of ceria.

The precision of the pressure values generated could not be investigated. The potential parameters and the conditions employed are what contribute towards the accuracy of the calculations, but attempting for a higher precision would mean that repeat results would have to be obtained. This would involve repeating the entire simulation, but with the same potential parameters and conditions as the previous runs, which would generate the same results. Perhaps the precision could be investigated by reproducing the models from scratch and redoing the amorphisation and recrystallisation process. The precision was not investigated in this way because a good precision is not significant if the accuracy is poor. Despite this, the counting of the peaks to produce a value for the frequency was done manually (human error) so an uncertainty was given for each frequency. Although the precision could not be acknowledged in the generation of the simulation results, it could be accounted for from the counting of the peaks in pressure fluctuation.

5.8.1 Cut-Off, Ewald

A cut-off radius of 10 Å was implemented in all the simulations. Including a cut-off value prevents the calculation of the interaction energies of the entire, infinite, periodic system. This is advantageous with regards to computational time as it means that less unit cells are accounted for. The compromise is that the accuracy of the results is affected.

The Ewald convergence parameter greatly affects the accuracy of the calculation of the Coulombic interactions because its application is solely for the long range interaction. In general, the Ewald summation has a high accuracy and the speed is fast compared to when

the parameter is not applied. The precision value used was 10^{-6}. As with the potentials and the majority of the parameters used in this study, the cut-off and Ewald values were chosen as these had been successfully used in previous studies[9, 13] involving the ceria nanoparticle models used in this study.

5.8.2 Velocity Increase

The majority of the velocities used were two orders of magnitude higher than the velocities of the atoms at rest. The purpose of increasing the velocity was solely to produce a vibrational response from the nanostructure. Experimentally, perhaps the breathing motion could be produced by a radiation source with a wavelength within the far-IR region, as the frequencies obtained for the ceria nanoparticle models all lie within this frequency range. Raman spectroscopy could then be used to characterise these modes and as such, the velocity increase in this study was to imitate the effect of inducing a vibration from the radiation source in spectroscopic techniques. Ultra-fast, pump-probe spectroscopy has been widely used to observe breathing modes and could be another option.

The vibration in these simulations were initiated by velocity changes of the atoms within the structure to emulate a situation where a radiation source is directed onto the nanoparticle. In an attempt to produce reasonable, graphical results in the visualiser and the datasets, the velocities were changed to 2 orders of magnitude higher than the velocities of the other atoms. This value of increase was loosely based around the observation that nanoparticles have thermal conductivities around 2 orders of magnitude lower than bulk materials[24]. The justification for relating the velocity increase to thermal conductivity in this manner, is that increasing the particle velocity causes an increase in the thermal conductivity. Phonons are the dominant contributors to thermal conductivity in non-metals so increasing the velocity of a phonon would also cause an increase in the thermal conductivity. Phonons are quantised lattice vibrations and as such, it was assumed that a factor (velocity) affecting the thermal conductivity would also affect the resulting phonon (lattice vibration) that occurs.

The set of results obtained for 336 Ce and 1505 Ce showed that an increase in the velocity causes a decrease in the frequency, but also showed that the differing velocities did not produce any significant changes in the breathing mode frequency. This observation is not what was expected, as it was assumed that an increase in the velocity would represent an increase in the energy, and one would assume that a higher energy would either lead to a breathing mode of a greater amplitude or a higher frequency. The only data set that reflects one of these assumptions is the 1505 Ce breathing modes, in which the increase from 200 Å/ps to 300 Å/ps, or from 300 Å/ps to 400 Å/ps, showed a greater amplitude at the beginning of the oscillations in their respective time-pressure graphs when comparing one velocity to an increased velocity. To elaborate, the oscillations from 0 – 5 ps for the 1505 Ce – 200 Å/ps breathing mode had an average displacement of around $\pm$ 1.9 Pa, but the average displacement for the oscillations at 0 – 5 ps for 1505 Ce – 300 Å/ps was around $\pm$ 2.1 Pa.

Overall, the general observation from the 336 Ce and 1505 Ce breathing modes showed that a change in the velocity on the order of ~± 100 Å/ps did not change the frequency significantly. As a result, the changes in velocity for the further simulations were not

observed in detail, as reflected by the breathing modes of 4537 Ce and 6283 Ce being simulated for a velocity of 100 Å/ps only.

5.8.3 Temperature Change

An increase in temperature generally leads to an increase in kinetic energy, providing more energy to the vibrational modes so the amplitude would increase. The frequency therefore, would also be expected to increase. The frequency obtained for 336 Ce – 100 Å/ps, 600K did not reflect this expectation, and was lower than for the breathing motion at 100 Å/ps, 300 K. Based on this observation, an increase in the temperature would cause a decrease in the breathing motion. This result however, is not accurate as the equilibration for the model was conducted at a temperature of 300 K, so perhaps a re-equilibration at 600 K would produce a result more in line with what is expected of a vibration from a temperature increase. For this reason, a certain conclusion on the trend could not be made as only one simulation was conducted at a different temperature. The uncertainty of how great of an influence temperature has on nanoparticle vibration could be solved by simulating more nanoparticles at increasing temperatures.

A previous study has found that the nanoparticle size increases with calcination temperature[7], and another study found that heat influences the energy relaxation time[25]. It is clear that temperature has a more significant effect on the nanoparticle than observed in this study, it would be worth exploring further to pursue potential trends relating heat, nanoparticle size and frequency.

Another reason for not investigating the effect of increased temperature any further was due to a finding by Baudin et al[26]. Baudin et al. simulated the surface energies of ceria nanoparticle (111), (110) and (100) planes. The authors reported that the surface energy was higher for a more reactive plane. They also reported that as the temperature increased from 10 K to 300 K, the surface energy decreased, which they attributed to the kinetic energies attempting to bring the surface energy to a stable level. As the surface energy decreases with increasing temperature, the reactivity would also decrease. Based on this finding, it was assumed that increasing the temperature (higher than 300 K) in the vibration runs would also cause a decrease in the surface energy. This was reflected in the result for 336 Ce – 100 Å/ps where the first few oscillations had a displacement of 5 a.u but for 336 Ce – 100 Å/ps, 600 K, the first few oscillations had a displacement of 2.9 a.u. The vibration in that affected region was weaker than the same vibration at 300 K, suggesting that the surface energy at 600 K was lower.

5.8.4 Faster Timestep

It was suggested that changing the timestep from 0.00005 ps to 0.00001 ps would allow more data points to be recorded, which was predicted to produce a “smoother” graph. The ideal outcome would produce a graph similar to the equilibration graphs, in terms of having less abruptness to the shape.

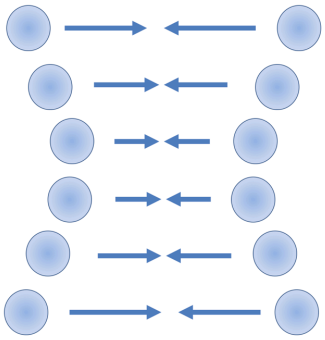

Figure 39: The movement of atoms during the vibration of a diatomic molecule, attraction and repulsion.

For a timestep of 0.00005 ps, perhaps every other movement would be recorded, missing out some data points. For a timestep of 0.00001 ps, this would have recorded every step shown. This explanation is relative to the diagram above (Figure 39) and it is this same concept that suggested a "smoother" looking graph would occur when setting a smaller timestep.

When the timestep change was implemented, the graph produced was not the expected outcome. Instead, more data than needed was calculated and recorded. Each part of the graph had a high density of data points and still gave a similar looking graph as before, sharp edges and abruptness. Resultantly, the decision to change the timestep to 0.00001 ps was not made.

5.8.4 Local environment

In this study, ceria nanoparticles were simulated with no significant regards to the neighbouring background. This is not the case in real terms, physical nanoparticles would most likely be surrounded by a medium or perhaps deposited on substrates.

Sound travels faster in water than in air but the energy needed to cause a vibration would be higher due to the density of water. This also applies to nanoparticles. The medium they are immersed in would strongly influence the velocity, consequently, also the vibrations that are able to be produced. The velocity of matter is greatly influenced by factors including drag and the Brownian motion. A possible factor, unrelated to velocity, to consider is whether having uniformly distributed nanoparticles in a colloid affect the vibrational frequency.

Also, as mentioned in the literature review, the ability of ceria to exhibit anti-oxidant and oxidant behaviour was due to the Ce^{3+}/Ce^{4+} ratio on the surfaces, but the pH of the surrounding environment also greatly affected this ability[27]. For example, ceria is known to be able to inhibit the production of an ROS, but an acidic condition reverses this ability and instead, the generation of an ROS is promoted. Generally, the production of an ROS is not a desired feature. As this project focused on the surfaces and exposing these surfaces further to promote reactivity, the environment was not considered. Observing the breathing modes of ceria nanoparticle in mammalian cells may provide differing results to the ones obtained in this study, due to the effect of pH on the modulation of oxidation state.

The local environment therefore, would affect the nanoparticle. As a result, the vibrations that would occur and the frequencies obtained experimentally may differ significantly. It is difficult to judge whether the comparisons are viable, the simulated results produced may not even come close to reaching agreement with an experimental realisation of this study.

5.9 References

1. J. R. McBride, K. C. Hass, B. D. Poindexter, W. H. Weber, J. Appl. Phys., 1994, vol 76, pp. 2435
2. M. L. Dos Santos, R. C. Lima, C. S. Riccardi, R. L. Tranquilin, P. R. Bueno, J. A. Varela, E. Longo, Materials Letters, 2008, vol 62, pp. 4509 – 4511
3. E. K. Goharshadi, S. Samiee, P. Nancarrow, Journal of Colloid and Interface Science, 2011, vol 356, pp. 473 – 480
4. S. Wheaton, R. M. Gelfand, R. Gordon, Nature Photonics, 2014, vol 9, pp. 68 – 72
5. B. Choudhury, A. Choudhury, Current Applied Physics, 2013, vol 13, pp. 217 – 223
6. I. Kosacki, V. Petrovsky, H. U. Anderson, P. Colomban, J. Am. Ceram. Soc., 2002, vol 85, pp. 2646 – 2650
7. K. K. Babitha, A. Sreedevi, K. P. Priyanka, B. Sabu, T. Varghese, Indian Journal of Pure and Applied Physics, 2015, vol 53, pp. 586 – 603
8. E. Szilagyi, J. S. Wittenberg, T. A. Miller, K. Lutker, F. Quirin, H. Lemke, D. Zhu, M. Chollet, J. Robinson, H. Wen, K. Sokolowski-Tinten, A. M. Lindenberg, Nature Communications, 2015, 6:6577, DOI: 10.1038/ncomms7577
9. S. Das, S. Singh, J. M. Dowding, S. Oommen, A. Kumar, T. X. T. Sayle, S. Saraf, C. R. Patra, N.E. Vlahakis, D. C. Sayle, W. T. Self, S. Seal, Biomaterials, 2012, vol 33, pp. 7746 – 7755
10. V. Juve, A. Crut, P. Maioli, M. Pellarin, M. Broyer, N. D. Fatti, F. Vallee, Nano. Lett., 2010, vol 10, pp. 1853 - 1858
11. M. Hijaz, S. Das, I. Mert, A. Gupta, Z. Al-Wahab, C. Tebbe, S. Dar, J. Chhina, S. Giri, A. Munkarah, S. Seal, R. Rattan, BMC Cancer, 2016, vol 220, pp. 220
12. K. Zhou, X. Wang, X. Sun, Q. Peng, Y. Li, Journal of Catalysis, 2005, vol 229, pp. 206 – 212
13. F. Caddeo, PhD thesis, University of Kent, 2016
14. Democritus: A Molecular Dynamics tutorial, ftp://ftp.dl.ac.uk/ccp5/DL_POLY/Democritus/Basic/Contents.html, (accessed January 2018)
15. D. Chakraborty, E. V. Leeuwen, M. Pelton, J. E. Sader, J. Phys. Chem. C., 2013, vol 117, pp. 8536 – 8544
16. P. V. Ruijgrok, P. Zijlstra, A. L. Tchebotareva, M. Orrit, Nano Letters, 2012, vol 12, pp. 1063 – 1069
17. M. Y. Ng, Y. C. Chang, J. Chem. Phys., 2011, vol 134, DOI: 10.1063/1.3563803
18. S. Deshpande, S. Patil, S. V. N. T. Kuchibhatla, S. Seal, Size dependency variation in lattice parameter and valency states in nanocrystalline cerium oxide, Appl. Phys. Lett., 2005, vol 87, pp. 133113
19. J. A. Martinez, D. E. Yilmaz, T. Liang, S. B. Sinnott, S. R. Phillpot, Current Opinion in Solid State and Materials Science, 2013, vol 17, pp. 263 – 270

20. T. X. T. Sayle, S. C. Parker, C. R. A. Catlow, 1994, Surface Science, 316(3), pp. 329 – 336
21. G. V. Lewis and C. R. A. Catlow, J. Phys. C: Solid State Phys., 1985, vol 18, pp. 1149 – 1161
22. C. R. A. Catlow, Proc. R. Soc. Lond. A., 1977, vol 353, pp. 533 - 561
23. T. X. T. Sayle, PhD Thesis, University of Bath, 1993
24. D. Li, Y. Wu, P. Kim, L. Shi, P. Yang, A. Majumdar, Appl. Phys. Lett., 2003, vol 83, pp. 2934 – 2936
25. S. H. Chung, A. Hoffman, S. D. Bader, C. Liu, B. Kay, L. Makowski, L. Chen, Appl. Phys. Letts., 2004, vol 85, pp. 2971 – 2973
26. M. Baudin, M. Wojcik, K. Hermansson, Surface Science, 2000, vol 468, pp 51 – 61
27. A. Wicki, D. Witzigmann, V. Balasubramanian, J. Huwyler, J. Control. Release., 2015, 200C, pp. 138 – 157

Chapter 6: Conclusion and Further Work

6.1 Conclusion

A variety of nanostructures were successfully vibrated using molecular dynamics. Frequencies were able to be calculated from the time-pressure graphs, the results showing differentiation between the sizes. In the case of the near spherical, polyhedral nanoparticles, the breathing mode frequency was found to decrease with increasing nanoparticle size. The calculated frequencies were amongst the very low THz values, suggesting that these breathing modes of ceria nanoparticles exist within the far-IR and Raman regions of the electromagnetic spectrum.

A frequency was also obtained for the nanocube but as there was only one model in the shape of a cube, differentiating between other nanocubes was not possible. Despite the lack of comparable data between different sized nanocubes, a value was successfully obtained which was noticeably different from the results obtained for the spherical nanoparticles. Whether this difference in value was due to the size is unfortunately beyond the scope of this project, but it is still some form of insight into how the breathing mode frequencies of ceria nanoparticles differ with the overall structure of the shape.

A similar case was observed with the nanorod in which only one model in this particular shape was available but also a further issue was the inability to calculate a frequency. Differing velocities were tested which resulted in frequencies of little variation. A higher temperature was also tested but the result obtained was not significantly different to prompt further testing. As shown in the literature review, previous studies have obtained radial breathing mode frequencies for carbon nanotubes, so it seems highly likely that a successful attempt at producing breathing mode vibrations for a ceria nanorod could be achieved if conditions were altered, the periodic boundary conditions as an example. Perhaps then, a more definitive conclusion could be drawn to state whether a ceria nanostructure can be identified as a nanorod shape solely from the breathing mode frequency. Time restraints prevented these alterations from being made but the view of distinguishing ceria nanoparticle shape by observing the breathing frequencies is still an optimistic one.

Despite not being able to conclude whether the breathing frequency can differentiate between a nanostructure (nanocube, nanorod), there were differences in the frequencies for the near spherical polyhedrals, with the oscillations at the beginning of the vibration being caused by the (111) plane in each respective model.

The literature has shown that when using Raman spectroscopy, the breathing mode of bulk and nanoparticle ceria is 465 cm^{-1} and 461 – 464 cm^{-1} respectively. As a result, the breathing mode frequencies obtained in this study are an order of magnitude out. However, as mentioned in the literature review and discussion sections, previous studies have used ultra-fast spectroscopy[1-2] to observe the breathing modes of metallic nanoparticles, giving frequencies closer to the simulated frequencies. Also, a study using a combination of ultra-fast spectroscopy and resonance Raman spectroscopy[3] has observed breathing modes within the low GHz region, which is interesting because these frequencies are outside of the

generally observed range of 100 – 500 cm^{-1} [4]. This suggests that using ultra-fast spectroscopy and resonance Raman spectroscopy, as opposed to using the standard method of observing breathing modes using Raman spectroscopy, would perhaps produce ceria nanoparticle breathing frequencies closer in range to the simulated frequencies.

The main aim of this work was to vibrate ceria nanoparticles to see whether the frequencies could distinguish between nanoparticle size. According to the simulated results, a larger diameter would cause a lower frequency, as expected, which is in agreement with some literature but not all.

6.2 Further Work

Conducting an experimental realisation of this simulation research would assist in validating the results of this study. This could be achieved by synthesising ceria nanoparticles of varying diameters to match the sizes seen in this study. The breathing modes of the single, isolated ceria nanoparticles can then be obtained using ultra-fast spectroscopy or a combination of ultra-fast and resonance Raman.

In this study, only one nanocube was able to be simulated and a breathing frequency for the nanorod was not able to be calculated. Further work could entail simulating the breathing modes of ceria nanocubes and nanorods of varying sizes. If a similar trend to the simulated polyhedrals is observed, in which the frequencies decreased with increasing diameter, then perhaps the breathing modes could also distinguish between different sized nanocubes and nanorods. This would also shed light on whether the breathing frequencies significantly differ for each nanostructure, which would assist in nanoparticle identification and detection.

For each nanoceria model simulated in this study, the single impact was directed at a region where a (111) plane existed. Simulating the models and targeting the impact at a (100) region would show whether the oscillations in the vibrations differ, and also whether the reactivity of this plane (already more energetically favourable than (111)) would increase.

In this study, all the models had Ce^{4+} but many ceria nanoparticles can also produce the Ce^{3+} cation on the surface, along with the production of an oxygen vacancy to maintain charge neutrality. This is the ability of ceria to exist as two oxidation states on its surface, which would mean multiple vacancies and possible defects are formed on the structure. As it is understood that the ceria breathing mode is caused by a ring of oxygen atoms surrounding the cation, oxygen vacancies would affect the frequency. An experimental realisation of these particles with oxygen vacancies could also contribute to ceria identification and detection, or identify whether the Ce^{3+} or Ce^{4+} is present. Perhaps then, it may be possible to apply this identification technique to particles used in nanomedicine.

6.3 References

1. 1. P. V. Ruijgrok, P. Zijlstra, A. L. Tchebotareva, M. Orrit, Nano Letters, 2012, vol 12, pp. 1063 – 1069
2. V. Juve, A. Crut, P. Maioli, M. Pellarin, M. Broyer, N. D. Fatti, F. Vallee, Nano. Lett., 2010, vol 10, pp. 1853 - 1858
3. S. Wheaton, R. M. Gelfand, R. Gordon, Nature Photonics, 2014, vol 9, pp. 68 – 72
4. E. Ghavanloo, S. A. Fazelzadeh, H. Rafii-Tabar, International Materials Reviews, 2015, vol 60, pp. 312 – 329